Mesoscale Variability in SUCCESS Data

Contract NAS5-97247

Annual Report

Oct 1, 1997 – Sep 30, 1998

Principal Investigator

Stephen D. Eckermann

CPI

Computational Physics, Inc.
Suite #600
2750 Prosperity Avenue
Fairfax, VA 22031
(703)204-1301; FAX (703)204-9121
http://www.cpi.com
eckerman@cpi.com

A three-year research project funded by:

Office of Aeronautics
National Aeronautics and Space Administration
Washington, DC 20546.

NRA-96-OA-01 (Area 3: SUCCESS Data Analysis)

Abstract

Analysis of meteorological, chemical and microphysical data from the airborne SUCCESS mission is reported. Careful analysis of the complex DC-8 flight pattern of May 2, 1996 reveals 19 linear or nearly linear flight segments within six main geographical areas, which we have analyzed. Significant mountain wave activity is revealed in the data from the MMS and MTP instruments on the DC-8, which resembles previous observations of mountain wave structures near Boulder, Colorado. Strong mountain-wave-induced upwelling downwind of the Rockies is noted. Turbulence is also noted in regions of the mountain wave consistent with overturning near the tropopause. Zonal winds recorded on the ER-2 are shown to be consistent with mountain wave breaking at or near critical levels in the stratosphere, consistent with the strong turbulence reported by the pilot during the ER-2 flight. These observations have been supported with spectral analyses and modeling studies. "Postcasts" of mountain wave activity on May 2, 1996 using the Naval Research Laboratory Mountain Wave Forecast Model (NRL/MWFM) predicts both strong mountain wave activity near the tropopause (as measured by the DC-8) and strong mountain-wave-induced turbulence in the stratosphere (as encountered by the ER-2). Two-dimensional simulations of fluid flow over topography reveal similar isentropic structures to observations.

Mountain wave-induced upwelling downstream of the Rockies generated wave clouds that were sampled during this flight. Analysis of *in situ* data from the DC-8 shows that the clouds were thin and formed by mountain wave-induced adiabatic cooling. A formal parcel advection methodology has been developed and applied to accurately model the production and distortion of vertically thin cloud and contrail layers by such gravity waves. The methodology has been used to extend the NRL/MWFM model to forecast mountain wave-induced cooling. The new model has been used to simulate stratospheric ice cloud formation by mountain waves on synoptic scales, as well as the effect of cooling by random spectra of gravity waves on equilibrium aerosol microphysics. The enhanced NRL/MWFM forecasts will play a major role in future NASA aircraft campaigns, such as the SAGE III Ozone Loss and Validation Experiment (SOLVE). The parcel-based theory has also resulted in unanticipated spin-off research, such as insights into the formation of gravity wave spectra in the atmosphere.

Table of Contents

1. Work and Results

1.1 Mountain Wave Encounter of May 2, 1996

1.1.1 Mountain Wave Structure from MMS and MTP Instruments on the DC-8

On May 2, 1996, the DC-8 flew a complex flight pattern aimed at sampling air within a mountain wave cloud over the Rocky Mountains near Boulder, Colorado. Strong velocity oscillations were recorded on the aircraft as it intercepted mountain waves. Plate 1[1] shows a three-dimensional perspective of the DC-8 flight path on this day (shown in red). Superimposed in white is the raw 1Hz vertical velocity activity measured by the new DC-8 Meteorological Measurement System (DC-8 MMS) [*Chan et al.*, 1998]. Ground-level color surface plots show topographic elevation. It is immediately evident that enhanced small-scale velocity activity was measured by the DC-8 MMS over the Rockies. It is also clear that the complex flight geometry of the DC-8 on this day complicates any analysis of the sampled wave activity (a full 3D animation of this plot is available on the web[2]).

To tackle this, a computer program was developed to read in arbitrary data from the instruments on the various aircraft platforms deployed during SUCCESS, and then interactively identify "regular" (i.e., nearly linear) flight segments that might be amenable to an analysis of wave properties. Results for the May 2 flight are shown in Figure 1. Black curves show (from top to bottom) time series of aircraft longitude, latitude, altitude and true air speed during the flight. Blue curves, labeled 1-19, show segments of the flight that were approximately linear in longitude, latitude and altitude. We chose not to include aircraft air speed in the classification since, as evident from the figure, it remains approximately constant once the DC-8 has reached cruise altitude. For test purposes, we also chose one flight segment (#6) with a small curved portion to its latitude-longitude trajectory, to assess the effect of curved airplane motion on derived parameters. This curve is marked in red in Figures 1 and 2.

Figure 2 shows three different planar sections of the three-dimensional flight geometry shown in Plate 1. Flight segments 1-19 from Figure 1 are superimposed on the latitude-longitude section (top plot) of Figure 2, along with colored shading depicting the underling topographic elevations. This grouping illustrates that flight segments 1-19 cluster within 6 main geographical "flight legs," labeled sequentially A-F and shown in orange in Figure 2. Details of these flight segments are given below in Table 1.

Flight Leg	Flight Segment #'s	Longitude-Latitude Transects	Cruise Altitude	Geographical Location	Direction (modulo 180)
A	1	40-41N, 100-105W	10.6 km	Kansas	NW,WNW
B	2,3	~41.5N, 106-108W	11.8 km	Southern Wyoming	WNW
C	4,5	40.2-41.5N, ~106W	11.8 km	Wyoming-Colorado	NNW
D	6	39.6-41.3N, ~105W	11.2 km	Wyoming-Colorado, slightly downwind (east) of Rockies	NNW
	7		10 km		
	8,11,12,16		11.8 km		
	15		12.4 km		
E	9,10	39.8N, 105-107.5W	11.8 km	Across Rockies, approximately west of Boulder, Colorado	WNW
	13,14		11.2 km		
F	17	39-40N, 98-104.5W	11.8 km	Colorado-Kansas	WNW
	18		11.2 km		
	19		7.3 km		

Table 1: Dominant flight legs (labeled A-F) during the DC-8 flight of May 2, 1996 (see Figures 1 and 2).

Legs A and F were essentially cruising patterns to/from the airfield from/to the Rocky Mountain region. Leg B was a sortie into Wyoming looking for wave clouds. Legs C and D were transects approximately parallel to the ridge axes of the dominant topography. Conversely, leg E was oriented roughly perpendicular to the dominant mountain ridge axis (see Plate 1 and/or Figure 2) which, based on standard mountain wave generation ideas [e.g., *Bacmeister et al.*, 1994; *Leutbecher and Volkert*, 1996], should efficiently profile any larger-scale mountain waves that were forced by flow over the larger-scale

[1] full page figures such as these are collated in Appendix D, to aid uninterrupted flow of the text.
[2] point your browser to the following URL: http://uap-www.nrl.navy.mil/dynamics/html/2may96.html

quasi-two-dimensional topography here. However, smaller-scale quasi-three-dimensional topographic features may force a spectrum of waves at various orientation angles, which would be profiled effectively during any of the flight legs B-E.

Figure 3 shows isentropes derived from Microwave Temperature Profiler (MTP) data during the four flight segments of flight leg E across the mountain ridge (shown in red). The cruise altitude of each flight segment is also shown with a colored curve on each plot. We note isentropic structure consistent with flow over this underlying topography, and subsequent penetration of forced mountain waves into the upper troposphere and stratosphere.

Figure 4 shows the three-component velocities, temperature and turbulent energy dissipation rates (TEDRs) measured *in situ* by the MMS during each of these flight legs (with 3 point smoothing applied). TEDR values were computed from the high frequency 1-5 Hz MMS data using the method described by *Chan et al.* [1998]. We note that the flight segment pairs at the same altitude (segments 9 and 10, segments 13 and 14) yielded very similar measurements, indicating a quasi-stationary mountain wave feature. We also note that the vertical velocity data (Figure 4c) are "noisier" and dominated by shorter scales than the horizontal velocity and temperature data (Figures 4a, 4b, and 4d, respectively). The TEDR data are noiser again, being dominated by highly intermittent short-scale turbulence events.

To study the large-scale mountain wave structures more effectively, these data were smoothed using a 65 point (~15 km) running average. These smoothed profiles are shown in Figure 5, which "cleans up" the vertical velocity and TEDR data in Figures 5c and 5e, respectively. In the zonal velocity and temperature traces (panels a and d, respectively), we see clear sinusoidal peaks and troughs with a horizontal wavelength ~0.5° (around 43 km), in reasonable agreement with earlier estimates [e.g., *Dean-Day et al*, 1998]. In the meridional winds (panel b) and temperatures (panel d), we also see evidence of a longer scale wave with a wavelength ~2° (~170 km). We also note order-of-magnitude increases in TEDRs at around 105.5°W, where large dips in the isentropes are observed in Figure 3. Similar enhancements in TEDRs are also seen at ~107°W.

1.1.2 Wave Cloud and Microphysics Observations from the DC-8 and ER-2

Wave clouds were also encountered on this flight, principally along flight leg D. Figure 6 shows total aerosol concentrations, volumes and surface areas measured by the MASP[3] instrument on this day [*Baumgardner and Gandrud*, 1998]. Figure 7 shows ice water content measured by the CVI[4] instrument (top panel) on the DC-8 [*Gerber et al.*, 1998]. These data reveal large aerosol volumes and water/ice occurrences on flight segments 8,11,12 and 16, which were all part of flight leg D (see Figure 1) and all occurred at a height of ~11.8 km (see Table 1). Note that during flight segments 6, 7 and 15, also part of flight leg D, these instruments did not record significant aerosol or water/ice content. The cruise altitudes of these latter flight segments were 10, 11.2 and 12.4 km, respectively (see Table 1). This indicates a thin vertical cloud layer located at ~11.8 km, inferences supported by the cloud lidar returns taken from the ER-2 during May 2, 1996 (see Figure 8 opposite). From Figure 3, this cloud altitude of ~11.8 km lies just a few hundred meters below the tropopause.

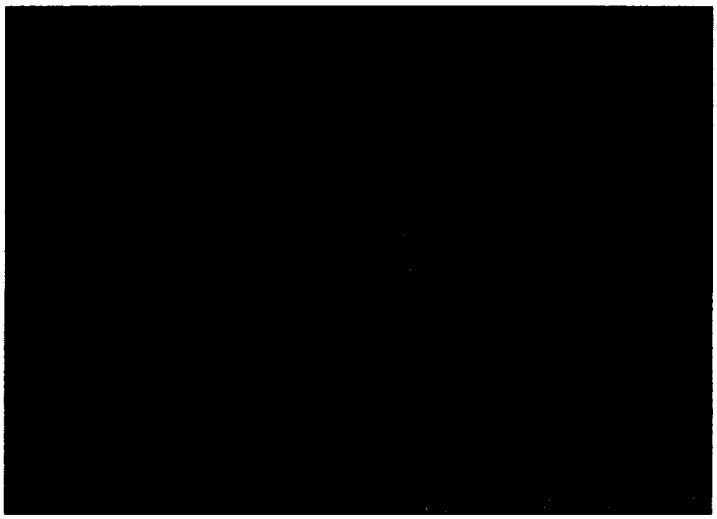

Figure 8: Backscattered power from the downward-scanning CLS (cloud lidar system) on the ER-2, May 2, 1996.

Flight leg D lies approximately north-south at 105°W, somewhat downstream (eastward) of the dominant topography (see Figure 2). From Figure 3, this region is seen to be at the isentropic ascent phase of the mountain wave near the tropopause, yielding adiabatic cooling and thus increased likelihood of cloud particle condensation at ~11.8 km. Similar processes have been simulated using NRL/MWFM simulations of mountain waves in the Arctic stratosphere [*Carslaw et al.*, 1998a, 1998b, 1999], where parcel theory is used to predict mesoscale cooling due to wave-induced upwelling [*Eckermann and Bacmeister*, 1998; see also section 1.4]. Microphysical simulations of the wave clouds measured here support the notion that wave-induced upwelling and adiabatic cooling triggered ice cloud formation *via* heterogeneous freezing along flight leg D [e.g., *Jensen et al.*, 1998; *Weinheimer et al.*, 1998] (see also section 1.4).

[3] multiangle aerosol spectrometer probe
[4] counterflow virtual impactor

1.2 NRL/MWFM "Postcasts" for SUCCESS Mission Days

Figure 9 plots maps of "postcast" mountain wave activity for the Boulder region on May 2, 1996. These maps were generated using the Naval Research Laboratory's Mountain Wave Forecast Model (NRL/MWFM[5]) interfaced to National Center for Environmental Prediction (NCEP) assimilated winds and temperatures for the day (daily global NCEP data on a 5°x2° grid).

Figure 9c shows postcast peak mountain wave displacements at 200mb, which is within the DC-8 cruise altitude range of ~11-12 km. The DC-8 flight track on May 2, 1996 is also shown. We see that NRL/MWFM predicts large mountain wave displacement amplitudes near the eastward end of flight leg E, as observed in Figures 3 and 4. Figure 9d shows postcast normalized momentum flux divergence between levels, a measure of wave dissipation and local turbulence production (0 = no dissipation, 1=maximum wave dissipation). We see that NRL/MWFM predicts some turbulence on the westward end of flight leg E. Some evidence of such turbulence exists in TEDRs inferred from the MMS in Figure 5e.

Recent extensions of the NRL/MWFM model have been made so that mountain-wave-induced mesoscale cooling can be forecast by the model [see *Eckermann and Bacmeister*, 1998; see section 1.4], since it is this wave-induced effect that is of most relevance to microphysical model predictions. The peak vertical displacement amplitudes of ~1-2 km in Figure 9c translate into peak mesoscale coolings of ~10 K in mountain-wave updrafts near the tropopause, which are sufficient to drop air below the frost point and trigger the ice clouds observed on flight leg D [*Jensen et al.*, 1998].

The ER-2 flew a similar flight pattern through the stratosphere on this day, occasionally overflying the DC-8 in efforts to observe from above any subsequent contrailing from the aircraft or effects of aircraft exhaust on the mountain wave cloud (the ER-2 flight track is plotted in Figures 9a and 9b). This ER-2 flight was "highly turbulent" according to pilot notes[6]. Figure 9b shows normalized momentum flux divergence at 100mb (~16 km) simulated by NRL/MWFM. We note large predicted mountain-wave-induced turbulence production at this level that frequently intercepts the ER-2 flight path, consistent with the turbulence reported by the pilot during this flight. The reasons for this intense turbulence production can be noted from the navigational zonal winds recorded on the ER-2 during this flight, shown in the top panel of Figure 10. We note zonal wind values near zero and even some westward values, as opposed to the strong eastward winds in the troposphere. Such vanishing or reversing zonal winds in the presence of zonally-aligned mountain waves are characteristic signatures of the wave overturning at or near a critical level, and are points where strong turbulence is to be expected, as discussed by *Ralph et al.* [1997a]. Thus, both *in situ* data and modeling results support the notion that this highly turbulent ER-2 flight was due to strong breaking of mountain waves at or near critical levels in the stratosphere.

1.3 Fourier and Wavelet Spectra of DC-8 MMS Fluctuations

Bacmeister et al. [1996, 1997] demonstrated that wavelet-based analysis of MMS data from accumulated ER-2 flights was a useful and illuminating way of spectrally analyzing these data. Initial Fourier-based power spectral analysis of MMS data from SUCCESS was provided by *Chan et al.* [1998], and some preliminary wavelet-based spectral analysis was provided by *Demoz et al.* [1998]. Both studies reported spectral shapes at small spatial scales ~k^{-3}, where k is horizontal wavenumber, consistent with earlier stratospheric findings [*Bacmeister et al.*, 1996]. Evidence of a $k^{-5/3}$ turbulent regime was also noted at very short scales in some of the observations [e.g., *Chan et al.*, 1998]. Detailed wavelet and Fourier spectral analyses of data from all the flight segments have been undertaken. Results for one particular flight segment (segment 14) will be shown here, to give a feel for the sort of results such analysis has yielded.

Figure 11 shows continuous wavelet spectra (right column) of unsmoothed (1Hz) zonal, meridional and vertical velocity fluctuations measured by MMS along flight segment 14 (see Figure 4), using the algorithm of *Torrance and Campo* [1998] with a Morlet wavelet basis (Gaussian-modulated sinusoids) and spectral oversampling. For zonal winds, we note that the wavelet spectrum identifies the 43 km mountain wave, but that it peaks most strongly in the eastward portion of the flight rather than in the westward part. This is consistent with the stronger isentropic oscillations and larger orographic falloffs in this region noted in Figure 3. Similar features are evident in the meridional velocity spectrum. Furthermore, the longer scale wave of wavelength ~170 km also appears strongly in the wavelet spectra. Peaks are also evident at an intermediate scale ~90 km, which may be due to spectral leakage caused by a non-optimal choice of wavelet basis functions.

Wavelet spectra of vertical velocities (bottom right panel of Figure 11) show evidence of these wavelengths. However, they also show evidence of intense short-scale perturbations. Indeed, we see clear evidence of strong oscillations of ~15 km wavelength at the westward and eastward extremities of the flight segment that show out clearly in the wavelet spectrum. Closer inspection of the wavelet spectrum also reveals significant subsidiary peaks at wavelengths ~1.5 km (isolated blue peaks in the spectrum at flight distances 3910km, 3990 km, etc.), which are not obvious from direct inspection of the time series. These features appear to be correlated to phases of the 15 km vertical velocity wave, and so could be coherent turbulent and/or nonlinear wavelike structures associated with instability/overturning of the primary wave [e.g., *Fritts et al.*, 1997]. Another possibility is that the DC-8 may be sampling the wake vortex that it created earlier during the outbound flight segment #13 (an encounter with wake vortices on May 4, 1996 was reported by *Chan et al.* [1998]). Note that

[5] see the NRL/MWFM web site at http://uap-www.nrl.navy.mil/dynamics/html/mwforc.html
[6] see http://cloud1.arc.nasa.gov/success/daily_summary/Flight_reports/960502.er2.html

the locations of these peaks correlate well with peaks in TEDRs for flight segment 14 shown in Figures 4e and 5e. Wavelet analysis is ideal here, has it captures all of these strong nonstationary oscillations in various part of these time series.

It is interesting to compare these results with the findings of conventional Fourier autospectra, shown in Figure 12. Note that the autospectrum of vertical velocity oscillations reveals peaks ~15 km and ~1.5 km, as in the wavelet spectrum, although the autospectrum goes not give the locations of this variability in the time series. The nonstationarity of the oscillations at these scales leads to noticeable spreading of the power spectral peaks in Figure 12. Light curves on the velocity autospectra in Figure 12 show k^{-3} (solid curve) and $k^{-5/3}$ shapes. We note for all spectra a noticeable transition, from k^{-3} shapes at larger scales, consistent with gravity waves [*Bacmeister et al.*, 1996], to $k^{-5/3}$ spectral shapes at short scales, consistent with inertial-range three-dimensional Kolmogorov turbulence [e.g., *Chan et al.*, 1998]. Note in particular that the vertical velocity peak at ~1.5 km wavelength occurs within this $k^{-5/3}$ spectral regime, suggesting that these structures may be coherent turbulent structures of some kind generated by mountain wave dissipation (e.g., vortex rolls, Kelvin-Helmholtz instabilities, etc.).

1.4 Generalized Parcel Advection Methodology for Modeling Gravity Wave Influences on Minor Constituents

It is well known that gravity waves (including mountain waves) significantly influence cloud formation [e.g., *Banta*, 1990] as well as contrail evolution and dispersion [e.g., *Schumann et al.*, 1995; see also section 1.1.2]. Yet the way in which gravity-wave dynamics interact with chemistry, microphysics, diffusion and larger-scale advection remains poorly understood at present [*Schumann et al.*, 1995].

As a formal approach to these issues, we have developed a parcel-based approach to the problem, based on the concept of quasi-adiabatic advection of air under the influence of gravity waves. Such an approach is often assumed to be valid for gravity waves, but has never been formally justified. Indeed, the approach differs significantly from traditional analyses of this problem for gravity waves, which involve linearized perturbation expansions of rate equations governing the chemical evolution of the relevant minor constituent. Such approaches require a background constituent profile that varies only gradually with height and horizontal distance, which is rarely the case for minor chemical species and aerosols in the upper troposphere [e.g., *Newell et al.*, 1996]. Indeed, very thin aerosol and water/ice layers were also observed here [section 1.1.2, Figures 6-8]. The formal parcel-based analysis method we developed avoids such a restriction. Furthermore, the approach gels naturally with conventional parcel advection models of the larger-scale mean transport and quasi-horizontal diffusion of air by synoptic-scale motions [e.g., *Brasseur et al.*, 1996], allowing interactions among these dynamics to be gauged more easily using gravity-wave-based additions to an existing modeling framework.

Our method is based on first-principles theory of dry parcel advection. We derive results for a hierarchy of simplified

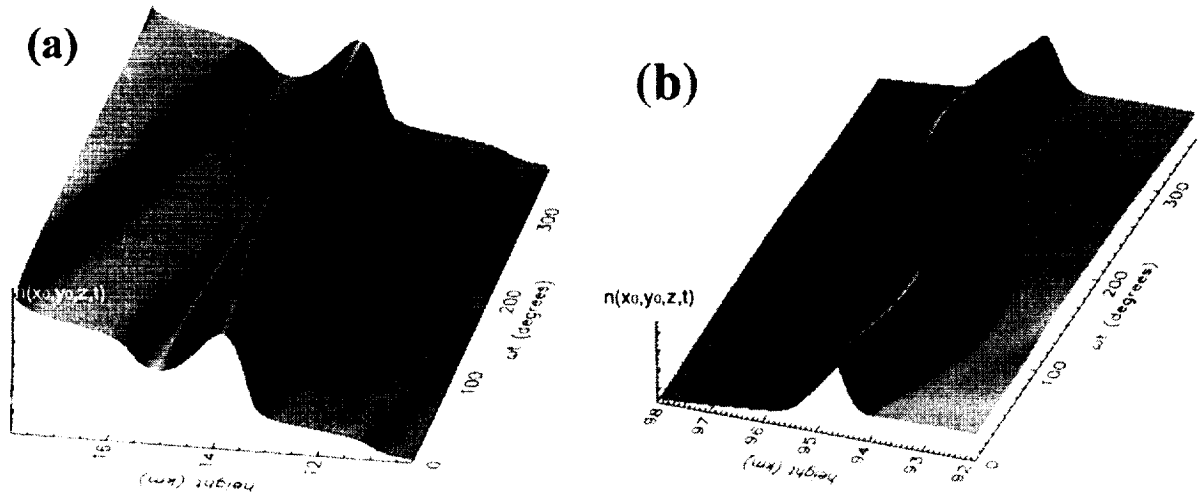

Figure 13: Height-time surface renderings of vertical profiles of minor constituent number densities as a gravity wave passes through the layer, as simulated using the parcel advection methodology of *Eckermann et al.* [1998]. Plots show gravity wave interactions with: (a) a laminated ozone profile in the lower stratosphere; (b) a large narrow enhancement in mesospheric sodium densities. See *Eckermann et al.* [1998] in Appendix A for more details.

problems which have been solved previously using conventional linearized perturbation expansions. The two methods give identical results. However, in environments where the minor constituent exhibits large spatial inhomogeneities (e.g., cloud and contrail distributions, tropospheric ozone etc.), the parcel method gives far superior results. This work was written up and accepted for publication in *The Journal of the Atmospheric Sciences* [*Eckermann et al.*, 1998]. A reprint of the published article is provided in Appendix A.

Sample results are shown in Figure 13. Panel a shows a gravity wave of vertical wavelength 2.3 km interacting with a laminated ozone profile in the lower stratosphere, which models the lidar observations of *Gibson-Wilde et al.* [1997]. Similar

inhomogeneities (e.g., cloud and contrail distributions, tropospheric ozone etc.), the parcel method gives far superior results. This work was written up and accepted for publication in *The Journal of the Atmospheric Sciences* [*Eckermann et al.*, 1998]. A reprint of the published article is provided in Appendix A.

Sample results are shown in Figure 13. Panel a shows a gravity wave of vertical wavelength 2.3 km interacting with a laminated ozone profile in the lower stratosphere, which models the lidar observations of *Gibson-Wilde et al.* [1997]. Similar laminated ozone profiles occur in the troposphere [e.g., *Newell et al.*, 1996; *Langford et al.*, 1997]. We see in Figure 13*a* a periodic expansion and contraction of the width of the ozone lamina. Furthermore, Figure 13*b* shows that for narrower layers again, there is also significant vertical advection of the layer as well as contraction and dilation of its width. Standard linearized perturbation analyses cannot capture this behavior [*Eckermann et al.*, 1998]. While the simulations in Figure 13 are nominally stratospheric and mesospheric, they assume tracer-like behavior (i.e. no radiation or chemistry) and so are directly applicable to the distortion and advection of analogous tropospheric layers, such as the narrow cloud and jet contrail layers sampled during SUCCESS.

We have tested the method further in microphysical simulations of wave-induced effects on polar stratospheric clouds (PSCs). This is a sensible first extension of the method to non-tracers, since the chemistry and microphysics required to simulate PSCs is usually significantly simpler than for tropospheric clouds, thereby allowing more straightforward initial tests using the new modeling methodology. This was achieved by using the method to quantify wave-induced adiabatic cooling of air parcels by mountain wave upwelling, which was then used to extend NRL/MWFM to generate global maps of postcast mountain-wave-induced temperature perturbations [*Eckermann and Bacmeister*, 1998]. The work has led to significant published work on PSC formation by stratospheric mountain waves in the Arctic and its possible influence on the ozone budget [*Carslaw et al.*, 1998a, 1998b, 1999]. We also used the parcel method in a more theoretical assessment of how typical random spectra of gravity waves might influence ambient distributions of aerosol particles [*Bacmeister et al.*, 1998]. All four papers have appeared in press or have been accepted for publication, but only the latter paper is included in Appendix B (to save space). These published works have come as spinoffs of the theoretical work initiated here as part of the current research project. Applications of the insights gained in these stratospheric simulations will be used to study the SUCCESS wave cloud and contrail data. Indeed, the findings in these stratospheric simulations may have quite direct relevance to upper tropospheric ice clouds and subvisible cirrus, since their microphysics and chemistry have many similarities to PSCs [e.g., *Jensen and Toon*, 1994; *Borrmann et al.*, 1996; *Jensen et al.*, 1998]. The enhanced NRL/MWFM model will also play an important forecasting role in flight planning for future NASA aircraft campaigns, such as the SAGE III Ozone Loss and Validation Experiment (SOLVE), planned for the Arctic in the winter of 1999-2000.

There was another unanticipated theoretical spinoff from this parcel-based work. In developing the parcel advection code, it became clear that superposing gravity waves would, in essence, "advect" parcels of constant potential temperature across other waves' phase fronts. In other words, gravity waves should advect not only minor constituents, but the phase structures of other waves! Such a process (if valid) could lead to waveform distortions, which in turn should be relevant to measured profiles of wave-induced fluctuations and their spectra (e.g., section 1.3). Thus, a simple parcel-based advection model of superposing gravity waves was developed to assess these ideas. Waveform distortions did indeed arise. Furthermore, the spectra of the vertical profiles yielded regular quasi-universal M^{-3} autospectra, where M is vertical wavenumber. Spectra such as these are routinely measured in the atmosphere and have been the subject of intense theoretical debate for more than a decade [e.g., *Smith et al.*, 1987; *Hines*, 1991]. These findings were written up, and the paper has been accepted for publication in *Geophysical Research Letters* [*Eckermann*, 1998]. A reprint of the published article is provided in Appendix C. These results provide new insights into mesoscale dynamical interactions and spectral formation.

1.5 Numerical Model Simulations of the Mountain Wave

In addition to NRL/MWFM simulations of mountain waves, we aim to simulate the waves directly using nonlinear numerical fluid dynamical models of flow over orography. The original goal was to work with Dr. J. T. Bacmeister and Dr. J. Rottman in using the MM5 model for this purpose. However, during this period both individuals have taken new jobs in other fields and are no longer be involved in the project. Presently, we are working with Dr. Andreas Dörnbrack in Germany on this problem, who uses the MM5 model to simulate mountain waves in the Arctic. This has proven useful, since Dr. Dörnbrack uses a modified version of MM5 that has been extended well into the stratosphere (lid at ~27 km). This affords the potential to study not only the mountain wave activity intercepted by the DC-8 near the tropopause, but also mountain wave-induced turbulence intercepted by the ER-2 in the stratosphere.

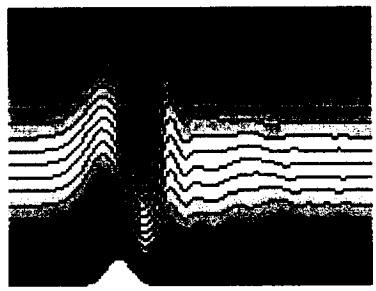

Figure 14: Isentropes generated by eastward flow over Gaussian hill using the UNSW/NRL mountain wave model.

To date, we have conducted some simplified studies using a two-dimensional nonhydrostatic numerical model of flow over orography (the

2. Analysis

2.1 Interpretation of Results Obtained to Date

Dean-Day et al. [1998] presented an initial analysis of mountain wave activity inferred from the DC-8 MMS and MTP during this May 2 SUCCESS flight. We have expanded upon their preliminary analysis of these data. Combining the many types of data acquired aboard the DC-8 yields a great deal of information about the mountain waves.

Flow on May 2, 1996 was from the west, corresponding to air flowing from left to right in Figure 3. From Figure 3, we also note that the underlying topography consists of a series of mountainous peaks, followed by a sharp drop in mean topographic elevation from 106°W to 105°W (the Continental Divide). Above this drop-off zone, strong isentropic dips are observed by the MTP in the upper troposphere, followed by sharp rises again further downstream. Very similar isentropic dips and rises have been observed in this region during the development of mountain-wave-induced downslope wind storms near Boulder. For example, Figure 15 shows isentropes inferred from *in situ* aircraft measurements in this region during the January 11, 1972 downslope windstorm event [*Lilly and Zipser*, 1972; *Lilly*, 1978]. While the amplitudes in Figure 15 are much larger, the upper-level isentropic dip and its relation to the falloff zone of the Continental Divide are very similar to those seen in the MTP isentropes in Figure 3. Similar features are also observed in model simulations [e.g., *Durran*, 1986]. Turbulence was also encountered to the right of the isentropic dips in Figure 15, due to overturning. Enhanced TEDRs were also found in similar locations for the mountain wave observed here (see Figure 5e).

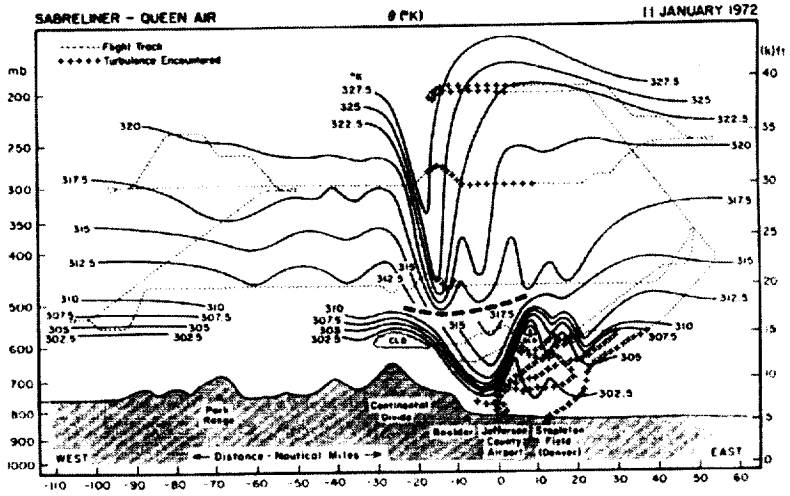

Figure 15: Isentropes measured by aircraft on January 11, 1972, during a major downslope wind storm near Boulder, Colorado. Dotted lines show flight trajectories, plus signs show regions where significant turbulence was recorded onboard the aircraft (after *Lilly* [1978]).

The larger-scale waves observed here remained quasi-stationary over a few hours, as opposed to the highly nonstationary mountain waves recently measured near Boulder and analyzed by *Ralph et al.* [1997a, 1997b]. However, shorter scale transient waves were also observed in the MMS vertical velocities (see Figures 5c), with associated small-scale turbulence. Turbulent vertical velocities occasionally showed coherent structures, as evidenced by wavelet and Fourier spectral analysis (Figures 11 and 12), due either to breaking structures in the mountain wave or remnant wake vortices resampled by the DC-8. Spectral shapes were generally consistent with earlier stratospheric studies of airborne MMS data [*Bacmeister et al.*, 1996], sometimes showing a clear transition from gravity wave to turbulence dynamics (Figure 12).

Very thin "laminated" cloud aerosol and water/ice layers were observed just below the tropopause, supporting earlier observations of sharp upper tropospheric layering from the DC-8 [e.g., *Newell et al.*, 1996] and from ground-based data [e.g., *Langford et al.*, 1997]. Upwelling by the mountain wave is identified in MTP data downstream of the mountain near flight leg D, where wave-cloud aerosol and water/ice are measured (Figures 6 and 7). This supports earlier microphysical simulations which suggested that mountain-wave-induced upwelling yielded sudden adiabatic cooling, which in turn led to heterogeneous freezing and wave cloud formation along flight leg D [*Jensen et al.*, 1998]..

2.2 Recommended Further Action

The results discussed in this result raise a number of additional questions and avenues for further research. Some of the more immediate are:

- further analysis of the May 2, 1996 data, specifically meteorological variability along other flight legs and correlations between measured constituents and winds/temperatures along the various flight tracks.
- computation of more derived data analysis products (e.g., momentum fluxes, directionality, etc.)
- similar analysis of data during the April 30, 1996 mountain wave and wave-cloud encounter over New Mexico.
- further modeling of mountain wave activity observed in these data using existing model suites.

- combined wavelet and Fourier analysis of data from other flights, to see whether the structures observed here using this method (e.g., Figure 12) can yield information on other dynamics (e.g., wake vortices, turbulent wave-breaking structures, cloudy and clear-air turbulence, short-scale gravity waves, etc.)
- further analysis of role of mesoscale variability in dispersion and advection of cloud and contrail layers.

2.3 Relation to Ultimate Objectives of the Research Contract

Significant progress has been made in the original objectives of the research project. Specifically:

- in-depth data analysis revealed a wealth of information about mountain waves, turbulence, vortices and so forth during the flight of May 2, 1996, when wave clouds formed and were intercepted by the DC-8.
- a formalized parcel advection methodology has been developed for modeling the way in which gravity waves interact with minor chemical constituents and narrow cloud/contrail layers (see Figure 13). This methodology provides a crucial theoretical framework within which more detailed studies can be formulated. Examples include condensation *via* wave-induced upwelling [e.g., *Carslaw et al.*, 1998b; *Jensen et al.*, 1998], mesoscale dispersion of contrails, interaction with large-scale dynamics and turbulence, and many other important dynamical unknowns [e.g., *Schumann et al.*, 1995].
- enhancements to the NRL/MWFM model to forecast/postcast temperature drops due to mountain wave upwelling [*Eckermann and Bacmeister*, 1998], which can now be used as inputs into global microphysical models of cloud and contrail formation [e.g., *Carslaw et al.*, 1998a, 1998b, 1999].
- progress in both Fourier-based and wavelet-based spectral analysis of airborne data has been made. Results in section 1.3 indicate that careful analysis of results from both techniques can provide very useful dynamical information on waves, turbulence, wake vortices, wave breaking, and so forth.
- comparison with model results has already occurred. NRL/MWFM simulations succeed in simulating the large mountain wave amplitudes measured on the DC-8, as well as the strong mountain wave-induced turbulence that buffeted the ER-2 during the May 2, 1996 flights. Initial UNSW/NRL mountain wave simulations generate isentropes similar to observations.
- science emanating from this research has already resulted in a significant body of publications in peer-reviewed journals [*Carslaw et al.*, 1998a, 1998b, 1999; *Bacmeister et al.*, 1998; *Eckermann*, 1998; *Eckermann et al.*, 1998]

References

Bacmeister, J. T., P. A. Newman, B. L. Gary, and K. R. Chan, An algorithm for forecasting mountain wave-related turbulence in the stratosphere, *Weather and Forecasting, 9*, 241-253, 1994.

Bacmeister, J. T., S. D. Eckermann, P. A. Newman, L. R. Lait, K. R. Chan, M. Loewenstein, M. H. Proffitt, and B. L. Gary, Stratospheric horizontal wavenumber spectra of winds, potential temperature and atmospheric tracers observed by high-altitude aircraft, *J. Geophys. Res., 101*, 9441-9470, 1996.

Bacmeister, J. T., S. D. Eckermann, A. Tsias, K. S. Carslaw, and T. Peter, Mesoscale temperature fluctuations induced by a spectrum of gravity waves: A comparison of parameterizations and their impact on stratospheric microphysics, *J. Atmos. Sci.*, (in press), 1998.

Banta, R. M., The role of mountain flows in making clouds, in *Atmospheric Process over Complex Terrain*, W. Blumen ed., *Meteor. Monographs, 23*, 229-283, 1990.

Baumgardner, D., and B. E. Gandrud, A comparison of the microphysical and optical properties of particles in an aircraft contrail and mountain wave cloud, *Geophys. Res. Lett., 25*, 1129-1132, 1998.

Borrmann, S., S. Solomon, J. E. Dye, and B. Luo, The potential of cirrus clouds for heterogeneous chlorine activation, *Geophys. Res. Lett., 23*, 2133-2136, 1996.

Brasseur, G. P., J.-F. Müller and C. Granier, Atmospheric impact of NO_x emissions by subsonic aircraft: A three dimensional model study, *J. Geophys. Res., 101*, 1423-1428, 1996.

Carslaw, K. S., M. Wirth, A. Tsias, B. P. Luo, A. Dörnbrack, M. Leutbecher, H. Volkert, W. Renger, J. T. Bacmeister, E. Reimer, and T. Peter Increased stratospheric ozone depletion due to mountain-induced atmospheric waves, *Nature, 391*, 675-678, 1998a.

Carslaw, K. S., M. Wirth, A. Tsias, B. P. Luo, A. Dörnbrack, M. Leutbecher, H. Volkert, W. Renger, J. T. Bacmeister, and T. Peter, Particle microphysics and chemistry in remotely observed mountain polar stratospheric clouds, *J. Geophys. Res., 103*, 5785-5796, 1998b.

Carslaw, K. S., T. Peter, J. T. Bacmeister and S. D. Eckermann, Widespread solid particle formation by mountain waves in the Arctic stratosphere, *J. Geophys. Res.*, (in press), 1999.

Chan, K. R., J. Dean-Day, S. W. Bowen, and T. P. Bui, Turbulence measurements by the DC-8 meteorological measurement system, *Geophys. Res. Lett., 25*, 1355-1358, 1998.

Dean-Day, J., K. R. Chan, S. W. Bowen, T. P. Bui, B. L. Gary, and M. J. Mahoney, Dynamics of Rocky Mountain lee waves observed during SUCCESS, *Geophys. Res. Lett., 25*, 1351-1354, 1998.

Demoz, B. B., D. O'Starr, K. R. Chan, and S. W. Bowen, Wavelet analysis of dynamical processes in cirrus, *Geophys. Res. Lett., 25*, 1347-1350, 1998.

Durran, D. R., Another look at downslope windstorms, Part I, On the development of analogs to supercritical flow in an infinitely deep, continuously stratified fluid, *J. Atmos. Sci., 43*, 2527-2543, 1986.

Eckermann, S. D., Isentropic advection by gravity waves: quasi-universal M^3 vertical wavenumber spectra near the onset of instability, *Geophys. Res. Lett.*, (in press), 1998.

Eckermann, S. D., and J. T. Bacmeister, Global parameterization of gravity wave temperature perturbations for chemical and microphysical models, in Proceedings of the European workshop on mesoscale processes in the stratosphere and their effect on stratospheric chemistry and microphysics, Bad Tölz, Germany, 9-11 November, (in press), 1998.

Eckermann, S. D., D. E. Gibson-Wilde, and J. T. Bacmeister,, Gravity wave perturbations of minor constituents: a parcel advection methodology, *J. Atmos. Sci., 55*, 3521-3539, 1998.

Fritts, D. C., J. R. Isler, J. H. Hecht, R. L. Walterscheid, and Ø. Andreassen, Wave breaking signatures in sodium densities and OH nightglow, 2, simulation of wave and instability structures, J. Geophys. Res., 102, 6669-6684, 1997.

Gerber, H., C. H. Twohy, B. Gandrud, A. J. Heymsfield, G. M. McFarquhar, P. J. DeMott, and D. C. Rogers, Measurements of wave-cloud microphysical properties with two new aircraft probes, *Geophys. Res. Lett., 25*, 1117-1120, 1998.

Gibson-Wilde, D. E., R. A. Vincent, C. Souprayen, S. Godin, A. Hertzog, and S. D. Eckermann, Dual lidar observations of mesoscale fluctuations of ozone and horizontal winds, *Geophys. Res. Lett., 24*, 1627-1630, 1997.

Hines, C. O., The saturation of gravity waves in the middle atmosphere. Part II: Development of Doppler-spread theory, *J. Atmos. Sci., 48*, 1360-1379, 1991.

Jensen, E. J., and O. B. Toon, Ice nucleation in the upper troposphere: Sensitivity to aerosol number density, temperature, and cooling rate, *Geophys. Res. Lett., 21*, 2019-2022, 1994.

Jensen, E. J., O. B. Toon, A. Tabazadeh, G. W. Sachse, B. E. Anderson, K. R. Chan, C. W. Twohy, B. Gandrud, S. M. Aulenbach, A. Hemysfield, J. Hallett, and B. Gary, Ice nucleation processes in upper tropospheric wave-clouds observed during SUCCESS, *Geophys. Res. Lett., 25*, 1363-1366, 1998.

Langford, A. O., M. H. Proffitt, T. E. VanZandt, and J.-F. Lamarque, Modulation of tropospheric ozone by a propagating gravity wave, *J. Geophys. Res., 101*, 26,605-26,613, 1996.

Leutbecher, M., and H. Volkert, Stratospheric temperature anomalies and mountain waves: a three-dimensional simulation using a multi-scale weather prediction model, *Geophys. Res. Lett., 23*, 3329-3332, 1996.

Lilly, D. K., A severe downslope windstorm and aircraft turbulence event induced by a mountain wave, *J. Atmos. Sci., 35*, 59-77, 1978.

Lilly, D. K., and E. J. Zipser, The Front Range windstorm of 11 January 1972 - A meteorological narrative, *Weatherwise, 25*, 56-63, 1972.

Newell, R. E., Z.-X. Wu, Y. Zhu, W. Hu, E. V. Browell, G. L. Gregory, G. W. Sachse, J. E. Collins Jr., K. K. Kelly, and S. C. Liu, Vertical fine-scale atmospheric structure measured from NASA DC-8 during PEM-West, *J. Geophys. Res., 101*, 1943-1960, 1996.

Ralph, F. M., P. J. Neiman and D. Levinson, Lidar observations of a breaking mountain wave associated with extreme turbulence, *Geophys. Res. Lett., 24*, 663-66, 1997a.

Ralph, F. M., P. J. Neiman, T. L. Keller, D. Levinson and L. Fedor, Observations, simulations and analysis of nonstationary trapped lee waves, *J. Atmos. Sci., 54*, 1308-1333, 1997b.

Schumann, U., P. Konopka, R. Baumann, R. Busen, T. Gerz, H. Schlager, P. Schulte, and H. Volkert, Estimate of diffusion parameters of aircraft exhaust plumes near the tropopause from nitric oxide and turbulence measurements, *J. Geophys. Res., 100*, 14,147-14,162, 1995.

Smith, S. A., D. C. Fritts and T. E. VanZandt, Evidence of a saturated spectrum of atmospheric gravity waves, *J. Atmos. Sci., 44*, 1404-1410, 1987.

Torrence, C., and G. P. Campo, A practical guide to wavelet analysis, *Bull. Amer. Meteor. Soc., 79*, 61-78, 1998.

Weinheimer, A. J., T. L. Campos, J. G. Walega, F. E. Grahek, B. A. Ridley, D. Baumgardner, C. H. Twohy, and B. Gandrud, Uptake of NO_y on wave-cloud ice particles, *Geophys. Res. Lett.*, 25, 1725-1728, 1998.

Appendix A:

Gravity Wave Perturbations of Minor Constituents: A Parcel Advection Methodology

Eckermann, S. D., D. E. Gibson-Wilde, and J. T. Bacmeister, *J. Atmos. Sci., 55,* 3521-3539, 1998.

Gravity Wave Perturbations of Minor Constituents: A Parcel Advection Methodology

STEPHEN D. ECKERMANN*

Computational Physics, Inc., Fairfax, Virginia

DOROTHY E. GIBSON-WILDE

Colorado Research Associates, Boulder, Colorado

JULIO T. BACMEISTER

E. O. Hulburt Center for Space Research, Naval Research Laboratory, Washington, D.C.

(Manuscript received 20 May 1997, in final form 10 February 1998)

ABSTRACT

Existing analytical models of wave-induced minor constituent fluctuations result from linearized perturbation expansions of a rate equation governing either number density or mixing ratio, whereas many numerical models now use isentropic parcel advection methods to simulate these effects. Exact relationships between the two approaches are not currently clear for gravity waves. Here, the parcel advection method is formalized and applied to derive analytical formulas for the response of vertical constituent profiles of arbitrary shape to adiabatic gravity wave displacements. These relations are compared to corresponding formulas from standard linearized perturbation analyses. Both methods accurately model perturbations produced by nondissipating hydrostatic gravity waves within idealized vertical tracer profiles. Both methods can also model wave-induced perturbations of minor constituents with shorter chemical lifetimes. This is demonstrated by using the parcel method to reproduce previous results for wave-induced fluctuations in upper-stratospheric ozone. The parcel-based approach yields more accurate models of nondissipating hydrostatic gravity wave effects on tracer distibutions with sharp spatial gradients. The authors demonstrate this by using the method to model wave-induced modulations of sporadic sodium layers in the mesosphere and of ozone laminae in the lower stratosphere. Conversely, the parcel method does not accurately model tracer density perturbations produced by nonhydrostatic waves, or situations in which the photochemical response of the constituent leads to significant diabatic feedback on the perturbing wave.

1. Introduction

High-resolution observations of minor (trace) constituents in the middle and upper atmosphere often reveal small-scale perturbations superimposed upon the mean background distribution. Such features can be produced by any number and combination of dynamical, radiative, and chemical processes. For trace constituents with long lifetimes, however, dynamics must be predominately responsible for any observed variability of that constituent's local number density over shorter timescales.

One important source of such variability is waves. For instance, vertical soundings at middle and high latitudes often reveal large enhancements or depletions of lower-stratospheric ozone (a tracer at these heights) confined to narrow (~1–2 km) vertical layers (e.g., Reid and Vaughan 1991; Bird et al. 1997). These structures, known assortedly as filaments or laminae, result from complex synoptic-scale flow patterns produced by breaking planetary Rossby waves, which yield air parcels at different stratospheric levels with vastly different histories and, hence, constituent densities (e.g., Newman and Schoeberl 1995; Orsolini et al. 1997).

Oblique oscillatory displacements of air parcels from their equilibrium positions produce accompanying density and temperature changes that can also perturb constituent profiles. Oscillations due to various types of planetary waves have been found to induce related perturbations in ozone (e.g., Newman and Randel 1988;

* Current affiliation: E. O. Hulburt Center for Space Research, Naval Research Laboratory, Washington, D.C.

Corresponding author address: Dr. Stephen D. Eckermann, Computational Physics, Inc., Suite 600, 2750 Prosperity Avenue, Fairfax, VA 22031.
E-mail: eckerman@cpi.com.

Prata 1990; Hess 1990; Randel and Gille 1991; Randel 1993; Stanford and Ziemke 1993; Wirth 1993; Ziemke and Stanford 1994; Engelen 1996) and other trace constituents (e.g., Randel 1990; Salby et al. 1990; Limpasuvan and Leovy 1995). On smaller scales, internal gravity waves can also give rise to fluctuations in constituent profiles (e.g., Reber et al. 1975; Gardner and Shelton 1985; Hedin and Mayr 1987; Sugiyama 1988; Hoegy et al. 1990; Wilson et al. 1991; Alexander and Pfister 1995; Langford et al. 1996; Bian et al. 1996; Bacmeister et al. 1997).

In fact, since observational data on middle and upper atmosphere constituents are often better and more abundant than wind and temperature data, analyses of fluctuations in long-term measurements of constituent densities have been used to infer climatologies of both planetary waves and gravity waves (e.g., Randel and Gille 1991; Senft and Gardner 1991; Randel 1993; Ziemke and Stanford 1994; Collins et al. 1996). However, since the response of constituents to waves is usually not straightforward, wave properties must be inferred from such observations by using a wave–tracer interaction model to convert the measured constituent response into a wave-related quantity. Such conversion methods have been derived to date by applying standard linearized perturbation methods of gravity wave theory to rate equations governing constituent densities or mixing ratios. Such derivations yield analytical formulas for translating conventional gravity wave oscillations into a corresponding response in the constituent profile (e.g., Dudis and Reber 1976; Chiu and Ching 1978; Gardner and Shelton 1985). Such relations can then be used to convert observed constituent fluctuations into wave-related quantities (e.g., Gardner and Voelz 1985; Randel 1990; Senft and Gardner 1991).

Recently, detailed numerical models have provided new insights into the way minor constituents respond to planetary wave and gravity wave advection (e.g., Fritts et al. 1993, 1997; Waugh et al. 1994; Roble and Shepherd 1997). Rich complex structures in minor species distributions are simulated, which often resemble observations (e.g., Fritts et al. 1993, 1997) but are not predicted by standard formulas that convert between observed tracer variability and a plane monochromatic wave. Due to their complexity, however, these models cannot as yet be used for operational extraction of wave properties from observed constituent fluctuations in the atmosphere. On the other hand, simplified versions of these models, which retained the minimum terms needed to simulate the basic effects, might lead to improved analytical models of wave-induced perturbations of minor constituent profiles.

We investigate this possibility here by considering one class of these numerical models, the so-called trajectory or parcel advection models. They have proved successful in simulating finescale tracer structures in the stratosphere, often using wind and temperature data with much coarser spatiotemporal resolution (e.g., Newman and Schoeberl 1995; Orsolini et al. 1997). The models work well because their assumptions of adiabatic motion and long chemical lifetimes are well satisified for many constituents in the lower stratosphere, where diabatic heating and turbulent diffusivities are both small. However, constituents with shorter chemical lifetimes can also be simulated by these models if a suitable parcel-based chemistry scheme is used (e.g., Lutman et al. 1997). Even in the troposphere, where diffusion and diabatic heating can be large, parcel advection models that parameterize these effects have also proved to be useful tools (e.g., Kao et al. 1995; Rind and Lerner 1996).

Given that parcel advection models often perform well even after many days of integration, the same models should also perform well if the synoptic-scale advection patterns were supplemented with wave-induced advection effects since their timescales (periods) are of the order of days for planetary waves and less than a day for gravity waves. Furthermore, since many gravity waves and planetary waves propagate conservatively through the stratosphere, an assumption of adiabatic wave-induced advection should also be well satisfied. Indeed, limited tests of gravity wave effects in such models have used this sort of approach (Pierce et al. 1994; Jensen and Thomas 1994; Carslaw et al. 1998).

Thus, we formalize the basic physical concepts underpinning parcel advection models in section 2, assess the utility of the method in gravity wave studies, then apply it in section 3 to derive analytical responses of tracers to wave-induced displacements. We compare our results throughout with corresponding results using the traditional approach of expanding state parameters into the sum of a mean and perturbation term, then isolating and linearizing the perturbation terms in the governing equations. Results of these analyses and intercomparisons are summarized in section 4.

2. Air parcel approach

This approach is based on the classic meteorological problem of vertically displacing a small dry parcel of air from its equilibrium height, where it is "well mixed" and in thermal equilibrium with the surrounding atmosphere. We assume that the displacement is small and that the parcel responds adiabatically while always maintaining a pressure equal to that of the surrounding atmosphere, following standard conventions (see, e.g., section 2.5.1 of Wallace and Hobbs 1977; section 9.1 of Iribarne and Godson 1981).

a. Conserved quantities in the parcel

1) TRACER MIXING RATIO

We consider a constituent of number density n within an air parcel of total number density n_M. For a trace constituent $n/n_M \ll 1$, any changes in n produce neg-

ligible changes in n_M, whereupon the following continuity equations apply:

$$\frac{dn_M}{dt} + n_M \nabla \cdot \mathbf{U} = 0 \tag{1a}$$

$$\frac{dn}{dt} + n \nabla \cdot \mathbf{U} = R, \tag{1b}$$

where $\mathbf{U}$ is the local velocity vector, $d/dt = \partial/\partial t + \mathbf{U} \cdot \nabla$ is a time derivative in the Lagrangian (parcel following) frame ($\partial/\partial t$ is the ground-based Eulerian time derivative), and R is the net production/loss rate for the trace constituent's number density n. Eliminating $\nabla \cdot \mathbf{U}$ between (1a) and (1b) yields (Lindzen and Goody 1965)

$$\frac{d}{dt}\left(\frac{n}{n_M}\right) = \frac{dq}{dt} = \frac{R}{n_M}, \tag{2}$$

where q is the mixing ratio of the trace constituent.

For passive trace constituents, $R \approx 0$, whereupon (2) yields

$$\frac{dq}{dt} = 0, \tag{3a}$$

or

$$q = \frac{n}{n_M} = \text{const} \tag{3b}$$

within the parcel. Thus, we get the well-known result that passive trace constituents are also tracers since the movement of a region of unique constituent mixing ratio traces the Lagrangian motion of air parcels.

2) Potential temperature

Air parcels advected by an inviscid adiabatic flow also conserve potential temperature Θ so that

$$\frac{d\Theta}{dt} = 0. \tag{4}$$

For a horizontally homogeneous atmosphere, the background potential temperature Θ is given by Poisson's relation

$$\overline{\Theta}(z) = \overline{T}(z)\left(\frac{\overline{p}(z_0)}{\overline{p}(z)}\right)^{(\gamma-1)/\gamma} = T(z, z_0), \tag{5}$$

where z is height, γ is the ratio of specific heats, $\overline{T}(z)$ is the background temperature, and $\overline{p}(z)$ is the background pressure (e.g., Turner 1973). From (5), $\overline{\Theta}(z)$ is also equal to the temperature $T(z, z_0)$ that an air parcel attains on being transported adiabatically a distance δz from its rest height z to a new height $z_0 = z + \delta z$.

3) Potential density

We can also work in terms of potential density, $D(z)$, which is defined for a horizontally homogeneous background atmosphere as

$$\overline{D}(z) = \overline{\rho}(z)\left(\frac{\overline{p}(z_0)}{\overline{p}(z)}\right)^{1/\gamma} = \rho(z, z_0) \tag{6}$$

(e.g. Turner 1973), where $\overline{\rho}(z) = M\overline{n}_M(z)$ is the background total air density at height z, $\overline{n}_M(z)$ is the background total number density, and M is the mean mass of an air molecule, assumed constant (no diffusive separation). From (6), $\overline{D}(z)$ also equals the density $\rho(z, z_0)$ that an air parcel attains on being transported adiabatically from a pressure, $\overline{p}(z)$ and density $\overline{\rho}(z)$, at its rest height z to a reference pressure $\overline{p}(z_0)$ at the displaced height $z_0 = z + \delta z$. It then follows (e.g., Wallace and Hobbs 1977) that

$$\frac{dD}{dt} = 0 \tag{7}$$

for parcels on an inviscid adiabatic flow, and thus the potential density of any parcel within such a flow is also conserved.

4) Potential tracer density

Analogously, we can also define a potential density, Δ, for a given tracer. If the constituent in question behaves as a tracer at all heights and has negligible horizontal gradients in its distribution, then, as in (6), we can define a background potential tracer density profile given by

$$\overline{\Delta}(z) = M_{tc}\overline{\nu}(z) = M_{tc}\overline{n}(z)\left(\frac{\overline{p}(z_0)}{\overline{p}(z)}\right)^{1/\gamma} = M_{tc}n(z, z_0), \tag{8}$$

where M_{tc} is the molecular mass of the trace constituent and $\overline{\nu}(z)$ is the background potential number density of the tracer. From (8), we see that $\overline{\Delta}(z)$ also equals the mass density of tracer $M_{tc}n(z, z_0)$ that an air parcel contains after being transported adiabatically from a pressure $\overline{p}(z)$ and tracer density $M_{tc}\overline{n}(z)$ at its rest height z to a reference pressure $\overline{p}(z_0)$ at the new height $z_0 = z + \delta z$. It then follows that

$$\frac{d\Delta}{dt} = \frac{d\nu}{dt} = 0 \tag{9}$$

for parcels on an inviscid adiabatic flow. Since number densities are more commonly considered in tracer studies, we shall work in terms of ν rather than Δ in subsequent analysis.

b. Perturbations due to adiabatic vertical displacements

Next we consider local responses of each conserved term to a small vertical adiabatic displacement ζ of an air parcel from its equilibrium position z_1 to a new height

$$z_2 = z_1 + \zeta, \tag{10}$$

given the standard background pressure profile

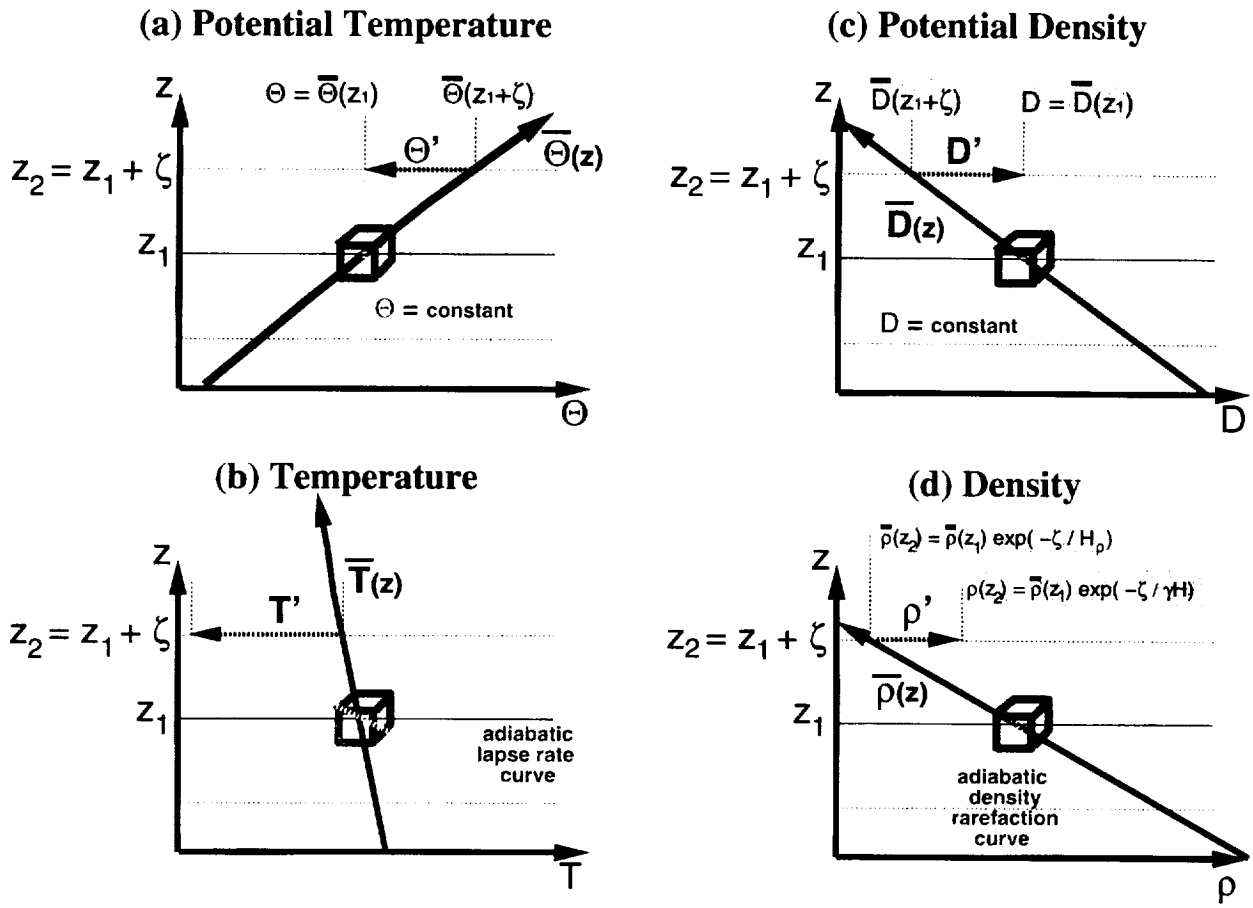

FIG. 1. Schematic diagram of response (light dotted curve) of (a) potential temperature Θ, (b) absolute temperature T, (c) potential density D, and (d) absolute density ρ in an air parcel (shown as a cube) as it is adiabatically advected a small vertical distance ζ from its equilibrium rest position z_1, where it is in thermal equilibrium with the background atmosphere. Background profiles of each quantity are plotted with solid curves.

$$\bar{p}(z_2) = \bar{p}(z_1) \exp\left(\int_{z_1}^{z_2} \frac{-dZ}{H(Z)}\right)$$

$$\approx \bar{p}(z_1) \exp\left(\frac{-\zeta}{H(z_1)}\right), \qquad (11)$$

where $H(z_1) = R\bar{T}(z_1)/g$ is the pressure scale height at height z_1, and the latter expression in (11) is sufficiently accurate for small ζ given a background temperature profile $\bar{T}(z)$ that varies slowly with height.

The formal parcel-based analysis of this problem is given in appendix A, where departures (perturbations) of parcel-based quantities from surrounding background values are derived. The basic procedure for computing these perturbations is depicted schematically in Fig. 1 for both temperature and density. In each panel in Fig. 1, an air parcel has been advected from its equilibrium height z_1 to a new height, z_2, and in each case the adiabatic response is given by moving the parcel along the light dotted "response curve." The top panels of Fig. 1 show constructions for the potential temperature and potential density: since both remain constant within the air parcel, their response curves are vertical. Corresponding constructions in terms of the absolute temperature and density are shown in the lower panels. Their response curves are given by $T(z_1, z_2)$ and $\rho(z_1, z_2)$ in (5)–(6): hereafter, it proves expedient to use the abbreviated notation $T(z_2)$ and $\rho(z_2)$ for these expressions since z_1 stays constant and the functional dependence on z_1 is implicit from (10). Background profiles are shown with thick solid curves on each plot. Perturbations are given by the difference between the adiabatically varying value within the parcel and the local background value at height z_2, as shown in Fig. 1. Using the abbreviated notation introduced above, this yields perturbation terms $\Theta'(z_2)$, $D'(z_2)$, $T'(z_2)$, and $\rho'(z_2)$.

Simplified equations for these perturbation terms follow when the displacement ζ is sufficiently small that variations in both the background profiles and the adiabatic response curves between z_1 and z_2 are approximately linear in Fig. 1. This holds so long as any curvature of these profiles occurs over vertical scales $L \gg$

ζ. Since the formal parcel relations in appendix A are height-varying exponentials, L can be conveniently characterized by the scale height H_X of the exponential relation for quantity X, so that $|\zeta/H_X| \ll 1$. When this condition is satisfied, the exponential parcel relations can be accurately approximated by retaining only the first two terms from their MacLaurin series expansions. For temperatures and densities, these truncated MacLaurin series (TMS) relations yield the instantaneous simplified perturbation relations

$$\frac{\rho'(z_2)}{\overline{\rho}(z_2)} = \frac{D'(z_2)}{\overline{D}(z_2)} = -\left(\frac{\Theta'(z_2)}{\overline{\Theta}(z_2)}\right) = -\left(\frac{T'(z_2)}{\overline{T}(z_2)}\right) = \frac{\zeta}{H_D(z_1)} = \frac{N^2(z_1)}{g}\zeta, \quad (12)$$

where

$$H_D(z_1) = H(z_1)\left(\frac{\gamma - 1}{\gamma} + \frac{\partial H(z_1)}{\partial z}\right)^{-1} = \frac{g}{N^2(z_1)} \quad (13)$$

is the potential density scale height (see appendix A). Equation (12) holds for $|\zeta/H_D| \ll 1$.

c. *Range of applicability to gravity waves*

Next we consider a sinusoidal form for the vertical parcel displacement from z_1:

$$\zeta = \zeta'(x, y, z_1, t) = \hat{\zeta}\sin(kx + ly + mz_1 - \omega t + \varphi), \quad (14)$$

where $\hat{\zeta}$ is the peak vertical displacement amplitude, φ is a (constant) phase offset, (k, l, m) is the wavenumber vector, and ω is the oscillation frequency of the parcel about its equilibrium height z_1. Considering potential temperature only for the moment, (14) and (12) yield

$$\frac{\Theta'(x, y, z_2, t)}{\overline{\Theta}(z_2)} = \frac{-N^2(z_1)}{g}\zeta'(x, y, z_1, t). \quad (15)$$

Since $\hat{\zeta}$ is small ($|\hat{\zeta}/H_D| \ll 1$), replacing the variable term $\overline{\Theta}(z_2)$ with the constant value $\overline{\Theta}(z_1)$ introduces negligible errors in (15). Then, to a good approximation, we can remove the explicit transport of parcels to z_2 so that we can reexpress the potential temperature perturbation (15) as a sinusoidal expression of the form (14) at a fixed height z_1:

$$\Theta'(x, y, z_1, t) = \hat{\Theta}(z_1)\sin(kx + ly + mz_1 - \omega t + \varphi), \quad (16)$$

where

$$\hat{\Theta}(z_1) = \frac{-N^2(z_1)}{g}\overline{\Theta}(z_1)\hat{\zeta} = -\frac{\partial\overline{\Theta}(z_1)}{\partial z}\hat{\zeta}. \quad (17)$$

Transport of parcels to z_2 is now implicit within (16) and (17). Similar relations to (17) follow from (12) and (14) for relative perturbations of potential density, density, and temperature, with peak amplitudes interrelated as

$$\frac{\hat{\rho}}{\overline{\rho}} = \frac{\hat{D}}{\overline{D}} = -\left(\frac{\hat{T}}{\overline{T}}\right) = -\left(\frac{\hat{\Theta}}{\overline{\Theta}}\right) = \frac{N^2}{g}\hat{\zeta}. \quad (18)$$

The relations (14) and (18) have the same form as the simplified polarization relations that govern a hydrostatic gravity wave of intrinsic frequency ω. This occurs because, in the linear hydrostatic limit, a gravity wave advects air parcels adiabatically (e.g., Fritts and Rastogi 1985), has a small displacement amplitude $\hat{\zeta}$ ($|\hat{\zeta}/H_D| \ll 1$), and produces a negligible pressure perturbation within displaced parcels (e.g., Gossard and Hooke 1975).

To assess the degree and range of this correspondence more quantitatively, a standard non-Boussinesq linearized perturbation derivation of the acoustic–gravity wave equations is outlined in appendix B. There it is shown that the parcel-derived polarization relations (18) are an acceptable approximation to the full acoustic–gravity wave polarization relations when the normalized quantities $|a(m, \omega)|$ and $|b(m, \omega)|$ are $\ll 1$ [see Eqs. (B10) and (B11)]. When this limit is not satisfied, wave-induced pressure perturbations become nonnegligible [see Eq. (B13)], so the parcel approach (which assumes zero pressure perturbation) becomes inaccurate. Sample calculations in appendix B show that the differences between the full acoustic–gravity wave polarization relations and the parcel-based approximations (18) are small for $\lambda_z = 2\pi/|m| \lesssim 20$ km (see Figs. B1b and B1c). Thus, we use this as an approximate upper-wavelength bound on the validity of the hydrostatic gravity wave approximation and of subsequent parcel-based derivations of gravity wave–induced minor constituent variability.

3. Gravity wave perturbations of minor constituents

We now apply the parcel-based approach to model gravity-wave-induced perturbations of minor constituent profiles. We begin by considering some simple examples and compare the parcel-based derivations (appendix A) with corresponding equations derived by a conventional linearized perturbation analysis (appendix B).

a. *Tracer with linear $\overline{q}(z)$ profile*

The parcel-based approach to this problem is depicted schematically in Fig. 2a and yields the perturbation formula (A19). Since the background profile is linear, then $\overline{q}(z_2) = \overline{q}(z_1) + (\partial\overline{q}/\partial z)\zeta'$, whereupon (A19) and the wave solution (14) yield

$$q'(x, y, z_2, t) = -\left(\frac{\partial\overline{q}}{\partial z}\right)\zeta'(x, y, z_1, t). \quad (19)$$

As for (15), if $\hat{\zeta}$ is small, then the explicit transport of parcels to z_2 can be removed in order that (19) can be

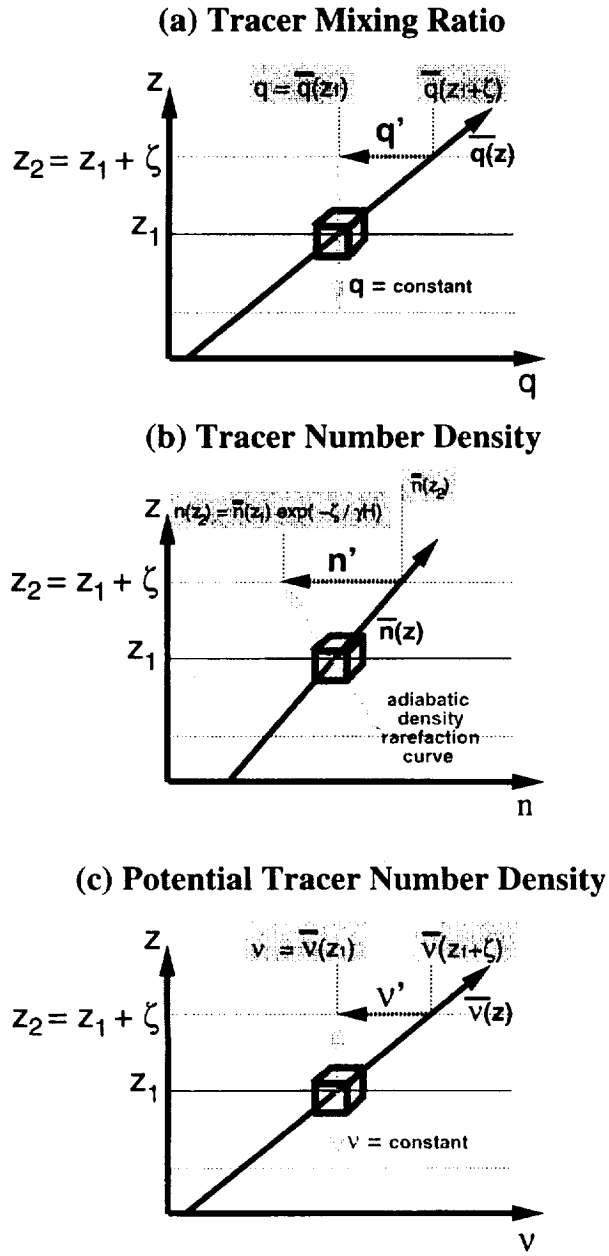

FIG. 2. As in Fig. 1 but for (a) tracer mixing ratio q, (b) tracer number density n, and (c) potential tracer number density ν of the parcel.

reexpressed as a wave solution of the form (16), with peak amplitudes related as

$$\hat{q}(z_1) = -\left(\frac{\partial \overline{q}}{\partial z}\right)\hat{\zeta}. \tag{20}$$

A standard linearized perturbation analysis of (3a) using the methodology in appendix B yields the linearized perturbation mixing ratio equation (e.g., Randel 1990)

$$-\iota\omega\hat{q} + \left(\frac{\partial \overline{q}}{\partial z}\right)\hat{w} = 0, \tag{21}$$

which, since $\hat{w} = -\iota\omega\hat{\zeta}$,, also yields (20) at a given height z_1. Thus the two approaches give identical results in this case.

b. Tracer with a linear $\overline{n}(z)$ profile

The parcel-based approach to this problem is depicted schematically in terms of tracer number density in Fig. 2b and in terms of potential tracer number density in Fig. 2c. The mathematical derivations are set out in appendix A. Because $\overline{n}(z)$ is linear and $\overline{\nu}(z)$ is approximately linear over the interval ζ, then TMS expansions of the parcel relations for tracer perturbations [e.g., (A25b)] are accurate, leading to the simplified TMS result

$$\frac{\nu'(x, y, z_2, t)}{\overline{\nu}(z_2)} = \frac{n'(x, y, z_2, t)}{\overline{n}(z_2)} \approx \frac{\zeta'(x, y, z_1, t)}{H_\nu(z_1)} \tag{22}$$

[see (A26)], where

$$H_\nu(z_1) = -\left(\frac{1}{\gamma H(z_1)} + \frac{1}{\overline{n}(z_1)}\frac{\partial \overline{n}(z_1)}{\partial z}\right)^{-1} \tag{23}$$

is the "potential tracer density scale height" by analogy to the potential *total* density scale height (13) [see (A7)]. Since $\overline{n}(z)$ is linear, the accuracy of the TMS relation (22) is controlled only by the curvature of the exponential response curve (A21) shown in Fig. 2b and so is accurate for $|\hat{\zeta}/\gamma H| \ll 1$.

As for (15) and (19), if $\hat{\zeta}$ is small, then the explicit transport of parcels to z_2 can be removed from (22) so that this equation can be reexpressed as a wave solution of the form (16) at the equilibrium height z_1, with peak amplitudes related as

$$\frac{\hat{n}(z_1)}{\overline{n}(z_1)} = -\left[\frac{1}{\gamma H(z_1)} + \frac{1}{\overline{n}(z_1)}\frac{\partial \overline{n}}{\partial z}\right]\hat{\zeta}, \tag{24}$$

where $\partial\overline{n}/\partial z$ is a constant here.

Equation (24) also follows from a linearized perturbation analysis using the nonhydrostatic isothermal acoustic–gravity wave equations of Hines (1960) (Dudis and Reber 1976; Chiu and Ching 1978; Weinstock 1978; Gardner and Shelton 1985; Sugiyama 1988). A similar analysis in appendix B shows that the full expression for nonhydrostatic acoustic–gravity waves is [see (B20)]

$$\frac{\hat{n}(z_1)}{\overline{n}(z_1)} = -\left\{\frac{1}{\gamma H(z_1)} + \frac{1}{\overline{n}(z_1)}\frac{\partial \overline{n}}{\partial z} - \frac{N^2(z_1)}{g}[a(m, \omega) + \iota b(m, \omega)]\right\}\hat{\zeta}. \tag{25}$$

Therefore (24) is valid only when $|a(m, \omega)|$ and $|b(m, \omega)|$ are negligible, which, as discussed in section 1c and

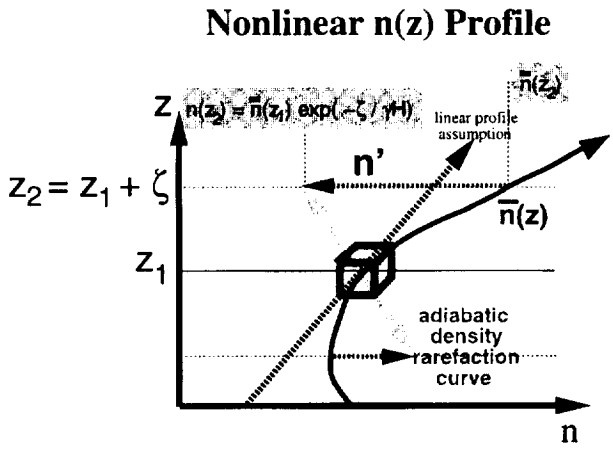

FIG. 3. As in Fig. 2b but illustrating the complications introduced by advecting a parcel across a nonlinear $\overline{n}(z)$ profile.

appendix B, holds only for hydrostatic gravity waves of $\lambda_z \lesssim 20$ km. Thus, (24) is a hydrostatic result (see also Dudis and Reber 1976), despite the fact that nonhydrostatic wave equations are needed to arrive at this result in some linearized perturbation analyses (e.g., Gardner and Shelton 1985). Note that no such caveats applied to the mixing ratio relation (20)—it holds for both hydrostatic and nonhydrostatic waves. Therefore, mixing ratio is the more straightforward quantity to consider when converting between minor constituent perturbations and displacement perturbations due to nonhydrostatic gravity waves or "tall" (fast) Kelvin waves.

c. *Tracer with a weakly nonlinear $\overline{n}(z)$ profile*

Of course tracer density profiles cannot be infinitely linear, but instead usually approximate some type of Chapman curve. If the curvature of the profile is gradual with height, then, for hydrostatic waves, (24) is often used to model wave-induced perturbations, with $\partial\overline{n}(z_1)/\partial z$ reevaluated at each new height z_1 in (24), as in (23) (e.g., Chiu and Ching 1978; Gardner and Voelz 1985; Senft and Gardner 1991). For this to be accurate, the profile needs to be approximately linear only over the limited range $z_1 \pm \hat{\zeta}$, as shown in Fig. 2b. However, this approximation may not always be sufficiently accurate for certain profile shapes, as shown schematically in Fig 3. Thus, tests of its adequacy for a given profile are required.

In the parcel-based approach, the assessment is straightforward. For an exponential $\overline{n}(z)$ profile, for instance, (22) and hence (24) are accurate for $|\hat{\zeta}/H_n| \ll 1$, from (A6a) and (A6b). For arbitrary profile shapes, we simply avoid TMS approximations and use the general parcel solution (A21), which, using (14), yields the normalized perturbation relation

$$\frac{n'(x, y, z_2, t)}{\overline{n}(z_2)} = \frac{\overline{n}(z_1)}{\overline{n}(z_2)} \exp\left(\frac{-\zeta'(x, y, z_1, t)}{\gamma H(z_1)}\right) - 1, \quad (26)$$

from (A23b), where $z_2 = z_1 + \zeta'(x, y, z_1, t)$. Note that (26) yields a nonsinusoidal solution. In terms of potential tracer density ν, this is equivalent to using (A6a) or (A8) instead of the approximate relation (A6b). Direct comparison of results using (24) and (26) then indicate whether the former equation is sufficiently accurate for modeling wave perturbations of a given $\overline{n}(z)$ profile.

Such assessments are less straightforward within the framework of a linearized perturbation analysis (e.g., Chiu and Ching 1978). Gardner and Shelton (1985) developed an iterative method for deriving higher-order corrections to (24) due to the curvature of a given $\overline{n}(z)$ profile, using perturbation expansions based on an assumed form for the solution. Their most general solution took the form

$$n(x, y, z, t) = \frac{\overline{n}\left[z - \gamma H(z) \ln\left(1 + \dfrac{A'(x, y, z, t)}{\gamma - 1}\right)\right]}{1 + \dfrac{A'(x, y, z, t)}{\gamma - 1}}, \quad (27)$$

where $A'(x, y, z, t)$ is a normalized gravity wave–induced perturbation, which, for small-amplitude waves in an isothermal atmosphere (Hines 1960), is approximately equal to the relative density perturbation of the wave [see Eq. (38) of Gardner and Shelton 1985]. It then follows that (27) corresponds approximately to the parcel solution (A21) derived in appendix A since $1 + A'(x, y, z, t)/(\gamma - 1) \approx 1 + \zeta'(x, y, z, t)/\gamma H(z)$, which in turn is a TMS expansion of $\exp[\zeta'(x, y, z, t)/\gamma H(z)]$.

Gardner and Shelton converted their solutions into perturbation formulas at a set height z_1 using MacLaurin series expansions. They derived the following extension of (24) in which the effects of both first- and second-order vertical derivatives of $\overline{n}(z)$ were retained:

$$\frac{n'(x, y, z_1, t)}{\overline{n}(z_1)} \approx \frac{-1}{\gamma - 1}\left[1 + \left(\frac{\gamma H(z_1)}{\overline{n}(z_1)}\right)\frac{\partial\overline{n}(z_1)}{\partial z}\right]\frac{\rho'(x, y, z_1, t)}{\overline{\rho}(z_1)} + \frac{1}{(\gamma - 1)^2}\left[1 + \left(\frac{3\gamma H(z_1)}{2\overline{n}(z_1)}\right)\frac{\partial\overline{n}(z_1)}{\partial z} + \left(\frac{\gamma^2 H^2(z_1)}{2\overline{n}(z_1)}\right)\frac{\partial^2\overline{n}(z_1)}{\partial z^2}\right]\left(\frac{\rho'(x, y, z_1, t)}{\overline{\rho}(z_1)}\right)^2, \quad (28)$$

where $\rho'(x, y, z_1, t)$ is the gravity wave density oscillation, which in this case is related to $\hat{\zeta}$ through (14) and (18) using isothermal relations ($\partial H(z_1)/\partial z = 0$) to evaluate $N^2(z_1)$ in (13). Like (26), Eq. (28) is also a nonsinusoidal solution.

In Fig. 4, we compare (28) with the linear profile solution (24) and the parcel solution (26). Since sodium acts as a passive tracer to gravity waves above ~85 km (e.g., Hickey and Plane 1995), we use an $\overline{n}(z)$ profile based on a Gaussian model of the mesospheric sodium layer, similar to the one considered by Gardner and Shelton (1985). The profile is plotted as the thick light curve in Figs. 4b and 4e. We perturb this profile with a hydrostatic gravity wave (14) of vertical wavelength λ_z = 10 km, $\hat{\zeta}$ = 800 m (both representative mesospheric values), and constant phase φ_0. Sample waves are shown in Figs. 4a and 4d as a function of height z at a given location (x_0, y_0) at two different times t. The corresponding perturbations to the background tracer profile are plotted in Figs. 4b and 4e, and the normalized perturbations are isolated and plotted in Figs. 4c and 4f for the parcel solution (26) and the perturbation formulas (24) and (28). The parcel solution (26) is also replotted with a dotted curve in Figs. 4c and 4f at the undisturbed height $z = z_1$, instead of at the perturbed height $z = z_2 = z_1 + \zeta'(x_0, y_0, z_1, t)$ (solid curve), to help separate the deviations that arise due to different physical locations for each parcel (i.e., differences in z_2 and z_1) and those due to incomplete characterization of the effects of mean profile curvature.

We see in Figs. 4c and 4f that the simple relation (24) is reasonably accurate here but that the higher-order correction (28) brings the solution closer to the parcel solution (26). The results in Fig. 4 also show many well-known features of wave-induced fluctuations of tracer number density profiles; for example, that the wave response is always larger on the underside of the layer than on the topside (e.g., Chiu and Ching 1978; Weinstock 1978). This feature is easily appreciated in a parcel analysis by noting that all points on the unperturbed Gaussian profile in Figs. 4b and 4e follow the "adiabatic rarefaction" response curve (A21) when vertically advected, as shown in Fig. 2b. This clearly yields greater deviations from the background profile on the bottom side of the layer than on the top side. Also evident in Figs. 4c and 4f is the well-known half-wavelength phase flip across the layer peak (Gardner and Shelton 1985).

d. Tracer with a strongly nonlinear $\overline{n}(z)$ profile

Tracer layers in the middle atmosphere often deviate significantly from the smoothly curved profiles considered in Fig. 4. For example, the mesospheric sodium layer sometimes develops a large narrow spike of enhanced Na density, known as a sudden (or sporadic) sodium layer (SSL) (Clemesha et al. 1980; Kwon et al. 1988; Nagasawa and Abo 1995). Similarly, ozone profiles in the lower stratosphere near the edge of the polar vortex often contain large narrow enhancements or depletions, known as "laminae" (e.g., Reid and Vaughan 1991). Neither the linearized perturbation relation (24) nor its second-order correction (28) are sufficiently accurate for modeling wave-induced effects within such profiles.

However, parcel-based methods can be used since they require no prior assumptions about the shape of the background vertical profile. To illustrate this, we simulate an SSL by adding a narrow Gaussian layer to the original Gaussian in Fig. 4, choosing its parameters to resemble the "typical" SSL considered by Cox et al. (1993). The resultant profile is the thick light curve shown in each panel of Fig. 5. We perturb this profile with the same wave as in Fig. 4. Solid curves in Fig. 5 show the perturbed profile as calculated using the parcel solution (A21) and the wave oscillation (14), with each panel showing results at six successive equispaced time values t spanning a full wave period $2\pi/\omega$. We see that the SSL is not only advected up and down by the wave, but is also periodically expanded (Fig. 5b) and compressed (Fig. 5e).

Detailed features of the response are more easily seen in surface renderings of successive profiles, shown in Fig. 6. Figure 6a shows the periodic oscillation of the SSL peak and the downward movement of wave phase fronts above and below the SSL, the latter associated with an approximately linear wave response within the basic Gaussian profile (Figs. 4c and 4f). The SSL is focused upon in Fig. 6b, which shows a sinusoidal advection of its peak value and periodic contraction and expansion of its width.

Figure 7 shows a representative lower-stratospheric ozone profile with a lamina superimposed (thick light curve), based on the lidar observations of Gibson-Wilde et al. (1997). Like sodium, ozone has a long chemical lifetime at these heights and therefore acts as a tracer to gravity wave motions. We perturb the profile with a gravity wave of $\hat{\zeta}$ = 200 m and λ_z = 2.3 km, choices based on the gravity wave detected and characterized by Gibson-Wilde et al. (1997) at ~12–18 km during their ozone measurement. Parcel results using (A21) for a full wave cycle are shown with solid curves in Fig. 7. Again, we see not only vertical advection of the lam-

→

FIG. 4. Perturbations of a Gaussian number density profile $\overline{n}(z)$ [thick light curve in (b) and (e)] are plotted in (b) and (e), as produced by the gravity wave shown above it in (a) and (d), respectively. Corresponding relative perturbations are plotted below in (c) and (f). Results using parcel advection methods (solid and dotted curves) are compared to the results (24) (dashed curve) and (28) (broken curve) based on linearized perturbation solutions. The thick light curves in (c) and (f) show the asymmetric amplitude envelope of the parcel solution, given from (A23a) by $[\overline{n}(z)/\overline{n}(z \pm \hat{\zeta})] \exp(\mp\hat{\zeta}/\gamma H) - 1$. An isothermal atmosphere of H = 7 km was used.

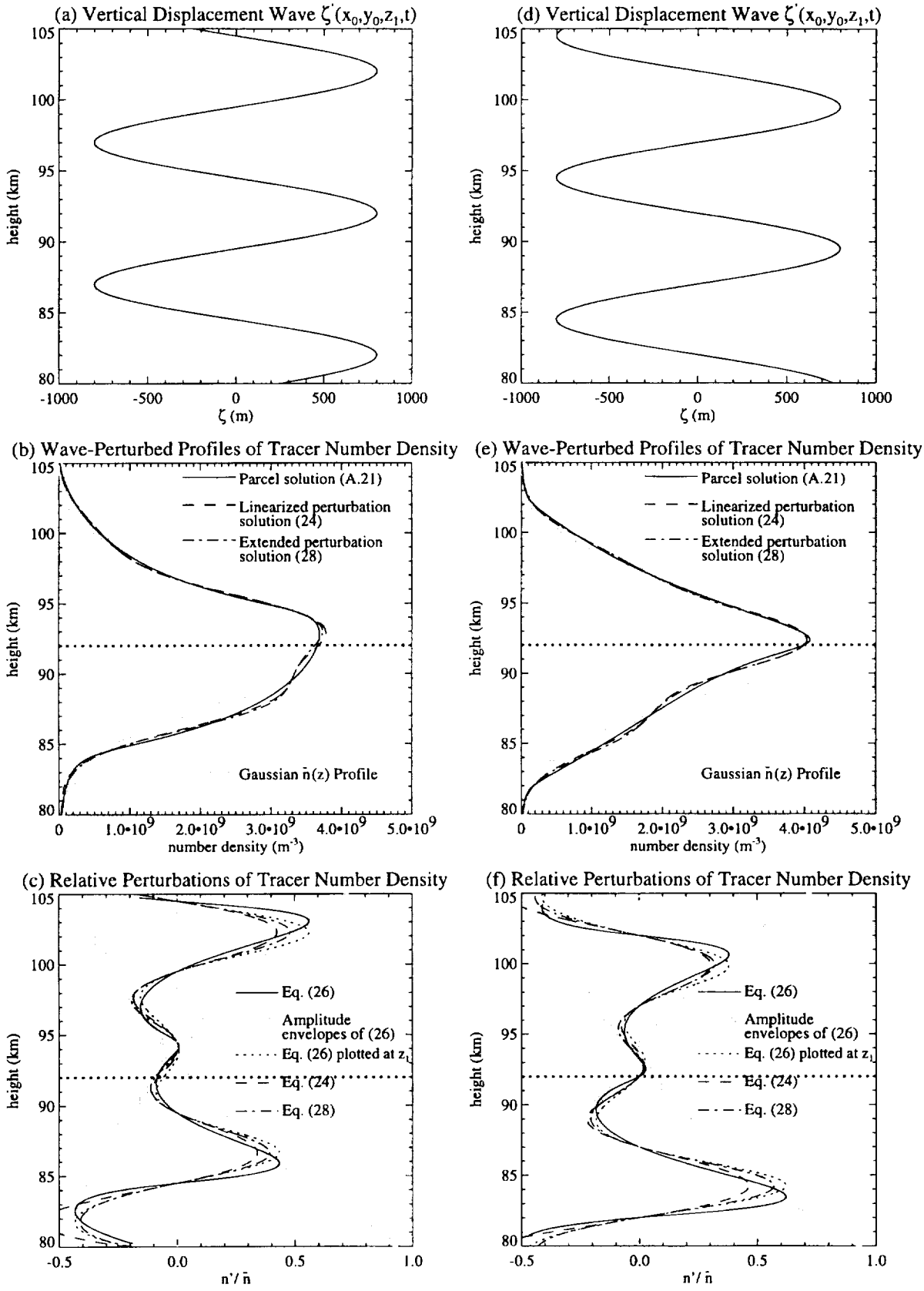
(a) Vertical Displacement Wave $\zeta'(x_0,y_0,z_1,t)$
height (km)
105
100
95
90
85
80
-1000
-500
0
500
1000
ζ (m)
(d) Vertical Displacement Wave $\zeta'(x_0,y_0,z_1,t)$
height (km)
ζ (m)
(b) Wave-Perturbed Profiles of Tracer Number Density
Parcel solution (A.21)
Linearized perturbation solution (24)
Extended perturbation solution (28)
Gaussian $\bar{n}(z)$ Profile
height (km)
0
$1.0\cdot10^9$
$2.0\cdot10^9$
$3.0\cdot10^9$
$4.0\cdot10^9$
$5.0\cdot10^9$
number density (m^{-3})
(e) Wave-Perturbed Profiles of Tracer Number Density
Parcel solution (A.21)
Linearized perturbation solution (24)
Extended perturbation solution (28)
Gaussian $\bar{n}(z)$ Profile
height (km)
number density (m^{-3})
(c) Relative Perturbations of Tracer Number Density
Eq. (26)
Amplitude envelopes of (26)
Eq. (26) plotted at z_1
Eq. (24)
Eq. (28)
height (km)
-0.5
0.0
0.5
1.0
$n'/\bar{n}$
(f) Relative Perturbations of Tracer Number Density
Eq. (26)
Amplitude envelopes of (26)
Eq. (26) plotted at z_1
Eq. (24)
Eq. (28)
height (km)
$n'/\bar{n}$

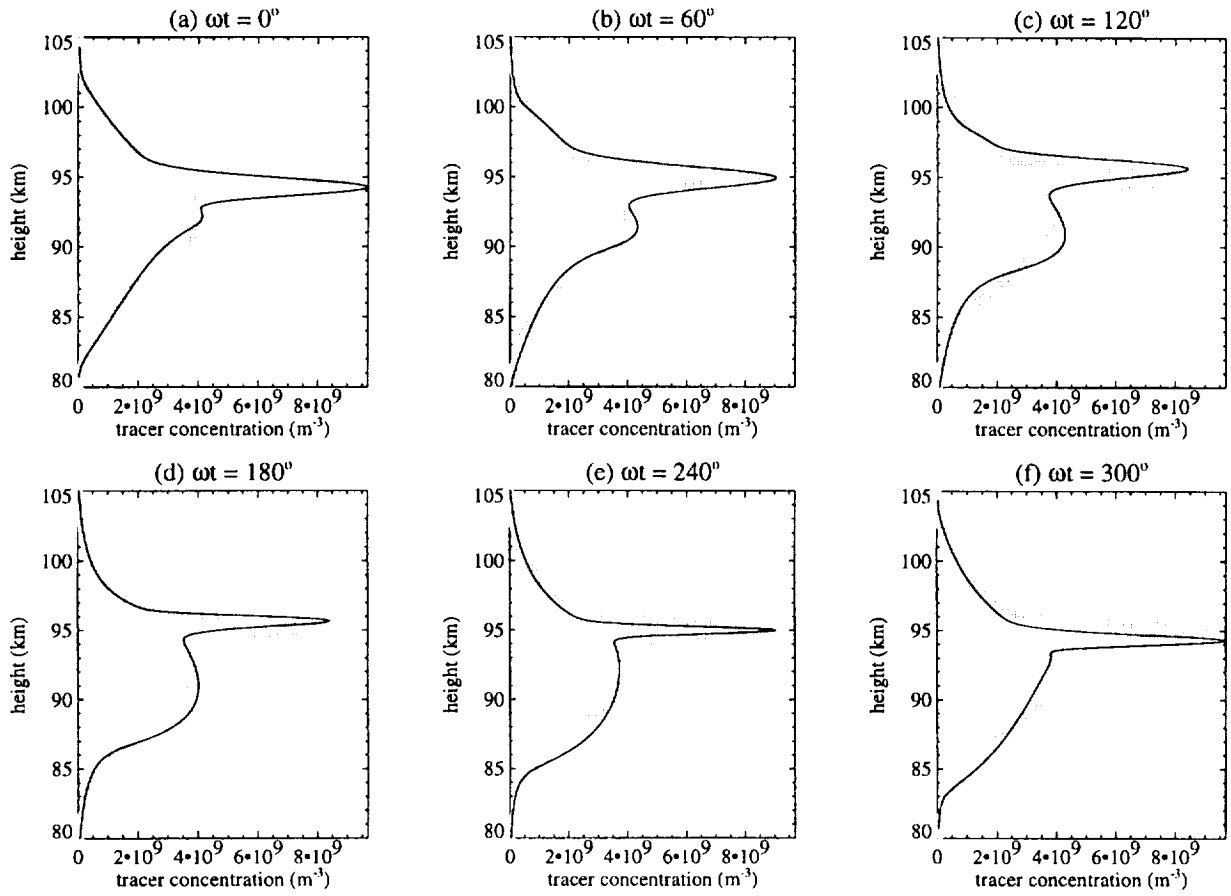

FIG. 5. Sequence of six profiles (at equispaced times t spanning one wave period) of a wave-perturbed Na layer (solid curve) as in Fig. 4, but with an SSL inserted at 95 km (based on Fig. 1 of Cox et al. 1993). The thick light curve shows the unperturbed profile in each case.

ina, but compression and expansion of its width as well, features that are more obvious in the corresponding surface plot in Fig. 8. Effects such as these may account for some of the standard deviation in mean magnitudes and widths of ozone laminae found in collated ozonesonde data (e.g., Fig. 7 of Reid and Vaughan 1991), as well as variability of other narrow atmospheric layers: for example, tropospheric chemical layers (Newell et al. 1996), cloud structures (e.g., Carslaw et al. 1998), polar mesosphere summer echoes (e.g., Fig. 1 of Rüster et al. 1996), and stratospheric aerosols (Shibata et al. 1994; Hansen and Hoppe 1997). Figure 8 also shows the regular downward movement of wave phase fronts above and below the lamina, where the response approximates a linear wave solution of the form (24).

e. *Three-dimensional gravity wave advection of a tracer*

The features that produce laminated ozone profiles tend to occur in long narrow streamers of meandering air, which lead to large background ozone gradients not only vertically, but also horizontally (e.g., Waugh et al. 1994; Orsolini et al. 1997). These gradients can be important when attempting to isolate wave-related structures in ozone measured within such environments (e.g., Danielsen et al. 1991; Teitelbaum et al. 1996; Bacmeister et al. 1997; Gibson-Wilde et al. 1997). Again, the approximate relations (24) and (28) cannot accurately simulate the effects of gravity waves on such three-dimensional tracer distributions.

The parcel-based theory in appendix A assumed no horizontal gradients in the background tracer profile and cannot be directly applied here. However, the analysis is easily extended to accommodate full three-dimensional wave-induced displacements $[\chi'(x_i, y_i, z_i, t), \eta'(x_i, y_i, z_i, t), \zeta'(x_i, y_i, z_i, t)]$ of a collection of parcels, i ($i = 1, 2, 3, \cdots$) at equilibrium positions (x_i, y_i, z_i) within an arbitrary three-dimensional tracer distribution $\overline{q}(x, y, z)$.

The mixing ratio response (A19) generalizes to

$$q[x_i + \chi'(x_i, y_i, z_i, t), y_i + \eta'(x_i, y_i, z_i, t), z_i + \zeta'(x_i, y_i, z_i, t)] = \overline{q}(x_i, y_i, z_i), \quad (29)$$

which, as discussed in section 3b, holds for hydrostatic

and nonhydrostatic waves. If we can assume that background isentropic surfaces are horizontal, then a corresponding extension of (A21) yields the number density response

$$n[x_i + \chi'(x_i, y_i, z_i, t), y_i + \eta'(x_i, y_i, z_i, t), z_i + \zeta'(x_i, y_i, z_i, t)] = \overline{n}(x_i, y_i, z_i) \exp\left(\frac{-\zeta'(x_i, y_i, z_i, t)}{\gamma H(z_i)}\right) \quad (30)$$

for a background number density distribution $\overline{n}(x, y, z)$.

As discussed in section 3b, (30) is accurate for hydrostatic gravity waves only. In environments where large narrow horizontal gradients in background potential temperatures/densities also arise, additional compression and expansion occurs as parcels are horizontally advected by the wave. In this situation, not only must the exponential in (30) be modified to account for this extra horizontal compression/expansion, but extended wave equations may be needed that incorporate concomitant modifications to the wave motion (e.g., Lamb and Shore 1992). Since background isentropes rarely tilt from the horizontal by more than a few degrees, then (30) should adequately describe gravity wave–induced perturbations of a three-dimensional distribution of tracer number densities in most circumstances.

It should be noted that the parcel relations (29) and (30) are Lagrangian expressions. A typical application, then, would be in supplementing synoptic-scale parcel advection models with oscillatory gravity wave advection effects (e.g., Pierce et al. 1994). The Eulerian tracer perturbations that such simulations will produce (e.g., fluctuations in vertical tracer profiles) will be quite complicated in general.

f. *Gravity wave perturbations of shorter-lived constituents*

The parcel-based approach can also be used for shorter-lived constituents. We illustrate this by using it to reproduce some well-known results for ozone.

While the lower-stratospheric ozone in Figs. 7–8 acts as a tracer, the ozone production/loss term in (1b), R_{O_3}, becomes nonnegligible above ~25–30 km. Assuming Chapman photochemistry, then

$$R_{O_3} \approx 2J_{O_2}n_{O_2} - \frac{2k_{O_3}J_{O_3}n_{O_3}^2}{k_{O_2}n_M n_{O_2}}, \quad (31)$$

where n_x is the number density of constituent x, J_x is its photolysis rate, and k_x is its recombination rate (Brasseur and Solomon 1984). As shown in appendix C, applying a parcel-based analysis to (2) and (31) yields a linearized response of the photochemical term R_{O_3} to an adiabatic vertical displacement of the parcel of the form

$$\frac{dq_{O_3}(z_2)}{dt} = -\overline{B}(z_2)q'_{O_3}(z_2) - \overline{C}(z_2)T'(z_2), \quad (32)$$

for small vertical displacements ζ, where $q_{O_3}(z_2) = \overline{q}_{O_3}(z_2) + q'_{O_3}(z_2)$ from (A19) and $T'(z_2)$ is the TMS temperature perturbation (A13). Since $\overline{R}_{O_3}(z) \approx 0$, then, for a linear $\overline{q}(z)$ profile,

$$\frac{d\overline{q}_{O_3}(z_2)}{dt} = \left(\frac{\partial \overline{q}_{O_3}}{\partial z}\right)w(z_2), \quad (33)$$

where $w(z_2) = d\zeta/dt$ is the vertical velocity of the parcel at z_2 (see Fig. 2a). Thus (32) and (33) yield

$$\frac{dq'_{O_3}(z_2)}{dt} + w(z_2)\left(\frac{\partial \overline{q}_{O_3}}{\partial z}\right) = -\overline{B}(z_2)q'_{O_3}(z_2) - \overline{C}(z_2)T'(z_2). \quad (34)$$

This equation was first derived by Lindzen and Goody (1965) using a linearized perturbation expansion of (2) and (31).

We now substitute the wave solution (14). If $\hat{\zeta}$ is small and the vertical variation of background quantities in (34) is gradual (as assumed in appendix C) and approximately linear over the interval $z_1 \pm \hat{\zeta}$, then explicit parcel transport to z_2 can be removed so that the linearized mixing ratio and temperature perturbations in (34) can also be expressed as wave solutions of the form (14) and (16). Substitution of those solutions into (34) yields, with the help of (21), (A5), and (13), the peak amplitude relation

$$\left(1 - \iota\frac{\overline{B}(z_1)}{\omega}\right)\hat{q}_{O_3}(z_1) = \left(\frac{\partial \overline{q}_{O_3}(z_1)/\partial z}{\partial \overline{T}(z_1)/\partial z + \Gamma_a} + \iota\frac{\overline{C}(z_1)}{\omega}\right) \times \hat{T}(z_1), \quad (35)$$

where Γ_a is the dry-adiabatic lapse rate. This is the basic ozone–temperature relation derived for Kelvin waves by Randel (1990). It illustrates the two limiting cases of the response. For $\omega^2 \gg \overline{B}^2$ and $(\overline{C}/\omega)^2 \ll [(\partial \overline{q}_{O_3}/\partial z)/(\partial \overline{T}/\partial z + \Gamma_a)]^2$, terms on the right of (34) are small while terms on the left are large and dominate, so (35) approximates the tracer solution (20). For $\omega^2 \ll \overline{B}^2$ and $(\overline{C}/\omega)^2 \gg [(\partial \overline{q}_{O_3}/\partial z)/(\partial \overline{T}/\partial z + \Gamma_a)]^2$, photochemistry dominates so that terms on the right-hand side of (34) are much larger than the parcel transport terms on the left. In this latter case, (35) tends toward the photochemistry-dominant limit

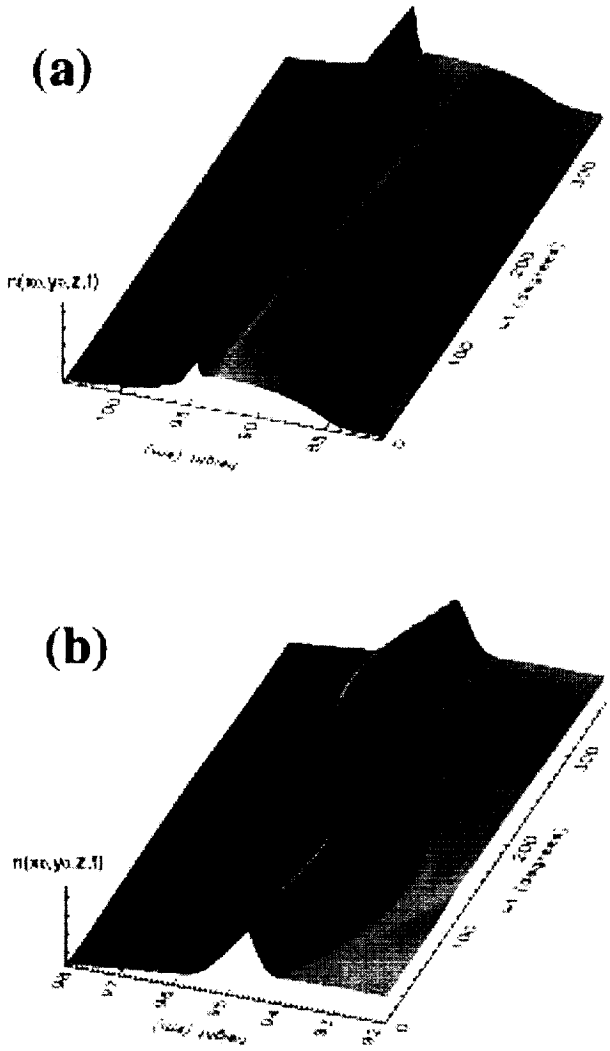

FIG. 6. Time–height surface rendering of the perturbed Na number density response in Fig. 5. Both plots span one wave period. Panel (a) shows variations over the full height range of the Na layer, while (b) focuses on the SSL.

$$\hat{q}(z_1) = -\left(\frac{\overline{C}(z_1)}{\overline{B}(z_1)}\right)\hat{T}(z_1), \tag{36}$$

which also follows on setting the left-hand side of (34) to zero.

This parcel-based analysis assumes adiabatic parcel motion, whereas the perturbation $q'_0(z_2)$ also produces a diabatic heating/cooling perturbation in the potential temperature equation. However, Zhu and Holton (1986) show that this leads to very minor departures from adiabaticity for hydrostatic gravity waves. Thus parcel-based analyses also work well in simulating (hydrostatic) gravity wave–induced perturbations of constituents with short chemical lifetimes, so long as the perturbed chemical response does not lead to significant diabatic damping of the wave; otherwise, a linearized perturbation analysis should be pursued (e.g., Zhu and Holton 1986).

4. Summary and conclusions

This study has formalized the parcel advection method, applied it to gravity waves, and compared its findings with standard results from linearized perturbation expansions of the governing equations. The combined results of section 3 have shown that the two approaches are equivalent in most circumstances. However, we also identified certain situations in which one or the other method gave more accurate results.

The parcel-based method becomes inaccurate when simulating perturbations of tracer density profiles by nonhydrostatic gravity waves. For shorter-lived constituents, the parcel method also becomes inaccurate if the wave-induced photochemical response produces a significant diabatic feedback on the wave. In these instances, the results from traditional linearized perturbation analysis should be used instead.

On the other hand, the parcel-based approach is the better method for modeling hydrostatic gravity wave perturbations of tracers with sharp spatial gradients in their background distribution. We illustrated this by using it to model wave-induced modulations of sporadic sodium layers and ozone laminae (Figs. 5–8).

While we have restricted attention here to gravity waves, the parcel methodology described here can also be applied to other types of waves, such as free and forced Rossby waves, mixed Rossby–gravity waves, Kelvin waves, and tides. For some of these waves, both meridional and vertical wave displacements are necessary to simulate their effects on tracers (e.g., Randel 1993; Stanford and Ziemke 1993). Parcel advection models have already been used extensively to simulate the effects of stationary Rossby waves on stratospheric tracer distributions.

Acknowledgments. Thanks to Mary Anderson, Andrea Hollin, Jane Ford, DuRene Brimer, and "Chap" Chappell at Computational Physics, Inc., and Mary-Ann Lindsey at the Naval Research Laboratory, Washington, D.C., for their help with the administration and public release of this paper. Thanks also to Chet Gardner, Richard Walterscheid, and an anonymous reviewer for helpful comments on the manuscript. SDE also thanks Colin Hines for comments on an earlier draft and for helping to resolve SDE's misunderstandings of some of his earlier work. This research was partially supported by the Office of Naval Research, Washington, D.C., and Contract NAS5-97247 of NASA's Atmospheric Effects of Aviation/Subsonic Assessment Program.

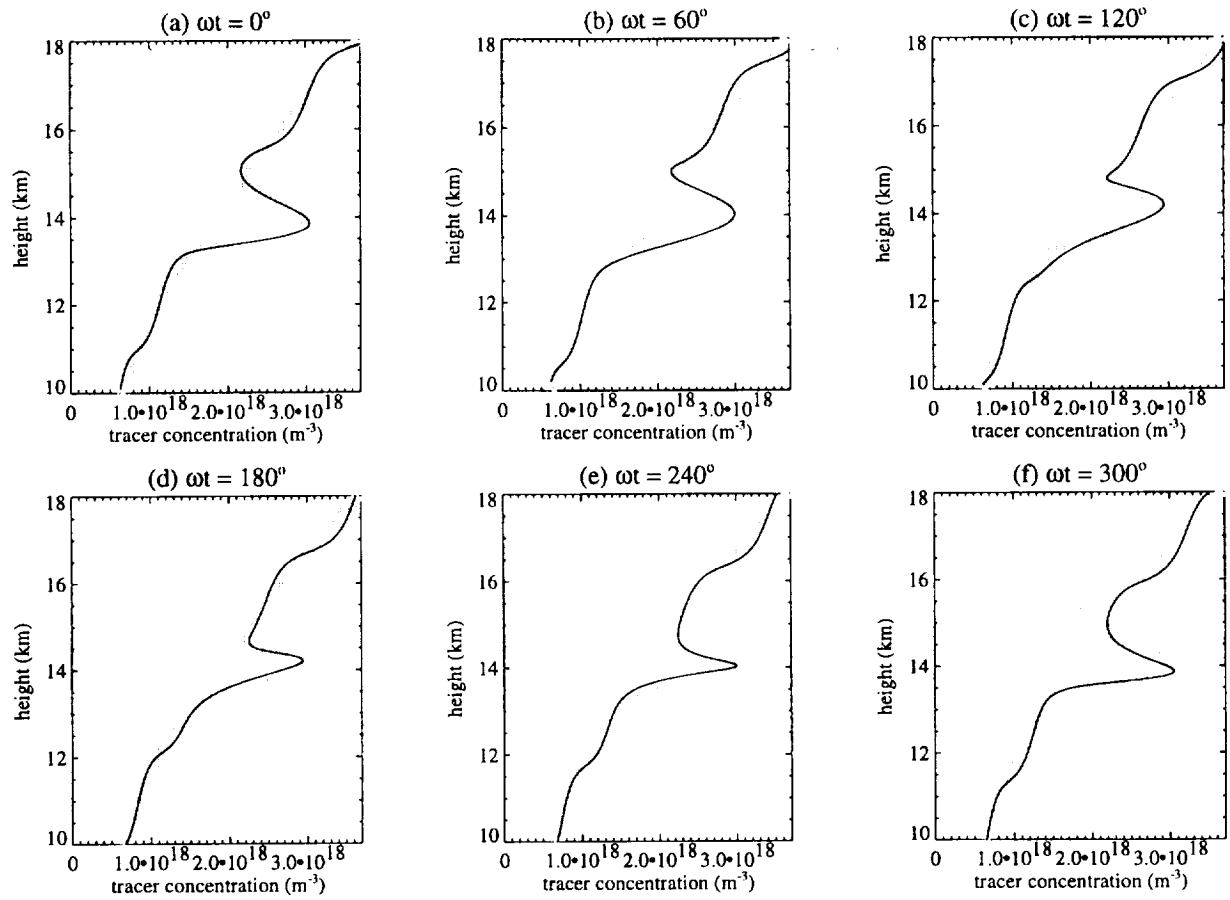

FIG. 7. As in Fig. 5 but using a representation of the ozone layer based on the data of Gibson-Wilde et al. (1997), with a lamina at 14 km. Thick light curves show the unperturbed profile. Solid curves show perturbed profiles due to a gravity wave of $\lambda_z = 2.3$ km and $\hat{\zeta} = 200$ m.

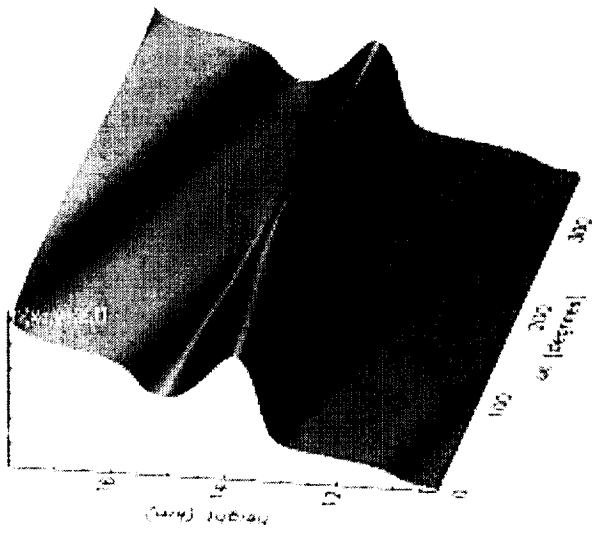

FIG. 8. As in Fig. 6a but showing the ozone number density response from Fig. 7.

APPENDIX A

Perturbation Formulas Using the Parcel Methodology

a. *Background profiles*

The ideal gas law and the altimeter equation (11) yield the standard background density relation

$$\overline{\rho}(z_2) = \overline{\rho}(z_1)\frac{\overline{T}(z_1)}{\overline{T}(z_2)}\exp\left(\frac{-\zeta}{H(z_1)}\right) \approx \overline{\rho}(z_1)\exp\left(\frac{-\zeta}{H_\rho(z_1)}\right), \tag{A1}$$

where

$$H_\rho(z_1) \approx H(z_1)\left(1 + \frac{\partial H(z_1)}{\partial z}\right)^{-1} \tag{A2}$$

is the density scale height. On invoking (5) and (6) at z_1 and z_2, then, with the aid of (11), (A1) and (A2), background potential temperature varies with height as

$$\overline{\Theta}(z_2) = \overline{\Theta}(z_1)\frac{\overline{T}(z_2)}{\overline{T}(z_1)}\exp\left(\frac{(z_2 - z_1)(\gamma - 1)}{\gamma H(z_1)}\right) \quad \text{(A3a)}$$

$$\approx \overline{\Theta}(z_1)\exp\left(\frac{\zeta}{H_D(z_1)}\right), \quad \text{(A3b)}$$

while background potential density varies with height as

$$\overline{D}(z_2) = \overline{D}(z_1)\frac{\overline{\rho}(z_2)}{\overline{\rho}(z_1)}\exp\left(\frac{(z_2 - z_1)}{\gamma H(z_1)}\right) \quad \text{(A4a)}$$

$$\approx \overline{D}(z_1)\exp\left(\frac{-\zeta}{H_D(z_1)}\right), \quad \text{(A4b)}$$

where

$$H_D(z_1) = H(z_1)\left(\frac{\gamma - 1}{\gamma} + \frac{\partial H(z_1)}{\partial z}\right)^{-1} = \frac{g}{N^2(z_1)} \quad \text{(A5)}$$

is the potential density scale height, g is gravitational acceleration, and $N(z_1)$ is the background Brunt–Väisälä frequency at height z_1.

From (8), analogous relations for the background potential number density of a given passive trace constituent are

$$\overline{\nu}(z_2) = \overline{\nu}(z_1)\frac{\overline{n}(z_2)}{\overline{n}(z_1)}\exp\left(\frac{(z_2 - z_1)}{\gamma H(z_1)}\right) \quad \text{(A6a)}$$

$$\approx \overline{\nu}(z_1)\exp\left(\frac{-\zeta}{H_\nu(z_1)}\right), \quad \text{(A6b)}$$

where

$$H_\nu(z_1) = -H(z_1)\left(\frac{1}{\gamma} + \frac{H(z_1)}{\overline{n}(z_1)}\frac{\partial \overline{n}(z_1)}{\partial z}\right)^{-1} \quad \text{(A7)}$$

is the potential tracer density scale height. The simplified relation (A6b) is accurate when height variations of the $\overline{n}(z_1)$ profile are approximately exponential over the interval ζ. For small ζ, (A6b) is a good approximation whenever $\overline{n}(z)$ varies over a typical vertical length scale $L \gg \zeta$. However, while background temperatures in (A1) and background densities in (A4a) usually obey such conditions, $\overline{n}(z)$ profiles in (A6a) often do not (see sections 3c and 3d), whereupon (A6a) or the integrated expression

$$\overline{\nu}(z_2) \approx \overline{\nu}(z_1)\exp\left(\int_{z_1}^{z_2 = z_1 + \zeta}\frac{-dZ}{H_\nu(Z)}\right) \quad \text{(A8)}$$

must be used. Note that the reformulation of (A6a) into a fully exponential form (A6b) and (A8) is similar to the approach taken by Lindzen (1981) in parameterizing the variation with height of WKB gravity wave equations [see his Eqs. (11) and (12)].

b. Temperature perturbations

Figure 1a constructs the perturbation of potential temperature produced by the adiabatic vertical displacement ζ of an air parcel from its equilibrium position z_1, as discussed in section 2b. Since Θ in the parcel is conserved, the displacement produces a perturbation from the background profile at height z_2 of

$$\Theta'(z_2) = \overline{\Theta}(z_1) - \overline{\Theta}(z_2). \quad \text{(A9)}$$

From (A3b) and (A5), this implies a normalized perturbation:

$$\frac{\Theta'(z_2)}{\overline{\Theta}(z_2)} = \exp\left(\frac{-\zeta}{H_D(z_1)}\right) - 1 \quad \text{(A10a)}$$

$$\approx \frac{-\zeta}{H_D(z_1)} = \frac{-N^2(z_1)}{g}\zeta$$

$$= -\frac{1}{\overline{\Theta}(z_1)}\frac{\partial \overline{\Theta}(z_1)}{\partial z}\hat{\zeta}, \quad \text{(A10b)}$$

where (A10b) follows from retaining the first two terms of the MacLaurin series expansion of the exponential in (A10a) and is accurate for small ζ (i.e., $|\zeta/H_D(z_1)| \ll 1$). This simplification is referred to hereafter as a truncated MacLaurin series (TMS) expansion and from (A10b) is clearly accurate when the background profile $\overline{\Theta}(z)$ is approximately linear between z_1 and z_2.

The absolute temperature response is depicted in Fig. 1b. Using (5) and (11), the temperature of the displaced parcel becomes

$$T(z_2) = \overline{T}(z_1)\exp\left(\frac{-\zeta(\gamma - 1)}{\gamma H(z_1)}\right) \quad \text{(A11a)}$$

$$\approx \overline{T}(z_1) - \frac{\zeta g}{C_p}, \quad \text{(A11b)}$$

where C_p is the mass specific heat at constant pressure. Equation (A11b) follows from a TMS expansion of (A11a) and reproduces the familiar result that the parcel temperature varies according to the (dry) adiabatic lapse rate $\Gamma_a = g/C_p$ for small ζ. This yields a temperature perturbation

$$T'(z_2) = T(z_2) - \overline{T}(z_2) \quad \text{(A12)}$$

and a relative perturbation, according to (A5), (A11a), and (A12), of

$$\frac{T'(z_2)}{\overline{T}(z_2)} = \frac{\overline{T}(z_1)}{\overline{T}(z_2)}\exp\left(\frac{-\zeta(\gamma - 1)}{\gamma H(z_1)}\right) - 1$$

$$\approx \exp\left(\frac{-\zeta}{H_D(z_1)}\right) - 1$$

$$\approx \frac{-\zeta}{H_D(z_1)} = \frac{-N^2(z_1)}{g}\zeta, \quad \text{(A13)}$$

using a TMS expansion of the exponential. Thus the

relative perturbations of absolute and potential temperature are equal for small ζ.

c. Density perturbations

Figure 1c constructs the perturbation of potential density produced by the same adiabatic vertical displacement ζ of an air parcel from its equilibrium position z_1. Since D in the parcel is conserved, then, as in (A9),

$$D'(z_2) = \overline{D}(z_1) - \overline{D}(z_2). \tag{A14}$$

From (A4b) and (A5), (A14) implies a normalized perturbation,

$$\frac{D'(z_2)}{\overline{D}(z_2)} = \exp\left(\frac{\zeta}{H_D(z_1)}\right) - 1 \tag{A15a}$$

$$\approx \frac{\zeta}{H_D(z_1)} = \frac{N^2(z_1)}{g}\zeta, \tag{A15b}$$

where (A15b) follows from a TMS expansion of (A15a).

Figure 1d shows the corresponding construction for the density perturbation. Using (6) and (11), the density of the adiabatically displaced parcel responds according to

$$\rho(z_2) = \overline{\rho}(z_1)\exp\left(\frac{-\zeta}{\gamma H(z_1)}\right), \tag{A16}$$

which, by analogy to the adiabatic lapse rate for temperature (A11b), we refer to here as the adiabatic rarefaction curve. This yields a density perturbation

$$\rho'(z_2) = \rho(z_2) - \overline{\rho}(z_2), \tag{A17}$$

which, with the aid of (A1), (A2), (A5), and (A16), yields to a relative density perturbation of

$$\frac{\rho'(z_2)}{\overline{\rho}(z_2)} = \frac{\rho(z_2)}{\overline{\rho}(z_2)} - 1$$

$$= \exp\left(\frac{\zeta}{H_D(z_1)}\right) - 1 \tag{A18a}$$

$$\approx \frac{\zeta}{H_D(z_1)} = \frac{N^2(z_1)}{g}\zeta, \tag{A18b}$$

using a TMS expansion of (A18a).

d. Tracer perturbations

Figure 2a constructs the perturbation mixing ratio q' induced by the adiabatic vertical displacement ζ of a parcel from its equilibrium height z_1 in an atmosphere containing a tracer with a background vertical profile $\overline{q}(z)$. Since q in the parcel is conserved according to (3), then

$$q'(z_2) = q(z_2) - \overline{q}(z_2)$$

$$= \overline{q}(z_1) - \overline{q}(z_2) \tag{A19}$$

and

$$\frac{q'(z_2)}{\overline{q}(z_2)} = \frac{\overline{q}(z_1)}{\overline{q}(z_2)} - 1. \tag{A20}$$

Since $\rho = Mn_M$, then (3b) and (A16) imply

$$n(z_2) = \overline{q}(z_1)n_M(z_2)$$

$$= \overline{n}(z_1)\exp\left(\frac{-\zeta}{\gamma H(z_1)}\right), \tag{A21}$$

where $\overline{n}(z)$ is the background number density profile of the tracer. Thus, like the total density ρ in (A16), the tracer number density n responds to adiabatic vertical displacements according to its adiabatic rarefaction curve (A21). As shown in Fig. 2b, this produces a perturbation of tracer number density

$$n'(z_2) = n(z_2) - \overline{n}(z_2), \tag{A22}$$

whose relative magnitude is given by

$$\frac{n'(z_2)}{\overline{n}(z_2)} = \frac{n(z_2)}{\overline{n}(z_2)} - 1$$

$$= \frac{\overline{n}(z_1)}{\overline{n}(z_2)}\exp\left(\frac{-\zeta}{\gamma H(z_1)}\right) - 1 \tag{A23a}$$

$$= \frac{\overline{q}(z_1)}{\overline{q}(z_2)}\exp\left(\frac{\zeta}{H_D(z_1)}\right) - 1 \tag{A23b}$$

$$= \frac{q'(z_2)}{\overline{q}(z_2)} + \frac{\rho'(z_2)}{\overline{\rho}(z_2)} + \left(\frac{q'(z_2)}{\overline{q}(z_2)}\right)\left(\frac{\rho'(z_2)}{\overline{\rho}(z_2)}\right), \tag{A23c}$$

where (A23c) is derived from (A23b) using (A18a) and (A20).

An equivalent derivation in terms of potential tracer number density is shown in Fig. 2c. Since ν in the parcel is conserved, then

$$\nu'(z_2) = \overline{\nu}(z_1) - \overline{\nu}(z_2), \tag{A24}$$

which, with the aid of (8), (11), and (A23a), yields

$$\frac{\nu'(z_2)}{\overline{\nu}(z_2)} = \frac{\overline{\nu}(z_1)}{\overline{\nu}(z_2)} - 1 \tag{A25a}$$

$$= \frac{\overline{n}(z_1)}{\overline{n}(z_2)}\exp\left(\frac{-\zeta}{\gamma H(z_1)}\right) - 1 \tag{A25b}$$

$$= \frac{n'(z_2)}{\overline{n}(z_2)}. \tag{A25c}$$

If ζ is small and $\overline{\nu}(z)$ variations are of much longer vertical scale than ζ, then (A25c) can be simplified using a TMS expansion of (A6b), along with (A7) and (A25a), to yield

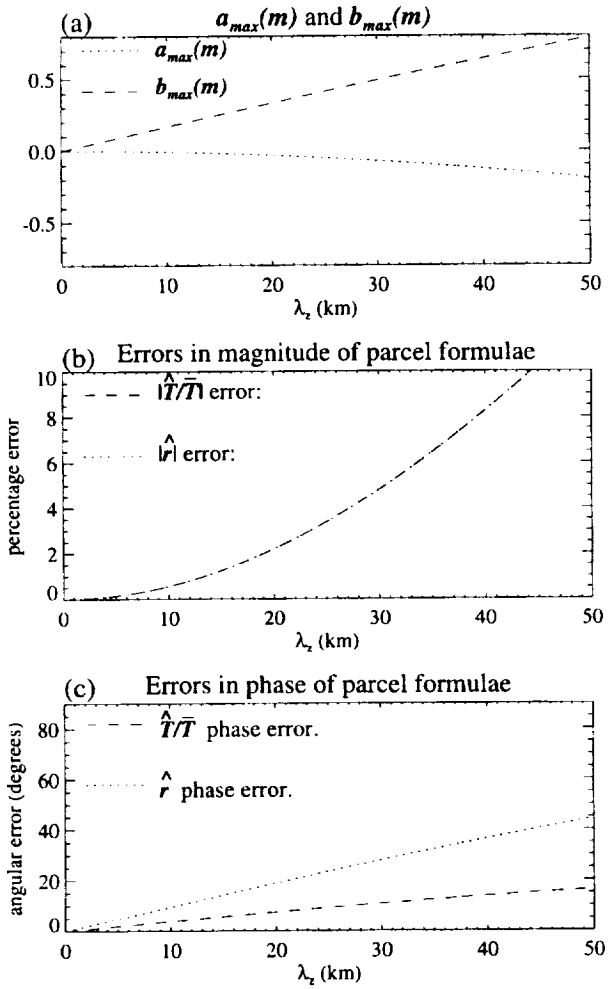

FIG. B1. Vertical wavelength variation of $a_{max}(m)$ and $b_{max}(m)$ (a), and deviations in magnitude (b) and phase (c) between the acoustic–gravity wave polarization relation (appendix B) and the corresponding parcel-based approximation (appendix A) relating $\hat{\zeta}$ to perturbations in relative temperature (dashed line) and relative density (dotted line).

$$\frac{\nu'(z_2)}{\overline{\nu}(z_2)} = \frac{n'(z_2)}{\overline{n}(z_2)} \approx \frac{\zeta}{H_\nu(z_1)}. \tag{A26}$$

The same expression also results from a direct TMS expansion of (A23a). Note the similar forms of (A26) and (A15b).

APPENDIX B

Acoustic–Gravity Wave Polarization Relations

On splitting atmospheric field variables into the sum of a mean and perturbation term ($X = \overline{X} + X'$), isolating and linearizing perturbation terms, and assuming wave solutions of the form

$$X' = \hat{X} \exp[\iota(kx + Mz - \Omega t)] \tag{B1}$$

$$= \hat{X} \exp[\iota(kx + mz - \Omega t) + z/2H_\rho], \tag{B2}$$

the following perturbation equations govern a zonally propagating nonhydrostatic gravity wave in a compressible rotating unsheared inviscid atmosphere (e.g., Gossard and Hooke 1975):

$$-\iota\omega\hat{u} - f\hat{v} = -\iota k\hat{\Phi}, \tag{B3}$$

$$-\iota\omega\hat{v} + f\hat{u} = 0, \tag{B4}$$

$$-\iota\omega\hat{w} + \hat{r}g = -(\iota M - H_\rho^{-1})\hat{\Phi}, \tag{B5}$$

$$-\iota\omega\hat{r} - \left(\frac{N^2}{g}\right)\hat{w} = -\left(\frac{\iota\omega}{c_s^2}\right)\hat{\Phi}, \tag{B6}$$

$$-\iota\omega\hat{r} + \iota k\hat{u} + (\iota M - H_\rho^{-1})\hat{w} = 0, \tag{B7}$$

where c_s is background sound speed, $(\hat{u}, \hat{v}, \hat{w})$ is the peak velocity amplitude, $\hat{r} = \hat{\rho}/\overline{\rho}$ is the relative density amplitude, and $\hat{\Phi} = \hat{p}/\overline{p}$, in which $\hat{p}$ is the pressure amplitude. The full nonhydrostatic dispersion relation for gravity waves [e.g., (23-7) of Gossard and Hooke (1975)] follows from the equation set (B3)–(B7); that is,

$$m^2 = k^2\left(\frac{N^2 - \omega^2}{\omega^2 - f^2}\right) - \frac{1}{4H_\rho^2} + \frac{\omega^2}{c_s^2}. \tag{B8}$$

Polarization relations follow from (B3)–(B7). Eliminating $\hat{\Phi}$ between (B5) and (B6) and noting that $\hat{w} = -\iota\omega\hat{\zeta}$, then

$$\hat{r} = \frac{\hat{\rho}}{\overline{\rho}} = \left(\frac{N^2}{g}\right)[1 + a(m, \omega) + \iota b(m, \omega)]\hat{\zeta}, \tag{B9}$$

$$a(m, \omega) = (1 - \omega^2/N^2)\left(\frac{g}{c_s^2}\right)\left[\frac{-\Gamma}{m^2 + \Gamma^2}\right], \tag{B10}$$

$$b(m, \omega) = (1 - \omega^2/N^2)\left(\frac{g}{c_s^2}\right)\left[\frac{m}{m^2 + \Gamma^2}\right], \tag{B11}$$

where $\Gamma = -1/(2H_\rho) + g/c_s^2$ is the anisothermal form of Eckart's coefficient. Since $c_s^2 = \gamma gH$, then eliminating $\hat{r}$ between (B5) and (B6) yields

$$\hat{\Phi} = N^2\gamma H[a(m, \omega) + \iota b(m, \omega)]\hat{\zeta}, \tag{B12}$$

where γ is the ratio of specific heats. This replicates (23-6) of Gossard and Hooke (1975) and can be reexpressed in terms of the relative pressure perturbation

$$\frac{\hat{p}}{\overline{p}} = \frac{\hat{\Phi}}{R\overline{T}} = \left(\frac{N^2}{g}\right)\gamma[a(m, \omega) + \iota b(m, \omega)]\hat{\zeta}. \tag{B13}$$

A linearized perturbation expansion of the ideal gas law yields

$$\frac{\hat{T}}{\overline{T}} = \frac{\hat{p}}{\overline{p}} - \frac{\hat{\rho}}{\overline{\rho}}, \tag{B14}$$

which, on inserting (B9) and (B13), yields

$$\frac{\hat{T}}{\overline{T}} = \left(\frac{-N^2}{g}\right)\{1 - (\gamma - 1)[a(m, \omega) + \iota b(m, \omega)]\}\hat{\zeta}. \tag{B15}$$

Equations (B3)–(B7) also yield the polarization relation

$$\hat{w} = \frac{-(\omega^2 - f^2)}{k(N^2 - \omega^2)}(m + \iota\Gamma)\hat{u}. \quad \text{(B16)}$$

For an isothermal ($H = H_\rho$) nonrotating ($f = 0$) atmosphere, it can be shown that the dispersion and polarization relations (B8)–(B16) are the same as Eqs. (21)–(24) and (26) of Hines (1960).

On linearizing the tracer continuity equation (1b), assuming a height-varying mean tracer profile $\overline{n}(z)$, and substituting the wave solution (B1), we obtain

$$-\iota\omega\hat{n} + \frac{\partial\overline{n}}{\partial z}\hat{w} + \overline{n}\nabla\cdot\hat{\mathbf{U}} = 0. \quad \text{(B17)}$$

From (B16), it follows that

$$\nabla\cdot\hat{\mathbf{U}} = \iota k\hat{u} + \iota M\hat{w}, \quad \text{(B18)}$$

$$= \left\{\frac{1}{\gamma H} - \frac{N^2}{g}[a(m, \omega) + \iota b(m, \omega)]\right\}\hat{w}, \quad \text{(B19)}$$

whereupon (B17) yields

$$\frac{\hat{n}}{\overline{n}} = -\left\{\frac{1}{\gamma H} + \frac{1}{\overline{n}}\frac{\partial\overline{n}}{\partial z} - \frac{N^2}{g}[a(m, \omega) + \iota b(m, \omega)]\right\}\hat{\zeta}. \quad \text{(B20)}$$

Thus, on comparing (B9), (B13), (B15), and (B19) with the simplified parcel-based derivations in appendix A (see also sections 2 and 3), we see that the normalized terms $|a(m, \omega)|$ and $|b(m, \omega)|$ must be $\ll 1$ for the two sets of equations to be equal to a good approximation. We note from (B10) and (B11) that the frequency dependence of $a(m, \omega)$ and $b(m, \omega)$ is weak, so for simplicity we consider the limiting maximum values

$$a_{\max}(m) = \frac{g}{c_s^2}\left(\frac{-\Gamma}{m^2 + \Gamma^2}\right), \quad \text{(B21)}$$

$$b_{\max}(m) = \frac{g}{c_s^2}\left(\frac{m}{m^2 + \Gamma^2}\right) \quad \text{(B22)}$$

that arise for $(\omega/N)^2 \to 0$.

Since these maximum values depend only on the vertical wavenumber m, Fig. B1a plots $a_{\max}(m)$ and $b_{\max}(m)$ versus $\lambda_z = 2\pi/|m|$ for an isothermal atmosphere of $\overline{T} = 230$ K. Figures B1b and B1c show the corresponding maximum difference in magnitude and phase between the polarization relations (B9) and (B15) and the corresponding parcel approximations $\hat{\rho}/\overline{\rho} = -\hat{T}/\overline{T} = (N^2/g)\hat{\zeta}$ given by (18). Other plots (not shown) revealed that these differences increase (decrease) with decreasing (increasing) $\overline{T}$, and that the equality in magnitude of the density and temperature departures in Fig. B1b occurs only when the atmosphere is isothermal. For vertical wavelengths $\lambda_z \lesssim 20$ km, we see from Fig. B1 that the approximate parcel-based formulas of appendix A, approximated by the wave polarization relations (14) and (18), produce only small deviations in amplitude and phase from the full acoustic–gravity wave polarizations relations (B9) and (B15).

APPENDIX C

Photochemical Reponse of Ozone Mixing Ratio in a Vertically Displaced Air Parcel

We start with the parcel-based ozone rate equation (Lindzen and Goody 1965)

$$\frac{dq_{O_3}}{dt} = 2J_{O_2}q_{O_2} - \frac{2\epsilon k_{O_3}J_{O_3}q_{O_3}^2}{k_{O_2}n_{O_2}}. \quad \text{(C1)}$$

where

$$\frac{\epsilon k_{O_3}}{k_{O_2}} \approx \epsilon(1.3 \times 10^{28}\ \text{m}^{-3})\left(\frac{T}{300\ \text{K}}\right)^{2.3} \times \exp[-(2060\ \text{K})/T] = G(T) \quad \text{(C2)}$$

(Demore et al. 1994). Equation (C1) differs from (2) and (31) only through insertion of an extra factor, ϵ, that scales the ozone destruction rate due to recombination with monatomic oxygen, k_{13}, to a net rate that resembles the one obtained when reactions with NO_x, HO_x, and ClO_x species are included (Zhu and Holton 1986).

We use (C1) and (C2) to describe the time evolution of ozone in a parcel displaced adiabatically by a small vertical distance ζ'. Since (A18a) holds for $n_{O_2}(z_2)/\overline{n}_{O_2}(z_2) - 1$, then

$$\frac{dq_{O_3}(z_2)}{dt} = 2J_{O_2}q_{O_2}(z_2) - \frac{2J_{O_3}}{\overline{n}_{O_2}(z_2)}G(T(z_2))q_{O_3}^2(z_2)\exp(-\zeta'/H_\rho), \quad \text{(C3)}$$

where $q_{O_3}(z_2) = \overline{q}_{O_3}(z_2) + q'_{O_3}(z_2)$ from (A19). We simplify (C3) by first noting that the background production/loss rate

$$\overline{R}_{O_3}(z_2) = 2J_{O_2}\overline{q}_{O_2}(z_2) - 2J_{O_3}\frac{G(\overline{T}(z_2))\overline{q}_{O_3}^2(z_2)}{\overline{n}_{O_2}} \approx 0. \quad \text{(C4)}$$

We then use a TMS expansion of $\exp(-\zeta'/H_\rho)$ and a truncated Taylor series expansion

$$G(\overline{T} + T') = G(\overline{T}) + T'\left(\frac{dG}{dT}\right)_{\overline{T}} = \overline{G} + G', \quad \text{(C5)}$$

where $T'(z_2) = T(z_2) - \overline{T}(z_2)$. Finally, on assuming constant q_{O_2} (no diffusive separation), constant J_x, and retaining only linear terms in the perturbation expansion of variables in (C3), we obtain, with the aid of (A13), (C4), and (C5),

$$\frac{dq_{O_3}(z_2)}{dt} = -\overline{B}(z_2)q'_{O_3}(z_2) - \overline{C}(z_2)T'(z_2), \quad \text{(C6)}$$

where

$$\overline{B}(z_2) = \frac{4J_{O_2}\overline{q}(z_2)G(\overline{T}(z_2))}{\overline{n}_{O_2}(z_2)}, \quad \text{(C7a)}$$

$$\overline{C}(z_2) = \frac{\overline{B}(z_2)\overline{q}(z_2)}{2\overline{T}^2(z_2)}\left[\overline{T}(z_2) - \left(\frac{d(\ln G)}{d(1/T)}\right)_{\overline{T}(z_2)}\right]. \quad \text{(C7b)}$$

Equation (C6) then yields the well-known ozone perturbation result of Lindzen and Goody (1965) (see section 3f), with the expressions (C7a) and (C7b) essentially the same as those derived by Zhu and Holton (1986).[1] More complete expressions for R_{O_3} with the NO_x, HO_x, and ClO_x rate terms included explicitly also leads to a linearized ozone deviation equation of the same form as (C6), although the formulas for the coefficients $\overline{B}$ and $\overline{C}$ are more complicated in this case (see, e.g., Stolarski and Douglass 1985).

REFERENCES

Alexander, M. J., and L. Pfister, 1995: Gravity wave momentum flux in the lower stratosphere over convection. *Geophys. Res. Lett.*, **22,** 2029–2032.

Bacmeister, J. T., S. D. Eckermann, L. Sparling, K. R. Chan, M. Loewenstein, and M. H. Proffitt, 1997: Analysis of intermittency in aircraft measurements of velocity, temperature and atmospheric tracers using wavelet transforms. *Gravity Wave Processes: Their Parameterization in Global Climate Models*, K. Hamilton, Ed., NATO ASI Series, Vol. I 50, Springer-Verlag, 85–102.

Bian, X., C. M. Berkowitz, and S. Zhong, 1996: Aircraft observations of the effects of internal gravity waves on ozone over the western North Atlantic. *J. Geophys. Res.*, **101,** 26 017–26 021.

Bird, J. C., S. R. Pal, A. I. Carswell, D. P. Donovan, G. L. Manney, J. M. Harris, and O. Uchino, 1997: Observations of ozone structures in the Arctic polar vortex. *J. Geophys. Res.*, **102,** 10 785–10 800.

Brasseur, G., and S. Solomon, 1984: *Aeronomy of the Middle Atmosphere*. 2d ed. Reidel, 452 pp.

Carslaw, K. S., M. Wirth, A. Tsias, B. B. Lou, A. Dörnbrack, M. Leutbecher, H. Volkert, M. Renger, J. T. Bacmeister, E. Reimer, and T. Peter, 1998: Increased stratospheric ozone depletion due to mountain-induced atmospheric waves. *Nature*, **391,** 675–678.

Chiu, Y. T., and B. K. Ching, 1978: The response of atmospheric and lower ionospheric layer structures to gravity waves. *Geophys. Res. Lett.*, **5,** 539–542.

Clemesha, B. R., V. W. J. H. Kirchoff, D. M. Simonich, H. Takahashi, and P. P. Batista, 1980: Spaced lidar and nightglow observations of an atmospheric sodium enhancement. *J. Geophys. Res.*, **85,** 3480–3489.

Collins, R. L., X. Tao, and C. S. Gardner, 1996: Gravity wave activity in the upper mesosphere over Urbana, Illinois: Lidar observations and analysis of gravity wave propagation models. *J. Atmos. Terr. Phys.*, **58,** 1905–1926.

Cox, R. M., J. M. C. Plane, and J. S. A. Green, 1993: A modelling investigation of sudden sodium layers. *Geophys. Res. Lett.*, **20,** 2841–2844.

Danielsen, E. F., R. S. Hipskind, W. L. Starr, J. F. Vedder, S. E. Gaines, D. Kley, and K. K. Kelly, 1991: Irreversible transport in the stratosphere by internal waves of short vertical wavelength. *J. Geophys Res.*, **96,** 17 433–17 452.

DeMore, W. B., S. P. Saunders, D. M. Golden, R. F. Hampson, M. J. Kurylo, C. J. Howard, A. R. Ravishankara, C. E. Kolb, and M. J. Molina, 1994: Chemical kinetics and photochemical data for use in stratospheric modeling. JPL Publ. 94-26, Jet Propulsion Laboratory, California Institute of Technology, Pasadena, CA, 273 pp. [Available from Jet Propulsion Laboratory, California Institute of Technology, Library Section, MS 111-120, 4800 Oak Grove Drive, Pasadena, CA 91109.]

Dudis, J. J., and C. A. Reber, 1976: Composition effects in thermospheric gravity waves. *Geophys. Res. Lett.*, **3,** 727–730.

Engelen, R. J., 1996: The effect of planetary waves on the total ozone zonal deviations in the presence of a persistent blocking anticyclone system. *J. Geophys. Res.*, **101,** 28 775–28 784.

Fritts, D. C., and P. K. Rastogi, 1985: Convective and dynamical instabilities due to gravity wave motions in the lower and middle atmosphere. *Radio Sci.*, **20,** 1247–1277.

——, J. R. Isler, G. E. Thomas, and Ø. Andreassen, 1993: Wave breaking signatures in noctilucent clouds. *Geophys. Res. Lett.*, **20,** 2039–2042.

——, ——, J. H. Hecht, R. L. Walterscheid, and Ø. Andreassen, 1997: Wave breaking signatures in sodium densities and OH nightglow, 2. Simulation of wave and instability structures. *J. Geophys. Res.*, **102,** 6669–6684.

Gardner, C. S., and J. D. Shelton, 1985: Density response of neutral atmospheric layers to gravity wave perturbations. *J. Geophys. Res.*, **90,** 1745–1754.

——, and D. G. Voelz, 1985: Lidar measurements of gravity wave saturation effects in the sodium layer. *Geophys. Res. Lett.*, **12,** 765–768.

Gibson-Wilde, D. E., R. A. Vincent, C. Souprayen, S. Godin, A. Hertzog, and S. D. Eckermann, 1997: Dual lidar observations of mesoscale fluctuations of ozone and horizontal winds. *Geophys. Res. Lett.*, **24,** 1627–1630.

Gossard, E. E., and W. H. Hooke, 1975: *Waves in the Atmosphere*. Elsevier, 456 pp.

Hansen, G., and U.-P. Hoppe, 1997: Lidar observations of polar stratospheric clouds and stratospheric temperature in winter 1995/96 over northern Norway. *Geophys. Res. Lett.*, **24,** 131–134.

Hedin, A. E., and H. G. Mayr, 1987: Characteristics of wavelike fluctuations in Dynamics Explorer neutral composition data. *J. Geophys. Res.*, **92,** 11 159–11 172.

Hess, P., 1990: Variance in trace constituents following the final stratospheric warming. *J. Geophys. Res.*, **95,** 13 765–13 779.

Hickey, M. P., and J. M. C. Plane, 1995: A chemical-dynamical model of wave-driven sodium fluctuations. *Geophys. Res. Lett.*, **22,** 2861–2864.

Hines, C. O., 1960: Internal gravity waves at ionospheric heights. *Can. J. Phys.*, **38,** 1441–1481; Corrigendum, **42,** 1425–1427.

Hoegy, W. R., L. H. Brace, W. T. Kasprzak, and C. T. Russell, 1990: Small-scale plasma, magnetic and neutral density fluctuations in the nightside Venus ionosphere. *J. Geophys. Res.*, **95,** 4085–4102.

Iribarne, J. V., and W. L. Godson, 1981: *Atmospheric Thermodynamics*. 2d ed. D. Reidel, 259 pp.

Jensen, E. J., and G. E. Thomas, 1994: Numerical simulations of the effects of gravity waves on noctilucent clouds. *J. Geophys. Res.*, **99,** 3421–3430.

Kao, C.-Y. J., S. Barr, A. Quintanar, D. Langley, G. A. Glatzmaier, and R. C. Malone, 1995: Numerical modeling of tracer transport within and out of the lower tropospheric Arctic region. *Geophys. Res. Lett.*, **22,** 941–944.

Kwon, K. H., D. C. Senft, and C. S. Gardner, 1988: Lidar observations of sporadic sodium layers at Mauna Kea Observatory, Hawaii. *J. Geophys Res.*, **93,** 14 199–14 208.

Lamb, K. G., and J. A. Shore, 1992: The influence of horizontal inhomogeneities on the propagation of high frequency linear

[1] Note that their Eq. 22 is wrong [cf. with (18)], which leads to a small error in their expression for $\overline{C}$.

internal gravity waves across a baroclinic flow. *J. Phys. Oceanogr.*, **22,** 965–975.

Langford, A. O., M. H. Proffitt, T. E. VanZandt, and J.-F. Lamarque, 1996: Modulation of tropospheric ozone by a propagating gravity wave. *J. Geophys. Res.*, **101,** 26 605–26 613.

Limpasuvan, V., and C. B. Leovy, 1995: Observation of the two day wave near the southern summer stratopause. *Geophys. Res. Lett.*, **22,** 2385–2388.

Lindzen, R. S., 1981: Turbulence and stress owing to gravity wave and tidal breakdown. *J. Geophys. Res.*, **86,** 9707–9714.

——, and R. Goody, 1965: Radiative and photochemical processes in mesospheric dynamics. Part I: Models for radiative and photochemical processes. *J. Atmos. Sci.*, **22,** 341–348.

Lutman, E. R., J. A. Pyle, M. P. Chipperfield, D. J. Lary, J. Kilbane-Dawe, J. W. Waters, and N. Larsen, 1997: Three-dimensional studies of the 1991/1992 Northern Hemisphere winter using domain-filling trajectories with chemistry. *J. Geophys. Res.*, **102,** 1479–1488.

Nagasawa, C., and M. Abo, 1995: Lidar observations of a lot of sporadic sodium layers in mid-latitude. *Geophys. Res. Lett.*, **22,** 263–266.

Newell, R. E., Z.-X. Wu, Y. Zhu, W. Hu, E. V. Browell, G. L. Gregory, G. W. Sachse, J. E. Collins Jr., K. K. Kelly, and S. C. Liu, 1996: Vertical fine-scale atmospheric structure measured from NASA DC-8 during PEM-West A. *J. Geophys. Res.*, **101,** 1943–1960.

Newman, P. A., and W. J. Randel, 1988: Coherent ozone-dynamical changes during southern hemisphere spring. *J. Geophys. Res.*, **93,** 12 585–12 606.

——, and M. R. Schoeberl, 1995: A reinterpretation of the data from the NASA Stratosphere-Troposphere Exchange Project. *Geophys. Res. Lett.*, **22,** 2501–2504.

Orsolini, Y. J., G. Hansen, U.-P. Hoppe, G. L. Manney, and K. H. Fricke, 1997: Dynamical modelling of wintertime lidar observations in the Arctic: Ozone laminae, and ozone depletion. *Quart. J. Roy. Meteor. Soc.*, **123,** 785–800.

Pierce, R. B., T. D. Fairlie, W. L. Grose, R. Swinbank, and A. O'Neill, 1994: Mixing processes in the polar night jet. *J. Atmos. Sci.*, **51,** 2957–2972.

Prata, A. J., 1990: Travelling waves in Nimbus-7 SBUV ozone measurements: Observations and theory. *Quart. J. Roy. Meteor. Soc.*, **116,** 1091–1122.

Randel, W. J., 1990: Kelvin wave-induced trace constituent oscillations in the equatorial stratosphere. *J. Geophys. Res.*, **95,** 18 641–18 652.

——, 1993: Global normal mode Rossby waves observed in stratospheric ozone data. *J. Atmos. Sci.*, **50,** 406–420.

——, and J. C. Gille, 1991: Kelvin wave variability in the upper stratosphere observed in SBUV data. *J. Atmos. Sci.*, **48,** 2336–2349.

Reber, C. A., A. E. Hedin, D. T. Pelz, W. E. Potter, and L. H. Brace, 1975: Phase and amplitude relationships of wave structure observed in the lower thermosphere. *J. Geophys. Res.*, **80,** 4576–4580.

Reid, S. J., and G. Vaughan, 1991: Lamination in ozone profiles in the lower stratosphere. *Quart. J. Roy. Meteor. Soc.*, **117,** 825–844.

Rind, D., and J. Lerner, 1996: Use of on-line tracers as a diagnostic tool in general circulation model development, 1, Horizontal and vertical transport in the troposphere. *J. Geophys. Res.*, **101,** 12 667–12 683.

Roble, R. G., and G. G. Shepherd, 1997: An analysis of wind-imaging interferometer observations of $O(^1S)$ equatorial emission rates using the thermosphere-ionosphere-mesosphere-electrodynamics general circulation model. *J. Geophys. Res.*, **102,** 2467–2474.

Rüster, R., P. Czechowsky, P. Hoffman, and W. Singer, 1996: Gravity wave signatures at mesopause heights. *Ann. Geophys.*, **14,** 1186–1191.

Salby, M. L., P. Callaghan, S. Solomon, and R. R. Garcia, 1990: Chemical fluctuations associated with vertically propagating equatorial Kelvin waves. *J. Geophys. Res.*, **95,** 20 491–20 505.

Senft, D. C., and C. S. Gardner, 1991: Seasonal variability of gravity wave activity and spectra in the mesopause region at Urbana. *J. Geophys. Res.*, **96,** 17 229–17 264.

Shibata, T., T. Itabe, K. Mizutani, and K. Asai, 1994: Pinatubo volcanic aerosols observed by lidar over Wakkanai, Japan. *Geophys. Res. Lett.*, **21,** 197–200.

Stanford, J. L., and J. R. Ziemke, 1993: Rossby-gravity waves in tropical total ozone. *Geophys. Res. Lett.*, **20,** 2239–2242.

Stolarski, R. S., and A. R. Douglass, 1985: Parameterization of the photochemistry of stratospheric ozone including catalytic loss processes. *J. Geophys. Res.*, **90,** 10 709–10 718.

Sugiyama, T., 1988: Response of electrons to a gravity wave in the upper mesosphere. *J. Geophys. Res.*, **93,** 11 083–11 091.

Teitelbaum, H., M. Moustaoui, J. Ovarlez, and H. Kelder, 1996: The role of atmospheric waves in the laminated structure of ozone profiles at high latitudes. *Tellus*, **48A,** 422–455.

Turner, J. S., 1973: *Buoyancy Effects in Fluids*. Cambridge University Press, 367 pp.

Wallace, J. M., and P. V. Hobbs, 1977: *Atmospheric Science: An Introductory Survey*. Academic Press, 467 pp.

Waugh, D. W., R. A. Plumb, R. J. Atkinson, M. R. Schoeberl, L. R. Lait, P. A. Newman, M. Loewenstein, D. W. Toohey, L. M. Avallone, C. R. Webster, and R. D. May, 1994: Transport out of the lower stratospheric Arctic vortex by Rossby wave breaking. *J. Geophys. Res.*, **99,** 1071–1088.

Weinstock, J., 1978: Theory of the interaction of gravity waves with O_2 $(^1\Sigma)$ airglow. *J. Geophys. Res.*, **83,** 5175–5185.

Wilson, J. C., W. T. Lai, and S. D. Smith, 1991: Measurements of condensation nuclei above the jet stream: Evidence for cross jet transport by waves and new particle formation at high altitudes. *J. Geophys. Res.*, **96,** 17 415–17 423.

Wirth, V., 1993: Quasi-stationary planetary waves in total ozone and their correlations with lower stratospheric temperature. *J. Geophys. Res.*, **98,** 8873–8882.

Zhu, X., and J. R. Holton, 1986: Photochemical damping of inertio–gravity waves. *J. Atmos. Sci.*, **43,** 2578–2584.

Ziemke, J. R., and J. L. Stanford, 1994: Quasi-biennial oscillation and tropical waves in total ozone. *J. Geophys. Res.*, **99,** 23 041–23 056.

Appendix B

Mesoscale temperature fluctuations induced by a spectrum of gravity waves: A comparison of parameterizations and their impact on stratospheric microphysics

Bacmeister, J. T., S. D. Eckermann, A. Tsias, K. S. Carslaw, and T. Peter, *J. Atmos. Sci.*, (in press), 1998.

=20pc =41pc
=20pc =41pc

Mesoscale Temperature Fluctuations Induced by a Spectrum of Gravity Waves: A Comparison of Parameterizations and Their Impact on Stratospheric Microphysics

Julio T. Bacmeister
Universities Space Research Association, 10227 Wincopin Circle, Suite #202, Columbia, MD, 21044

Stephen D. Eckermann
Computational Physics, Inc., Fairfax, VA, 22031

Athanasios Tsias, Kenneth S. Carslaw, and Thomas Peter
Max Planck Institute for Chemistry, 55020 Mainz, Germany

Abstract. Power spectral densities (PSDs) of mesoscale fluctuations of temperature and rate of change of temperature (heating/cooling rate) due to a spectrum of stratospheric gravity waves are derived using canonical spectral forms based on observations and linear gravity wave theory. The parameterization developed here assumes a continuous distribution of horizontal wave phase speeds, as opposed to a previous spectral parameterization in which all waves were assigned stationary ground-based phase speeds. Significantly different heating/cooling rate PSDs result in each case. The differences are largest at small horizontal scales, where the continuous phase-speed parameterization yields heating/cooling rate PSDs that are several orders of magnitude smaller than in the stationary phase-speed parameterization. A simple Monte Carlo method is used to synthesize randomly-phased temperature perturbation time series within tagged air parcels using either spectral parameterization. These time series are incorporated into a nonequilibrium, microphysical trajectory-box model to assess the microphysical consequences of each parameterization. Collated results yield a "natural" geophysical scatter of instantaneous aerosol volumes within air parcels away from equilibrium conditions. The amount of scatter was much smaller when the continuous phase-speed parameterization was used.

1. Introduction

The importance of polar stratospheric clouds (PSCs) in ozone depletion has prompted considerable research into their composition and formation. Observations show that PSCs often form preferentially over mountainous terrain, where they seem to be associated with the penetration of mountain lee waves into the stratosphere (e.g. Cariolle *et al.* 1989; Deshler *et al.* 1994; Godin *et al.* 1994; Fromm *et al.* 1997; Carslaw *et al.* 1998a,b). Recent modeling work has shown that mountain wave temperature perturbations affect the formation and growth of aerosol particles, as well as subsequent heterogeneous chemical reactions which take place on the particles (e.g., Peter *et al.* 1994; Meilinger *et al.* 1995; Bormann *et al.* 1997; Tsias *et al.* 1997). This occurs because microphysical processes have a strongly nonlinear dependence on both temperature (e.g., Tabazadeh *et al.* 1994; Carslaw *et al.* 1994) and the rate of change of temperature (e.g., Meilinger *et al.* 1995; Tsias *et al.* 1997). Thus, details in air parcel temperature histories can have an important impact on microphysical end products, such as particle size distributions, total aerosol volume and particle freezing (Drdla and Turco 1991; Jensen and Toon, 1994; Koop *et al.* 1995, 1997; Tsias *et al.* 1997). Furthermore, several important heterogeneous reaction rates have a strong temperature dependence (e.g., Bormann *et al.* 1997), which leads to rates of chlorine activation in stratospheric mountain waves that are orders of magnitude faster than those encountered synoptically (Carslaw *et al.* 1998a). Carslaw *et al.* (1998b) have proposed that the combined effect of all such mountain waves in the Arctic could cause an overall decrease in ozone levels. The temperature oscillations of a gravity wave have also been shown to be important in microphysical models of polar mesospheric clouds (Turco *et al.* 1982; Jensen and Thomas 1994) and of high cirrus clouds (Potter and Holton 1995; Jensen *et al.* 1996; Lin *et al.* 1998).

All of these model studies considered the microphysical effects of single waves, whereas observations reveal that, on average, broad pseudo-random spectra of temperature fluctuations exist in the stratosphere (e.g., Nastrom and Gage 1985; Tsuda *et al.* 1991; Bacmeister *et al.* 1996; Whiteway *et al.* 1997). Tabazadeh *et al.* (1996) parameterized this by assuming Gaussian probability density functions (PDFs) of mesoscale temperature fluctuations due to a spectrum of waves, basing their variances on stratospheric data taken from the Microwave Temperature Profiler (MTP) on NASA's ER-2 research aircraft. Murphy and Gary (1995) (hereafter MG95) also addressed this issue by deriving mesoscale horizontal wavenumber spectra of temperature, heating/cooling rate (i.e., rate of change of temperature) and PSC supersaturation fluctuations, based on the temperature spectra observed from MTP and other in-situ aircraft measurements in the lower stratosphere.

The calculations of MG95 were based on the implicit assumption that mesoscale temperature fluctuations observed by the aircraft were stationary with respect to the ground, implying a spectrum of gravity waves with stationary ground-based horizontal phase speeds (such as mountain waves). However, analysis of accumulated Meteorological Measurement System (MMS) data from stratospheric ER-2 flights led Bacmeister *et al.* (1996) (hereafter B96) to different conclusions. They compared fluctuations in these data with idealized models of the two-dimensional (2D) spectrum of gravity-wave-induced horizontal velocities as a function of vertical wavenumber m, and intrinsic frequency ω, $G_{u,v}(m,\omega)$. This continuous 2D spectrum implies a broad, continuous distribution of wave phase speeds, in contrast to the MG95 model. B96 used linear gravity wave theory to transform $G_{u,v}(m,\omega)$ into corresponding spectral predictions for the one-dimensional horizontal wavenumber (k) spectra of horizontal velocities, $F_{u,v}(k)$, and vertical velocities, $F_w(k)$ (Gardner *et al.* 1993a,b). Excellent agreement was found between these theoretical spectra and corresponding spectra derived from MMS data, leading them to conclude that mesoscale temperature and velocity fluctuations in stratospheric ER-2 data were consistent with a spectrum of gravity waves with a broad distribution of horizontal phase speeds.

In this paper, we go on to develop a spectral parameterization of mesoscale temperature and heating/cooling rate perturbations based on the continuous phase speed model of Gardner *et al.* (1993a,b) and B96, and compare it with the stationary phase speed parameterization of MG95. We demonstrate that, in each case, very different temperature and heating/cooling rate perturbations arise within air parcels as they are advected through the wave fields. Reanalysis of MMS data reveals that PDFs of mesoscale temperature amplitudes in the stratosphere are approximately Gaussian, with depatures only in the "wings"

of the distribution. We associate the Gaussian components of the PDFs with the basic background spectrum of wave activity that is always present in the stratosphere, and the nonGaussian tails with intermittent large-amplitude wave events. We go on to generate synthetic time series of parcel-based temperature perturbations using a simple Monte Carlo method, which yields Gaussian temperature PDFs that can be governed by either the MG95 or B96-based spectral parameterizations. Finally, we use these artificial time series within a microphysical box-trajectory model for the stratosphere to assess the microphysical impacts of each parameterization.

2. Spectral Parameterization

In their analysis of velocity and temperature fluctuation spectra from MMS data from the lower stratosphere, B96 used linear polarization and dispersion relations for hydrostatic, nonrotating gravity waves to transform models for the 2D gravity-wave spectrum, $G_{u,v}(m,\omega)$, into corresponding predictions for the one dimensional horizontal wavenumber spectra of horizontal velocities, $F_{u,v}(k)$, and vertical velocities, $F_w(k)$, that are measured by the aircraft (Gardner *et al.* 1993a,b). A further assumption of horizontal isotropy in wave propagation directions was made in these theoretical derivations. B96 found excellent agreement between the velocity spectra observed by MMS and theoretical predictions for $F_{u,v}(k)$ and $F_w(k)$ based on a separable analytical hydrostatic gravity-wave spectral model of the form

$$G_{u,v}(m,\omega) = E_0 \hat{A}_{u,v}(m)\hat{B}_{u,v}(\omega), \tag{1}$$

where $\hat{A}_{u,v}(m)$ and $\hat{B}_{u,v}(\omega)$ are normalized 1D model spectra and E_0 is the total wave energy per unit mass (Fritts and VanZandt 1993). The shapes of the 1D model spectra are discussed in depth by Gardner *et al.* (1993a,b), Fritts and VanZandt (1993) and B96. Briefly, the vertical wavenumber spectrum $\hat{A}_{u,v}(m) \rightarrow m^{-3}$ at large m and peaks at a characteristic wavenumber m_*, which is around 2π (2–3 km)$^{-1}$ in the lower stratosphere. The normalized frequency spectrum takes the form $\hat{B}_{u,v}(\omega) \propto [1+(f/\omega)^2]\omega^{-p}$ between the allowed intrinsic frequencies $\mid f \mid < \mid \omega \mid < N$ ($\hat{B}_{u,v}(\omega) = 0$ elsewhere), where f is the Coriolis parameter, N is the background Brunt-Väisälä frequency, and $p = 2$. These shapes are based on both theory and accumulated data, and although nonseparable models for $G_{u,v}(m,\omega)$ have also been proposed (e.g., Gardner 1996; Dewan 1997), the separable form (1) is still used commonly in the stratosphere (e.g., Gardner *et al.* 1993a,b; Fritts and VanZandt, 1993). The model (1) implies a broad continuous distribution of wave phase speeds within the spectrum, as opposed to the stationary phase speed model of MG95.

We now apply the model (1) to predict PSDs of temperature and heating/cooling rate perturbations.

2.1. Temperature PSDs

B96 also evaluated PSDs of MMS potential temperature data and compared them to the predictions of the model (1). Simple polarization relations for hydrostatic gravity waves lead to the relation

$$G_T(m,\omega) = \left(\frac{\bar{T}}{\bar{\Theta}}\right)^2 G_\Theta(m,\omega) = Q(\omega)\left(\frac{N\overline{T}}{g}\right)^2 G_{u,v}(m,\omega), \tag{2}$$

where $G_T(m,\omega)$ is the 2D gravity-wave temperature spectrum, $G_\Theta(m,\omega)$ is the potential temperature spectrum, g is gravitational acceleration, $\bar{\Theta}$ and $\bar{T}$ are background potential and absolute temperatures, respectively, and $Q(\omega)$ is the ratio of potential to kinetic energy of a given wave of intrinsic frequency ω. For hydrostatic waves, $Q(\omega) = 1$ for nonrotating flow and $Q(\omega)=\frac{(\omega^2-f^2)}{(\omega^2+f^2)}$ for rotating flow (for the calculations in this paper, we have assumed a nonrotating atmosphere). This leads to model horizontal wavenumber PSDs

$$F_T(k) = T_0^2 \hat{F}_T(k) \propto F_\Theta(k) \propto \left(\frac{N\overline{T}}{g}\right)^2 F_{u,v}(k), \tag{3}$$

where T_0^2 is the total temperature variance and $\hat{F}_T(k)$ is normalized model spectrum. Thus, the potential temperature, absolute temperature and horizontal velocity fluctuations should all have similarly-shaped horizontal wavenumber spectra. B96 showed that $F_\Theta(k)$ and $F_{u,v}(k)$ computed from MMS data had similar shapes, and thus agreed well with the model prediction (3) based on (1).

Of additional relevance to microphysics is the intrinsic frequency PSD of temperatures, which governs the time variations of temperature fluctuations within tagged air parcels as they are advected by the background flow. This spectrum is difficult to measure directly. However, it is easily derived from the model spectra (1) and (2), to yield

$$B_T(\omega) = T_0^2 \hat{B}_T(\omega) = Q(\omega) \left(\frac{N\overline{T}}{g}\right)^2 E_0 \hat{B}_{u,v}(\omega) \equiv B_T^{B96}(\omega), \tag{4}$$

where $\hat{B}_T(\omega)$ is the normalized temperature spectrum.

The present analysis can be contrasted to that of MG95, which assumed (implicitly) that all the waves in the spectrum were stationary with respect to the ground. MG95 used a model for the horizontal wavenumber temperature PSD based on data from various airborne platforms, which exhibited similar spectral shapes to the model spectrum $F_T(k)$ in (3). Under their stationary phase-speed assumption, a Taylor transformation from the ground-based to the intrinsic frame[1] yields the intrinsic (parcel-based) frequency PSD

$$B_T^{MG95}(\omega, \mathcal{U}) = T_0^2 \frac{\hat{F}_T(\omega/\mathcal{U})}{\mathcal{U}}, \tag{5}$$

where $\mathcal{U} = (\bar{U}^2 + \bar{V}^2)^{1/2}$ is the background wind speed and $\omega = k\mathcal{U}$. This derivation also assumes no directional variability in $\hat{F}_T(k)$ (i.e. azimuthal isotropy). Note the strong dependence of this parcel-based spectrum on the background wind speed.

2.2. Heating/Cooling Rate PSDs

If the wave spectrum is nondissipating, as is often the case in the lower stratosphere [see, e.g., Figures 7 and 8 of Tsuda *et al.* (1991)], an air parcel will be displaced adiabatically about its equilibrium position by the wave field. Thus, the potential temperature of the parcel will be conserved, which, for a single wave, yields the linearized perturbation equation

$$D_t\theta' = \partial_t\theta' + \overline{U}\partial_x\theta' + \overline{V}\partial_y\theta' = -w'\partial_z\overline{\Theta}, \tag{6}$$

where θ' and w' are wave-induced perturbations of potential temperature and vertical velocity, respectively, $\overline{U}$ and $\overline{V}$ are the background zonal and meridional winds, respectively, $\overline{\Theta}$ is the background potential temperature, subscripted ∂ terms denote local partial derivatives (i.e. $\partial_t = \partial/\partial t$), and D_t is the intrinsic (parcel-based) time derivative. Horizontal gradients in background quantities were neglected in deriving (6).

Hydrostatic gravity waves have shallow vertical structure, and so the temperature and potential temperature perturbations are approximately related, as in (2), according to

$$\frac{\theta'}{\overline{\Theta}} = \frac{T'}{\overline{T}} \tag{7}$$

---

[1] the Taylor transformation converts stationary horizontal wavelength structures in one frame (in this case, the ground-based frame) into temporal variations measured within another frame which is being advected through this horizontal variability (in this case, the intrinsic frame). Note that this is the inverse Taylor transformation to the one used to derive ground-based frequency spectra due to stratified two-dimensional turbulence models, in which the horizontal variability is assumed to be stationary ("frozen") in the intrinsic frame [see, e.g., eq. (9) of Vincent and Eckermann (1990)].

(e.g., Eckermann *et al.* 1998). Thus, rearranging terms in (6) and scaling with (7), we obtain the expression

$$D_t T' = \partial_t T' + \overline{U}\partial_x T' + \overline{V}\partial_y T' = -w'\partial_z \overline{\Theta}\left(\frac{\overline{T}}{\overline{\Theta}}\right) = -\left(\frac{\overline{T}N^2}{g}\right)w', \tag{8}$$

for the Lagrangian rate of change of temperature perturbation (i.e., the heating/cooling rate perturbation within an air parcel advected by the mean wind). Thus, for linear adiabatic gravity waves, the heating/cooling rate perturbations are proportional to the vertical velocity perturbations, and so the heating/cooling rate PSD, $F_{D_tT}(k)$, follows from simple scaling of the PSD of vertical velocity according to (8):

$$F_{D_tT}(k) = \left(\frac{\overline{T}N^2}{g}\right)^2 F_w(k) \equiv F_{D_tT}^{B96}(k). \tag{9}$$

The horizontal wavenumber PSD of heating/cooling rate fluctuations under the continuous phase speed model, (9), may be contrasted with the one arising from the MG95 stationary phase speed model, which is given by

$$F_{D_tT}^{MG95}(k,U) = U^2 k^2 F_T(k). \tag{10}$$

This relation follows *via* a Taylor transformation from the ground-based frame (where ∂_t terms vanish since waves are taken to be stationary) to the intrinsic frame to derive the parcel-based time derivative D_t (Murphy and Gary 1995). Note that, unlike (9), the MG95 heating/cooling rate PSD (10) is a strong function of the background wind speed U.

Intrinsic frequency PSDs of heating/cooling rate follow from the corresponding temperature PSDs. For the B96-based model,

$$B_{D_tT}^{B96}(\omega) = \omega^2 B_T^{B96}(\omega), \tag{11}$$

and so is approximately flat given the approximately ω^{-2} shape of $B_T^{B96}(\omega)$ implied by (4). The corresponding PSD from the MG95 model is

$$B_{D_tT}^{MG95}(\omega,U) = \omega^2 B_T^{MG95}(\omega,U) = \frac{\omega^2}{U} F_T(\omega/U), \tag{12}$$

where $\omega = kU$.

3. Comparisons with Data

To compare the various parameterizations with data, we use vertical velocity and temperature fluctuations derived from MMS data during 3 aircraft campaigns employing NASA's ER-2 aircraft: (1) the second Arctic Airborne Stratospheric Expedition (AASEII); (2) the Stratospheric Photochemistry Aerosol and Dynamics Experiment (SPADE); and (3) the Airborne Southern Hemisphere Ozone Experiment/Measurements for Assessing the Effects of Stratospheric Aircraft (ASHOE/MAESA) campaign. Locations and dates of these campaigns, as well as a brief description of the MMS data set, can be found in B96 and references therein. The PSDs used in this study are calculated from discreet wavelet transforms (DWTs) in the manner outlined in B96.

3.1. Heating/Cooling Rates PSDs

It was noted in section 2 that the two parameterizations use a similar observationally-constrained model for the horizontal wavenumber spectrum of temperatures, $F_T(k)$, but derive different heating/cooling rate PSDs from it. These differences are ilustrated in Figure 1. The solid curve with triangular symbols in Figure 1a shows $F_{D_tT}^{B96}(k)$ derived from MMS vertical velocity spectra using (9). It represents a log-average over all flights in the AASE II, SPADE, and ASHOE/MAESA campaigns. The remaining curves in Figure 1a show $F_{D_tT}^{MG95}(k,U)$ for three U values of 1 m s^{-1}, 20 m s^{-1} and 50 m s^{-1}, as obtained by

scaling a corresponding log-averaged PSD of MMS temperature (shown in Figure 1b) using (10).

The shapes of the two heating/cooling rate PSDs are clearly very different. The MG95 PSDs are much flatter at small scales. At scales smaller than 6.4 km, $F_{D_tT}^{MG95}(k,U)$ decays weakly with a spectral index between 0 and −1, while $F_{D_tT}^{B96}(k)$ decays more rapidly with a spectral index close to −3. The magnitude of $F_{D_tT}^{MG95}(k,U)$ also depends sensitively on the background flow speed U, since it determines how rapidly the parcels are advected through, and perturbed by, the stationary horizontal wave structures. In contrast, the heating/cooling rate PSD determined from the B96-based parameterization (9) has no explicit dependence on background flow conditions. Observationally, B96 found a weak dependence of the MMS vertical velocity PSD on the magnitude of the background horizontal wind, and other studies have also reported some sensitivities of stratospheric velocity spectra to the background wind profile (e.g., Eckermann 1995). The sensitivity of the MMS vertical velocity PSDs to background wind speed appeared to vary with horizontal scale: at $k>m_*$ the vertical velocity PSDs appeared to be less sensitive to changes in the background wind speed than the PSDs at $k<m_*$ (Bacmeister *et al.* 1996). So, while some evidence for a dependence on wind speed exists, existing data indicate that it is significantly weaker than the quadratic dependence of $F_{D_tT}^{MG95}(k,U)$ on U in (10) and Figure 1a.

Table 1 gives spectrally-integrated root-mean-square (rms) heating/cooling rates for the B96-based heating/cooling rate spectrum within several logarithmically-spaced wavenumber ranges, as determined by numerically integrating $F_{D_tT}^{B96}(k)$ in Figure 1a. Integrated heating/cooling rates based on (9) peak at scales between ∼3–25 km. This is in contrast to the MG95 spectral model, which yields integrated cooling rates that increase monotonically as horizontal scales decrease (see Table 1 of MG95).

3.2. Temperature PDFs

Another approach to parameterizing multi-wave temperature perturbations within microphysical models is to employ Gaussian PDFs (Tabazadeh *et al.* 1996). The DWT analysis of MMS data by B96 preserves information about the location and amplitude of fluctuations at each of the characteristic scales (or "octaves") resolved by the DWT, which allows us to study temperature fluctuation statistics and PDF's as a function of horizontal scale.

Figure 2 shows PDFs of DWT temperature amplitudes at different horizontal scales. Least-squares fits to a Gaussian distribution over the central 68% of the data are also shown. Within $\pm 1\sigma$ of the peak, the PDFs closely approximate a Gaussian distribution, as assumed by Tabazadeh *et al.* (1996). The rms amplitudes of the fluctuations in Figure 2 are comparable to those obtained by MG95 at similar horizontal scales.

However, there is evidence of non-Gaussian high-amplitude tails in all of the PDFs in Figure 2. In other words, high-amplitude temperature fluctuations are somewhat more probable than would be inferred from the Gaussian distributions determined from fits to the central 68% of the data. These departures from Gaussianity become more pronounced as the horizontal scale of the fluctuations decreases in Figure 2. Chi-squared tests of the observed PDFs *versus* the Gaussian fits indicate that the non-Gaussian behavior in the wings of the distributions is highly significant statistically. Similar behavior is observed in the PDFs of horizontal velocity fluctuations measured by MMS in the stratosphere (Bacmeister *et al.* 1997a). The origin of the non-Gaussian tails in the temperature fluctuations is not entirely clear. However, intermittent large-amplitude wave events are likely to be at least partially responsible (Bacmeister *et al.* 1990; Alexander and Pfister 1995).

4. Parameterizations for Parcel-based Calculations

The spectral parameterizations (3), (9), (10) and those of MG95 are presented as horizontal wavenumber spectra, which govern the horizontal "line" distribution of a collection of parcels at a given instant in time. However, many microphysical models are Lagrangian, concentrating instead on time variations of meteorological and microphysical parameters within tagged air parcels as they are advected by the background flow.

For such models, spectral parameterizations of wave-induced temperature fluctuations following an air parcel are needed. These are given by the intrinsic frequency spectra (4)

and (5) for the B96-based and MG95 parameterizations, respectively. Again, the two parameterization give very different results. For temperatures, quasi-invariant spectra $\sim\omega^{-2}$ arise in the B96-based model (4), whereas the MG95-based spectrum (5) follows the shape of the horizontal wavenumber spectrum according to $F_T(\omega/U)$, and its intensity scales with background wind speed U. Analogous differences exist between the heating/cooling rate spectra (11) and (12).

To assess the effects of each parameterization on Lagrangian microphysical models, it is first necessary to generate parcel-based temperature perturbation time series governed by these spectral models. A straightforward approach for the B96-based parameterization is to generate a random time series of the form

$$T'_{B96}(t) = \sqrt{2}T_0 \sum_{i=1}^{n} \left(\hat{B}_T^{B96}(\omega_i)\Delta\omega \right)^{1/2} \sin(\omega_i t + \phi_i), \tag{13}$$

where $\sqrt{2}$ transforms from rms to peak amplitudes, $\Delta\omega$ is a (constant) frequency step, ω_i is the ith. (evenly-spaced) frequency and ϕ_i is a random phase for this harmonic. The frequency step $\Delta\omega$ must be small enough to resolve shape transitions in $B_T^{B96}(\omega)$ adequately, and n and $\Delta\omega$ are chosen so as to integrate $\hat{B}_T^{B96}(\omega_i)$ over its full range between f and N (i.e., $\omega_1 = f + \Delta\omega/2$, $\omega_n = N - \Delta\omega/2$). While this is similar to the Monte Carlo method of Eckermann (1990), many other randomly-phased Fourier and/or wavelet synthesis methods could also be used (e.g., Owens 1978; Benzi *et al.* 1993; Alexander 1996; Elliott *et al.* 1997). Note that (13) yields Gaussian temperature PDFs, and so is also consistent with the PDF-based modeling strategy of Tabazadeh *et al.* (1996).

The main remaining task is to choose a representative total rms temperature amplitude T_0 for insertion into (13). Here, we attempt a data-based estimate of it from our temperature PSD in Figure 1b, which was computed over a limited wavenumber range $k_1<k<k_2$, where $k_1 = 2\pi(102.4\text{ km})^{-1}$ and $k_2 = 2\pi(0.8\text{ km})^{-1}$. Thus, integrating this spectrum gives us some fraction, ϵ, of T_0^2. We estimate ϵ by numerically integrating $G_T(m,\omega)$ in (2) over all m and ω and comparing it with a second integral constrained within the range $k_1<k<k_2$. Figure 3 shows a sample contour plot of $G_T(m,\omega)$ for $m_*=2\pi(3\text{ km})^{-1}$. The shaded region shows the integration range on restriction to the horizontal wavenumber range $k_1<k<k_2$. Using a typical stratospheric value of $m_*=2\pi(3\text{ km})^{-1}$ (Tsuda *et al.* 1991), we obtain $\epsilon = 0.21$ using representative midlatitude f and N values. Thus, according to the continuous phase speed model (2), a little over one fifth of the total variance T_0^2 is contained in the horizontal wavenumber PSDs shown in Figure 1b and B96.

On numerically integrating the 1D temperature PSD in Figure 1b, we obtain a variance of 0.16 K^2, and thus a total variance $T_0^2 = 0.16/\epsilon \approx 0.8\text{ K}^2$. This is a small value compared to other measurements and analyses (e.g., Tsuda *et al.* 1991; Allen and Vincent 1995), but it should kept in mind that a significant fraction of the total ER-2 flight miles during these experiments occurred over open ocean, where wave variances are smaller than those over land (e.g., Nastrom *et al.* 1987). Furthermore, the mean spectra in Figure 1b and B96 are log-averages of wavelet spectra taken during 1024 s flight intervals. Log-averages deemphasize periods of high activity, and thus the variance of the log-average spectrum is less than the mean variance of the data. Nevertheless, our estimate of $T_0^2 \approx 1\text{ K}^2$ can be considered broadly representative of "ambient" stratospheric conditions, or a "lower bound" estimate. In any given situation, T_0^2 may be considerably larger, and may depend on environmental factors such as underlying cloudiness and terrain, background winds (at all levels), altitude, and so on. A sample parcel-based temperature fluctuation time series using $T_0^2=0.76\text{ K}^2$ in (13) is shown in Figure 4a.

Temperature perturbation time series for the MG95 parameterization can also be generated by replacing $\hat{B}_T^{B96}(\omega_i)$ in (13) with the corresponding normalized MG95 spectrum, $U^{-1}\hat{F}_T(\omega_i/U)$, from (5). Figure 4b shows the resulting time series, using the same n, T_0 and ϕ_i values as in Figure 4a, U=50 m s^{-1}, and where the shape and wavenumber range of the temperature PSD in Figure 1b was used to specify $\hat{F}_T(\omega_i/U)$. Note the smaller time range and the "rougher" appearance of this time series, due to higher frequency content and a different spectral shape. This time series also highlights a serious shortcoming of the MG95 parameterization: that the gravity-wave frequency limits $|\ f\ |<|\ \omega\ |< N$ are not imposed

in this parameterization, and thus unphysical high-frequency temperature oscillations are simulated within air parcels when U is large.

An additional general caveat must be made about the use of (13) to generate parcel-based temperature fluctuations. For multi-parcel trajectory models, we would expect some degree of spatial correlation between the temperature perturbations within closely adjacent parcels. A straightforward application of (13) within such models will not provide these correlations. However, (13) can be generalized to provide spatio-temporal parcel-based temperature fluctuation fields $T'(x, y, z, t)$ using the complete four-dimensional model power spectrum $H_T(k, l, m, \omega)$, assuming isotropy or some other simple directional dependence in wave propagation directions (e.g., Gardner *et al.* 1993a 1993b).

5. Microphysical Effects of the Parameterizations

Figures 4a-b show that the B96-based and MG95 parameterizations lead to noticeable differences in simulated mesoscale temperature variability along an air parcel trajectory. Meilinger *et al.* (1995) and Tsias *et al.* (1997) have shown that rapid temperature fluctuations can cause the composition of liquid stratospheric aerosols to depart from equilibrium. The extent of non-equilibrium depends upon the cooling and heating rates of air parcels (Tsias *et al.* 1997), with more rapid cooling and heating leading to greater departures from equilibrium. Under conditions where the stratospheric aerosol is composed principally of H_2SO_4 and H_2O (typically at temperatures $T >$ 195-200 K), the effect of temperature fluctuations can largely be ignored since equilibrium between gas phase H_2O and the droplets is rapidly achieved. The greatest departures from equilibrium occur under conditions where HNO_3 is strongly partitioned from the gas phase into the liquid aerosol, which is typically at $T <$ 195-200 K (Carslaw *et al.* 1997).

Here, we investigate how each parameterization affects the evolution of ternary $H_2O/HNO_3/H_2SO_4$ aerosol droplets by inserting the time series in Figure 4a-b into the nonequilibrium microphysical box-trajectory model of Meilinger *et al.* (1995). We also investigate the effect of these temperature fluctuations on the growth and evaporation of nitric acid trihydrate (NAT) particles. Our aim is to examine how the different natural background temperature fluctuations might affect the instantaneous volumes of these typical stratospheric particles.

In the experiments using this model, parcels were advected along the Θ = 454 K isentrope using an initial water vapor mixing ratio of 5 ppmv and an initial gas-phase HNO_3 mixing ratio of 10 ppbv. The perturbation time series in Figure 4a-b were superimposed upon the mean temperature, and four separate experiments were conducted for each time series using $\bar{T}$=188, 190, 191.5 and 193 K (with corresponding mean pressures $\bar{p}$=47, 48.7, 50, and 51.4 hP, respectively[2]). Total aerosol volume and temperature within the parcel were calculated and recorded at each time step. Results for all four experiments using the B96-based and MG95-based temperature perturbation time series are collated and plotted in Figures 4c and 4d, respectively. The thin black line on both panels represents the thermodynamical equilibrium curve of Carslaw *et al.* (1994). Also indicated on each figure is the approximate amount of scatter in observed aerosol volumes (in terms of the equivalent scatter in temperature) measured by Dye *et al.* (1992) on 24 January 1989. These observations were used by Carslaw *et al.* (1994), Tabazadeh *et al.* (1994) and Drdla *et al.* (1994) for comparison with volumes calculated using a liquid aerosol model assuming thermodynamic equilibrium.

Figures 4c and 4d show that the temperature fluctuations in both the B96-based and MG95 parameterization lead to significant scatter in aerosol volume around the thermodynamic equilibrium value. This is because the time constant for diffusive growth and shrinking of the droplets by HNO_3 mass transfer is rather large compared to the rate of change of air parcel temperature that induces the size changes [for a discussion of these time constants,

---

[2]Note that Carslaw *et al.* (1994) used a constant pressure of 55 hPa in calculating aerosol volumes as a function of temperature, implying a change in potential temperature between the different temperatures. Here, the calculations refer to aerosol volumes on a constant potential temperature level. The difference in volume is small.

see Meilinger *et al.* (1995)]. In particular, it is the large droplets whose growth is diffusively hindered, while, as pointed out by Meilinger *et al.* (1995) and Tsias *et al.* (1997), the small droplets adjust their mass rapidly to changes in temperature. However, these small droplets do not contribute significantly to the total aerosol mass. For both the B96-based and MG95 gravity-wave parameterizations, the departures in aerosol volume from equilibrium are even greater than those produced by rapid synoptic-scale cooling (Carslaw *et al.* 1997).

The results using the MG95 parameterization (Figure 4d) show a great deal more scatter about the equilibrium line in the 189 to 193 K range than the B96-based results in Figure 4c. Since there is more rapid heating and cooling of parcels in the MG95 parameterization (see Figure 4a-b), large aerosol droplets can be rapidly heated to high temperatures before they can adjust by evaporating mass, leading to larger departures from the equlilibrium curve. Aerosol volumes a factor of 5–10 larger than equilibrium predictions occur in Figure 4d. Nonequilibrium behavior is also evident in the B96-based experiments (Figure 4c) but is much less pronounced, with aerosol volumes generally less than a factor of two greater than equilibrium predictions. The strong nonequilibrium behavior in the MG95 parameterization also produces a higher total mean aerosol volume than in the B96-based parameterization.

Clearly the amount of scatter in the B96 case is much closer to that observed by Dye *et al.* (1992) than is the case for the MG95 trajectory. This may reflect the fact that the MG95 trajectory yields unrealistically rapid cooling and heating rates, and therefore unrealistically broad scatter of calculated aerosol volumes. The calculated scatter in liquid aerosol volumes in the B96 case indicates the "natural" range of scatter along an individual trajectory arising from a background of mesoscale temperature fluctuations. The scatter observed by Dye *et al.* (1992) most likely includes this effect, but also contains scatter arising from air-mass variations, as well as from instrument noise, particularly at low volumes. Another source of scatter in the measurements is that due to different particle types (most likely in different air masses). The Dye *et al.* observations from 24 January 1989 appear to be consistent with pure liquid ternary aerosols at all temperatures, which is not the case for observations on other days. Note that the calculated scatter shown here is apparent only where aerosol volumes increase sharply with decreasing temperature, while scatter is apparent at all temperatures in the Dye *et al.* data. From their measurements alone, it is not possible to say how much of the observed scatter in aerosol volumes was produced by mesoscale temperature fluctuations. However, the observed scatter in the data should represent an upper limit on estimates of the true value of scatter due to temperature fluctuations.

We now consider the effect of the B96-based temperature fluctuations on NAT growth (Fig. 5) using an extended version of the Meilinger *et al.* (1995) model (Tsias *et al.* 1997). We show a case where 1% of the background liquid aerosols are assumed to be nucleated as NAT (corresponding to about 0.1 cm^{-3}). NAT particles were assumed to form and evaporate at the NAT equilibrium temperature. It is likely that NAT formation may require a large degree of supercooling, or may even occur heterogeneously on ice at temperatures several Kelvins lower. The calculated scatter shown here is therefore a lower limit to that expected in reality. Figure 5 shows the scatter in total aerosol volume, and is therefore comparable with aerosol volume measurements. The effect of liquid aerosols is relatively minor, so the volumes shown are also rather similar to those of NAT alone. The amount of scatter is now considerably greater than was the case for liquid aerosol growth. The reason is that, with only 0.1 NAT particles cm^{-3}, the individual particles grow rather large and are therefore more strongly diffusively-limited than the many smaller liquid aerosols. The amount of scatter is the same as the amplitude of the temperature fluctuations themselves. With 100% NAT activation, the scatter again resembles that for liquid aerosols, while for even fewer NAT particles it is somewhat greater. For the MG95 temperature fluctuations and 1% NAT, the amount of scatter is somewhat larger than that obtained with the B96-based time series, although the difference is not as pronounced as it was for the liquid aerosols. As the number density of NAT particles increases, the difference in scatter between B96 and MG95 NAT aerosol volumes also increases.

These calculations indicate that, even under "passive" background synoptic conditions, a large amount of scatter in aerosol volume can occur due to mesoscale temperature perturbations. Although we have compared the calculated scatter with a single set of *in situ* particle volume observations, we believe such a "natural" scatter will be present in all such particle ensembles. This sets a natural limit on the "quality" of particle volume and composition measurements. Under some conditions this may make identification of NAT and

liquid aerosols in the stratosphere from volume observations alone very difficult unless non-equilibrium growth is taken into account.

6. Summary and Discussion

The work of MG95 indicated that the temperature perturbations produced by a spectrum of stratospheric gravity waves had important effects on stratospheric microphysics. Here, we presented revised models of the PSDs of mesoscale temperature and heating/cooling rate perturbations due to such waves, based on the spectral data of B96. The shapes of these PSDs were significantly different from those obtained by MG95. We derived a heating/cooling rate PSD that is more steeply decreasing at the smallest horizontal scales, and is far less sensitive to variations in background wind speed (Figure 1a). Overall, RMS cooling rates using the B96-based model were significantly smaller than those derived by MG95.

We developed a simple method for generating random time series of temperature perturbations within air parcels, as governed by either the MG95 or B96-based spectral parameterization. These time series were imported into a microphysical box model to assess the microphysical consequences of each parameterization. Both parameterizations generated total aerosol volumes as a function of air-parcel temperature that departed significantly from equilibrium (Figure 4c-d). The MG95 parameterization generated aerosol volumes that exceeded equilibrium values by up to a factor of 10. The B96-based approach yielded smaller departures, with aerosol volumes generally within a factor of 2 of equilibrium predictions.

The ER-2 aerosol volume *versus* temperature data of Dye *et al.* (1992) show significant scatter about the equilibrium curve. In flights for which air mass variations were estimated to be small, aerosol volume as a function of temperature does not appear to show the large departures from equilibrium predicted by the MG95 approach (Figure 4d). As dicusssed in section 4, the total temperature variance of $T_0^2 = 0.76$ K^2 used in Figure 4 is probably a lower bound, and use of a larger T_0^2 in Figure 4 would yield even greater departures from equilibrium using the MG95 parameterization. Thus, the degree of scatter in the aerosol volume data of Dye *et al.* (1992) is more closely approximated by a microphysical model using a B96-based parameterization of typical stratospheric mesoscale temperature variability (Figure 4c).

The differences between the MG95 and B96-based approaches to parameterizing adiabatic gravity-wave heating and cooling perturbations arise from the frequency spectrum assumed for the gravity waves in each approach. MG95 assumed (implicitly) a wave field composed entirely of stationary waves, which yields a single intrinsic phase speed that is of similar magnitude to the background stratospheric wind. The B96-based approach assumes that a broad distribution of intrinsic wave phase speeds is present, with a peak centered ~ 10 m s^{-1} in the lower stratosphere. Thus, waves in B96 are assumed to "run with" the background flow to a large degree, reducing the relative speed of air parcels with respect to the waves in regions where background winds are large (e.g., near the edge of the polar vortex).

The full implications of these differences for stratospheric microphysics are not yet clear. Generally speaking, however, both instantaneous and time-averaged aerosol volumes and surface areas will be larger using the MG95 parameterization. However, the duration of cold temperature events due to gravity waves are longer using the B96-based parameterization. This extended residence time in cold conditions could, for example, lead to increased settling of particles. The time evolution of heterogeneous reactions with strong temperature dependences could also depend on the shape of the frequency spectrum assumed for wave-induced temperature fluctuations. More work is needed to assess these possibilities fully.

We consider it unlikely that the background temperature fluctuations described here could induce nucleation of recognized nitric acid hydrates. The work of Tsias *et al.* (1997) shows that large amplitude (>6 K peak to peak) rapid cooling and warming events, such as found in localised mountain-induced gravity waves, would be necessary. In such events, the composition of $HNO_3/H_2SO_4/H_2O$ droplets can approach almost binary HNO_3/H_2O with HNO_3 concentrations in the liquid as high as 59 wt%, leading to the possible nucleation of nitric acid dihydrate from the droplets. Temperature fluctuations as large and rapid as these are not found in the gravity wave temperature time series considered here (see Figure 4a).

Therefore, hydrate nucleation in temperature fluctuations may well be restricted to regions of the stratosphere directly affected by large-amplitude mountain waves [see, e.g., Fig. 2 of Carslaw *et al.* (1998b)]. Note, however, that these arguments refer only to homogeneous freezing of nitric acid hydrates from the liquid. As shown by Tabazadeh *et al.* (1996), background gravity wave temperature fluctuations may sometimes be sufficient to push air parcel temperatures sufficiently below the ice frost point to cause ice nucleation. However, the magnitude of the associated heating/cooling rate fluctuations ($D_t T'$) probably have little influence on this mechanism.

From a purely physical viewpoint, we believe that the B96-based parameterization will be more realistic than the MG95 approach in most circumstances. In "passive" environments away from strong wave sources, gravity wave spectra have characteristic shapes. While the processes responsible for generating these spectral shapes are still being debated (e.g., Hines 1991; Gardner 1996; Dewan 1997), canonical spectral models that are constrained by the gravity-wave dispersion relation, like (1), do a good job in interrelating a wide range of observed gravity wave spectra. In particular, B96 showed that the shapes and intensities of stratospheric horizontal wavenumber spectra measured by aircraft were well predicted by these models. The B96-based parameterization presented here is an extension of these same models to temperature and heating/cooling rate spectra. However, if spectral models other than (1) are preferred, corresponding temperature and heating/cooling rate PSDs can be easily derived from them using similar derivations to those in section 2. The MG95 parameterization, on the other hand, is not constrained by the gravity wave dispersion relation, and can generate unphysical high frequency ($\omega > N$) temperature fluctuations within parcels advected by strong winds.

In regions close to strong wave sources, it is likely that neither spectrally-based approach will be the best way to estimate wave temperature perturbations. Alternative models of direct wave propagation from orographic or convective source regions show more promise in this regard (e.g. Bacmeister *et al.* 1994, 1997b; Alexander 1996; Leutbecher and Volkert 1996), and have started to be incorporated into regional microphysical models (Carslaw *et al.* 1998a, 1998b, 1998c). A complete parameterization of gravity wave effects for chemical and microphysical models may require both a spectral approach, to capture the small-amplitude relatively-ubiquitous background wave field, and explicit event-by-event modeling to capture the rarer large-amplitude wave events generated by strong underlying sources.

Acknowledgements. This research was supported in part by contracts W-18,566 and NAS5-98XXX of NASA's Atmospheric Chemistry Modeling and Analysis Program, and contract NAS5-97247 of NASA's Atmospheric Effects of Aviation/Subsonic Assessment Program.

References

Alexander, M. J., A simulated spectrum of convectively generated gravity waves: Propagation from the tropopause to the mesopause and effects on the middle atmosphere, *J. Geophys. Res., 101,* 1571-1588, 1996.

Alexander, M. J., and L. Pfister, Gravity wave momentum flux in the lower stratosphere over convection, *Geophys. Res. Lett., 22,* 2029-2032, 1995.

Allen, S. J., and R. A. Vincent, Gravity-wave activity in the lower atmosphere: Seasonal and latitudinal variations, *J. Geophys. Res., 100,* 1327-1350, 1995.

Bacmeister, J. T., M. R. Schoeberl, L. R. Lait, P. A. Newman, and B. Gary, ER-2 mountain wave encounter over Antarctica: Evidence for blocking. *Geophys. Res. Lett,* 17, 81-84, 1990.

Bacmeister, J. T., S. D. Eckermann, P. A. Newman, L. Lait, K. R. Chan, M. Loewenstein, M. H. Proffitt and B. L. Gary, Stratospheric horizontal wavenumber spectra of winds, potential temperature and atmospheric tracers observed by high-altitude aircraft. *J. Geophys. Res.*, 101, 9441-9470, 1996.

Bacmeister, J. T., S. D. Eckermann, L. Sparling, K. R. Chan, M. Loewenstein, and M. H. Proffitt, Analysis of intermittency in aircraft measurements of velocity, temperature and atmospheric tracers using wavelet transforms, To appear in NATO ASI Series, Vol. 1, *Gravity Wave Processes and their Parameterization in Global Climate Models*, ed. K. P. Hamilton, Springer Verlag, Heidelberg, 1997a.

Bacmeister, J. T., S. D. Eckermann, and C. J. Marks, Analysis and modeling of stratospheric gravity wave activity along ER-2 flight tracks, in The Proceedings of the First SPARC General Assembly, WMO World Climate Research Report No. 99, Vol I, 283-286, 1997b.

Benzi, R. L., A. Biferale, A. Crisanti, G. Paladin, M. Vergassola, and A. Vulpani, A random process for the construction of multiaffine fields, *Physica D, 65*, 352-358, 1993.

Borrmann, S., S. Solomon, J. E. Dye, D. Baumgardner, K. K. Kelly, and K. R. Chan, Heterogeneous reactions on stratospheric background aerosols, volcanic sulfuric acid droplets, and type I polar stratospheric clouds: Effects of temperature fluctuations and differences in particle phase, *J. Geophys. Res., 102*, 3639-3648, 1997.

Cariolle, D., S. Muller, F. Cayla, and M. P. McCormick, Mountain waves, polar stratospheric clouds, and the ozone depletion over Antarctica, *J. Geophys. Res., 94*, 11233-11240, 1989.

Carslaw, K.S., B. P. Luo, S. L. Clegg, Th. Peter, P. Brimblecombe, and P. J. Crutzen, Stratospheric aerosol growth and HNO3 gas phase depletion from coupled HNO3 and water uptake by liquid particles, *Geophys. Res. Lett., 21*, 2479-2482, 1994.

Carslaw, K.S., Th. Peter, and S. L. Clegg, Modeling the composition of liquid stratospheric aerosols, *Rev. Geophys., 35*, 125-154, 1997.

Carslaw, K. S., M. Wirth, A. Tsias, B. P. Luo, A. Dörnbrack, M. Leutbecher, H. Volkert, W. Renger, J. T. Bacmeister, and T. Peter, Particle microphysics and chemistry in remotely observed mountain polar stratospheric clouds, *J. Geophys. Res., 103*, 5785-5796, 1998a.

Carslaw, K. S., M. Wirth, A. Tsias, B. P. Luo, A. Dörnbrack, M. Leutbecher, H. Volkert, W. Renger, J. T. Bacmeister, E. Reimer, and T. Peter, Increased stratospheric ozone depletion due to mountain-induced atmospheric waves, *Nature*, 391, 675-678, 1998b.

Carslaw, K. S., T. Peter, J. T. Bacmeister, and S. D. Eckermann, Widespread solid polar stratospheric cloud formation by mountain waves in the Arctic, *J. Geophys. Res., (submitted)*, 1998c.

Deshler, T., T. Peter, R. Müller, and P. Crutzen, The lifetime of leewave-induced ice particles in the Arctic stratosphere, I, Balloonborne observations, *Geophys. Res. Lett., 21*, 1327-1330, 1994.

Dewan, E. M., Saturated-cascade similitude theory of gravity wave spectra, *J. Geophys. Res., 102*, 29,799–29,817, 1997.

Drdla, K., and R. P. Turco, Denitrification through PSC formation: A 1D model incorporating temperature oscillations, *J. Atmos. Chem.*, 12, 319-366, 1991.

Drdla, K., A. Tabazadeh, R. P. Turco, M. Z. Jacobson, J. E. Dye, C. Twohy, and D. Baumgardner, Analysis of the physical state of one Arctic polar stratospheric cloud based on observations, *Geophys. Res. Lett., 21*, 2475-

2478, 1994.

Dye, J. E., D. Baumgardner, B. W. Gandrud, S. R. Kawa, K. K. Kelly, M. Loewenstein, G. V. Ferry, K. R. Chan, and B. L. Gary, Particle size distributions in Arctic polar stratospheric clouds, growth and freezing of sulfuric acid droplets, and implications for cloud formation, *J. Geophys. Res., 97,* 8015-8034, 1992.

Eckermann, S. D., Effects of nonstationarity on spectral analysis of mesoscale motions in the atmosphere, *J. Geophys. Res., 95,* 16,685-16,703, 1990.

Eckermann, S. D., Effect of background winds on the vertical wavenumber spectrum of atmospheric gravity waves, *J. Geophys. Res., 100,* 14097–14112, 1995.

Eckermann, S. D., D. E. Gibson-Wilde, and J. T. Bacmeister, Gravity-wave perturbations of minor constituents: a parcel advection methodology, *J. Atmos. Sci., (in* press), 1998.

Elliott Jr., F. W., D. J. Horntrop, and A. J. Majda, A Fourier-wavelet Monte Carlo method for fractal random fields, *J. Comp. Phys.*, 132, 384-408, 1997.

Fritts, D. C., and T. E. VanZandt, Spectral estimates of gravity wave energy and momentum fluxes, Part I: Energy dissipation, acceleration and constraints, *J. Atmos. Sci., 50,* 3685-3694, 1993.

Fromm, M. D., J. D. Lumpe, R. M. Bevilacqua, E. P. Shettle, J. Hornstein, S. T. Massie, and K. H. Fricke, Observations of Antarctic polar stratospheric clouds by POAM II: 1994-1996, *J. Geophys. Res., 102,* 23,659-23,672, 1997.

Gardner, C. S., Testing theories of atmospheric gravity wave saturation and dissipation, *J. Atmos. Terr. Phys.*, 58, 1575–1589, 1996.

Gardner, C. S., C. A. Hostetler, and S. J. Franke, Gravity wave models for the horizontal wave number spectra of atmospheric velocity and density perturbations, *J. Geophys. Res., 98,* 1035-1049, 1993a.

Gardner, C. S., C. A. Hostetler, and S. Lintelman, Influence of the mean wind field on the separability of atmospheric perturbation spectra, *J. Geophys. Res., 98,* 8859-8872, 1993b.

Godin, S., G. Mégie, C. David, D. Haner, C. Flesia, and Y. Emery, Airborne lidar observation of mountain-wave-induced polar stratospheric clouds during EASOE, *Geophys. Res. Lett., 21,* 1335-1338, 1994.

Hines, C. O., The saturation of gravity waves in the middle atmosphere. Part II: Development of Doppler-spread theory, *J. Atmos. Sci., 48,* 1360-1379, 1991.

Jensen, E. J., and G. E. Thomas, Numerical simulations of the effects of gravity waves on noctilucent clouds, *J. Geophys. Res., 99,* 3421-3430, 1994.

Jensen, E. J., and O. B. Toon, Ice nucleation in the upper troposphere: Sensitivity to aerosol number density, temperature and cooling rate, *Geophys. Res. Lett., 21,* 2019-2022, 1994.

Jensen, E. J., O. B. Toon, L. Pfister, and H. B. Selkirk, Dehydration of the upper troposphere and lower stratosphere by subvisible cirrus clouds near the tropical tropopause, *Geophys. Res. Lett., 23,* 825-828, 1996.

Koop, T., U. M. Biermann, W. Raber, B. P. Luo, P. J. Crutzen, and T. Peter, Do stratospheric aerosol droplets freeze above the ice frost point?, *Geophys. Res. Lett., 22,* 917-920, 1995.

Koop, T., B. P. Luo, U. M. Biermann, P. J. Crutzen, and

T. Peter, Freezing of HNO3/H2SO4/H2O solutions at stratospheric temperatures: Nucleation statistics and experiments, *J. Phys. Chem., 101,* 1117-1133, 1997.

Leutbecher, M., and H. Volkert, Stratospheric temperature anomalies and mountain waves: a three-dimensional simulation using a multiscale weather prediction model, *Geophys. Res. Lett., 23,* 3329-3332, 1996.

Lin, H., K. J. Noone, J. Ström, and A. J. Heymsfield, Dynamical influences on cirrus cloud formation process, *J. Atmos. Sci., 55,* 1940-1949, 1998.

Meilinger, S. K., T. Koop, B. P. Luo, T. Huthwelker, K. S. Carslaw, U. Krieger, P. J. Crutzen, and T. Peter, Size-dependent stratospheric droplet composition in lee wave temperature fluctuations and their potential role in PSC freezing, *Geophys. Res. Lett., 22,* 3031-3034, 1995.

Murphy, D. M., and B. L. Gary, Mesoscale temperature fluctuations and polar stratospheric clouds. *J. Atmos. Sci., 52,* 1753-1760, 1995.

Nastrom, G. D., and K. S. Gage, A climatology of atmospheric wavenumber spectra of wind and temperature observed by commercial aircraft, *J. Atmos. Sci., 42,* 950-960, 1985.

Nastrom, G. D., D. C. Fritts, and K. S. Gage, An investigation of terrain effects on the mesoscale spectrum of atmospheric motions, *J. Atmos. Sci., 44,* 3087-3096, 1987.

Owens, A. J., A algorithm for generating fluctuations having an arbitrary power spectrum, *J. Geophys. Res., 83,* 1673-1675, 1978.

Peter, T., R. Müller, P. J. Crutzen, and T. Deshler, The lifetime of leewave-induced ice particles in the Arctic stratosphere, II, Stabilization due to NAT-coating, *Geophys. Res. Lett., 21,* 1331-1334, 1994.

Potter, B. E., and J. R. Holton, The role of monsoon convection in the dehydration of the lower tropical stratosphere, *J. Atmos. Sci., 52,* 1034-1050, 1995.

Tabazadeh, A., R. P. Turco, K. Drdla, M. Z. Jacobson, and O. B. Toon, A study of type I polar stratospheric cloud formation, *Geophys. Res. Lett., 21,* 1619-1622, 1994.

Tabazadeh, A., O. B. Toon, B. L. Gary, J. T. Bacmeister, and M. R. Schoeberl, Observational constraints on the formation of type 1a polar stratospheric clouds. *Geophys. Res. Lett., 23,* 2109-2112, 1996.

Tsias, A., A. J. Prenni, K. S. Carslaw, T. P. Onasch, B. P. Luo, M. A. Tolbert, and T. Peter, Freezing of polar stratospheric clouds in orographically induced strong warming events, *Geophys. Res. Lett., 24,* 2303-2306, 1997.

Tsuda, T., T. E. VanZandt, M. Mizumoto, S. Kato, and S. Fukao, Spectral analysis of temperature and Brunt-Väisälä frequency fluctuations observed by radiosondes, *J. Geophys. Res., 96,* 17,265-17,278, 1991.

Turco, R. P., O. B. Toon, R. C. Whitten, R. G. Keesee, and D. Hollenbach, Noctilucent clouds: simulation studies of their genesis, properties and global influences, *Planet. Space Sci., 30,* 1147-1181, 1982.

Vincent, R. A., and S. D. Eckermann, VHF radar observations of mesoscale motions in the troposphere: Evidence of gravity wave Doppler shifting, *Radio Sci.,* 25, 1019-1037, 1990.

Whiteway, J. A., T. J. Duck, D. P. Donovan, J. C. Bird, S. R. Pal, and A. I. Carswell, Measurements of gravity wave activity within and around the Arctic stratospheric vortex, *Geophys. Res. Lett., 24,* 1387-1390, 1997.

(Received _____)

RMS heating/cooling rates within logarithmically-spaced horizontal scale ranges, using the B96-based model

Horizontal Scale Range (km)	Heating/Cooling Rate (K day^{-1})
102.4 – 25.6	52
51.2 – 12.8	71
25.6 – 6.4	86
12.8 – 3.2	87
6.4 – 1.6	70
3.2 – 0.8	47

Figure 1. (a) Power spectral density (PSD) of heating/cooling rate as a function of horizontal wavenumber k. (b) PSD of temperature as a function of k. PSD's in (a) and (b) are obtained from log-averages over all flights in AASE II, SPADE, and ASHOE/MAESA. Filled triangles in (a) show cooling rates obtained by scaling the mean PSD of vertical velocity as shown in (3). Solid, dotted and dashed lines show cooling rates obtained from the horizontal derivative of the mean temperature in (b), following MG95. Results shown are for 3 different values of mean wind U; 20, 50 and 1 m s^{-1}.

Figure 2. Log_{10} of normalized PDF's of temperature fluctuation amplitude determined using discreet wavelet transforms of MMS temperatures measured during ASHOE/MAESA. Thick dashed curves show Gaussian fits (which appear parabolic here) to the central 68% of data. Results are shown for fluctuations with characteristic horizontal scales of (a) 12.8 km, (b) 6.4 km, (c) 3.2 km, and (d) 1.6 km. Fluctuation amplitudes appear to be well described by a normal distribution in the central or small amplitude portion of the distribution. However, PDF's show non-Gaussian, high-amplitude tails especially at smaller horizontal scales. These may be associated with infrequent high-amplitude wave events, such as waves generated by intense convection or flow over mountains.

Figure 3. Model power spectral density (PSD) of temperature as a function of vertical wavenumber m and intrinsic frequency ω, $G_T(m,\omega)$, from (2) based on the separable model (1) of Gardner *et al.* (1993a). Contours of this two-dimensional PSD for $m_*=2\pi(3.0\text{ km})^{-1}$ are shown with solid curves. Cusps in the contours at $m=m_*$ mark the shape change in $\hat{A}_{uv}(m)$ in (1). $G_T(m,\omega)$ is identically zero for $\omega>|N|=0.02$ rad s^{-1} and $\omega<|f|=10^{-4}$ rad s^{-1}. Shaded region shows portions of the (m,ω)-plane enclosed by curves of constant horizontal wavenumber corresponding to the range of horizontal scales between 102.4 km and 0.8 km. For $m_*=2\pi(3.0\text{ km})^{-1}$ approximately 21% of total variance lies within this shaded region.

Figure 4. (a) Temperature as a function of time for an air parcel advected through a random field of gravity waves with an intrinsic frequency spectrum $B(\omega)\sim\omega^{-2}$ between f and N (B96-based approach). (b) Temperature history for an air parcel traversing a stationary wave field with a temperature power spectrum like that in Figure 1b (MG95 approach). A relative speed of 50 m s^{-1} is assumed for the air parcel with respect to wave field. A total temperature variance $T_0^2\approx0.76$ K^2 was used in both cases. Total aerosol volume as a function of temperature for the two different parameterizations of gravity wave temperature fluctuations, (a) and (b), are shown in panels (c) and (d), respectively. Aerosol volumes were calculated for ternary $HNO_3/H_2SO_4/H_2O$ droplets using the box model of Meilinger *et al.* (1995). Each of the aerosol volume plots in (c) and (d) combines the results of 4 calculations using the temperature perturbation histories in (a) and (b), with different mean temperatures of 188, 190, 191.5 und 193 K. The thin black line in each panel is the thermodynamic equilibrium result for ternary droplets (Carslaw *et al.* 1994). Arrows depict the approximate range of scatter in the data of Dye *et al.* (1992).

Figure 5. Total aerosol volume as a function of temperature for NAT particles, where 1% of the background liquid aerosols is assumed to be nucleated as NAT. Results were derived using the parcel-based temperature time series in Figure 4a (B96), using four different mean temperatures of 188, 190, 191.5 and 193 K. Solid line is NAT volume at equilibrium, dashed line is liquid $HNO_3/H_2SO_4/H_2O$ droplet volume at equilibrium.

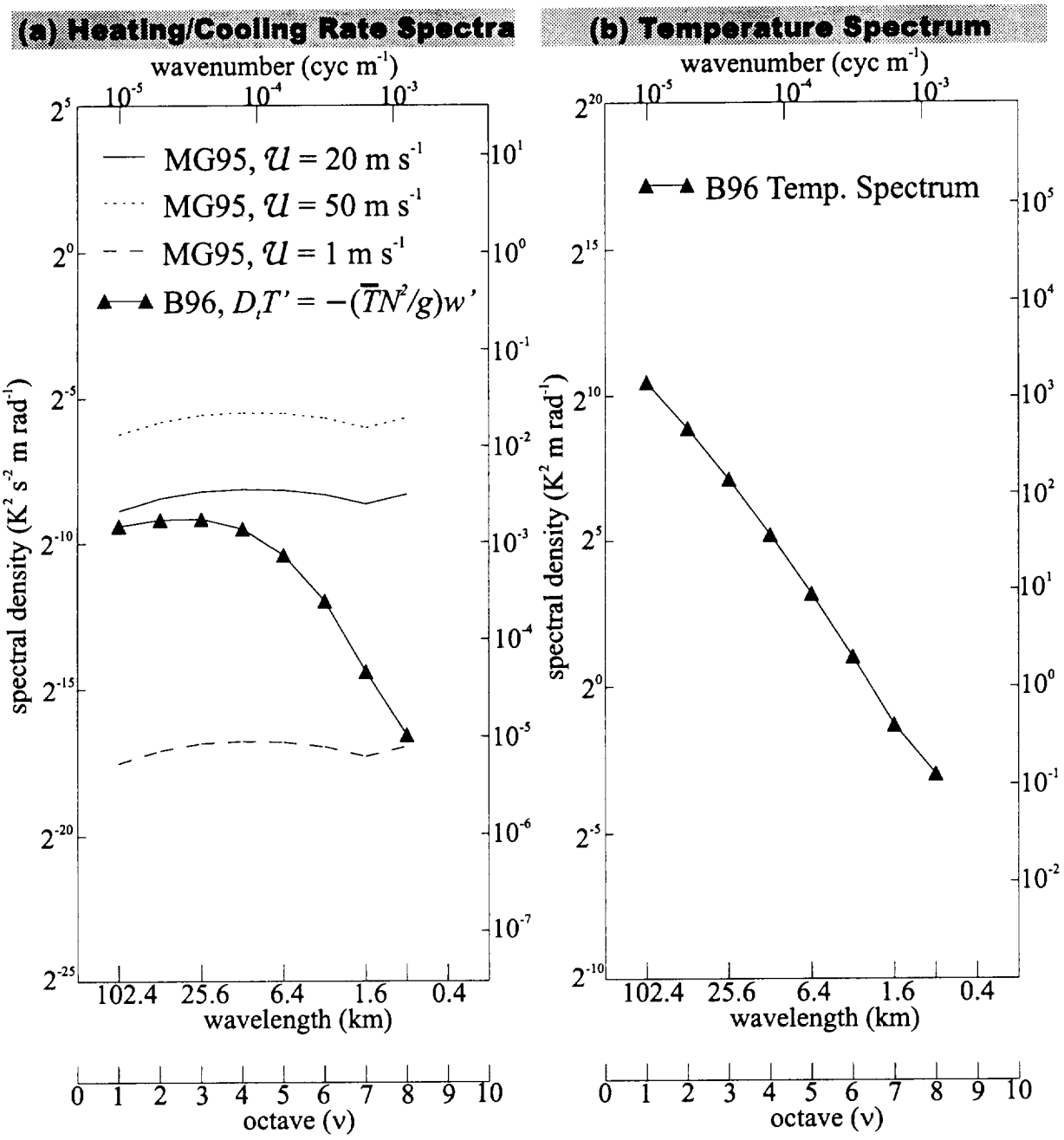
(a) Heating/Cooling Rate Spectra
(b) Temperature Spectrum
wavenumber (cyc m-1)
MG95, U = 20 m s-1
MG95, U = 50 m s-1
MG95, U = 1 m s-1
B96, D_t T' = −(T̄N²/g)w'
B96 Temp. Spectrum
spectral density (K² s-2 m rad-1)
spectral density (K² m rad-1)
wavelength (km)
102.4 25.6 6.4 1.6 0.4
octave (ν)
0 1 2 3 4 5 6 7 8 9 10

Figure 1

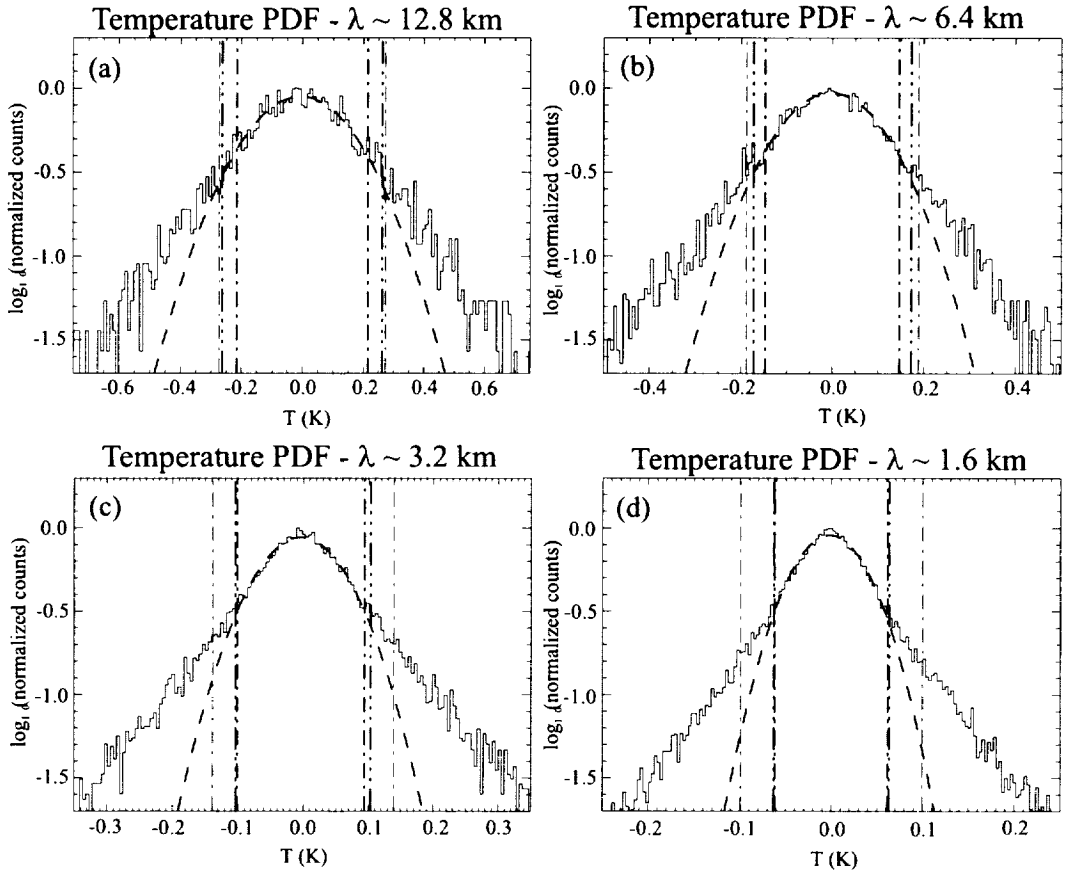
Temperature PDF - λ ~ 12.8 km
(a)
Temperature PDF - λ ~ 6.4 km
(b)
Temperature PDF - λ ~ 3.2 km
(c)
Temperature PDF - λ ~ 1.6 km
(d)
log10 (normalized counts)
T (K)

Figure 2

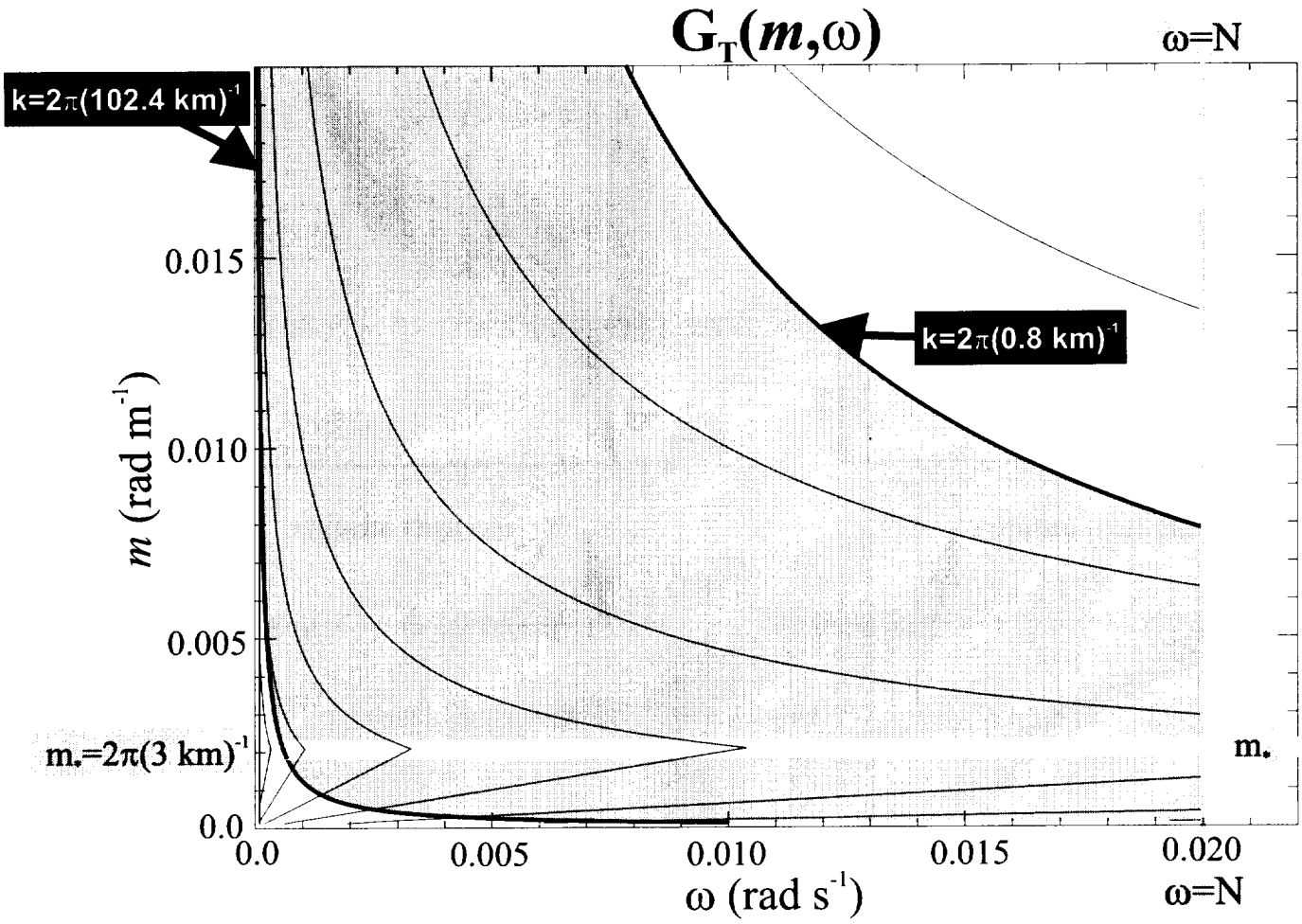
$G_T(m,\omega)$
ω=N
k=2π(102.4 km)$^{-1}$
k=2π(0.8 km)$^{-1}$
0.015
0.010
0.005
0.0
m (rad m^{-1})
m_*=2π(3 km)$^{-1}$
m_*
0.0
0.005
0.010
0.015
0.020
ω (rad s^{-1})
ω=N

Figure 3

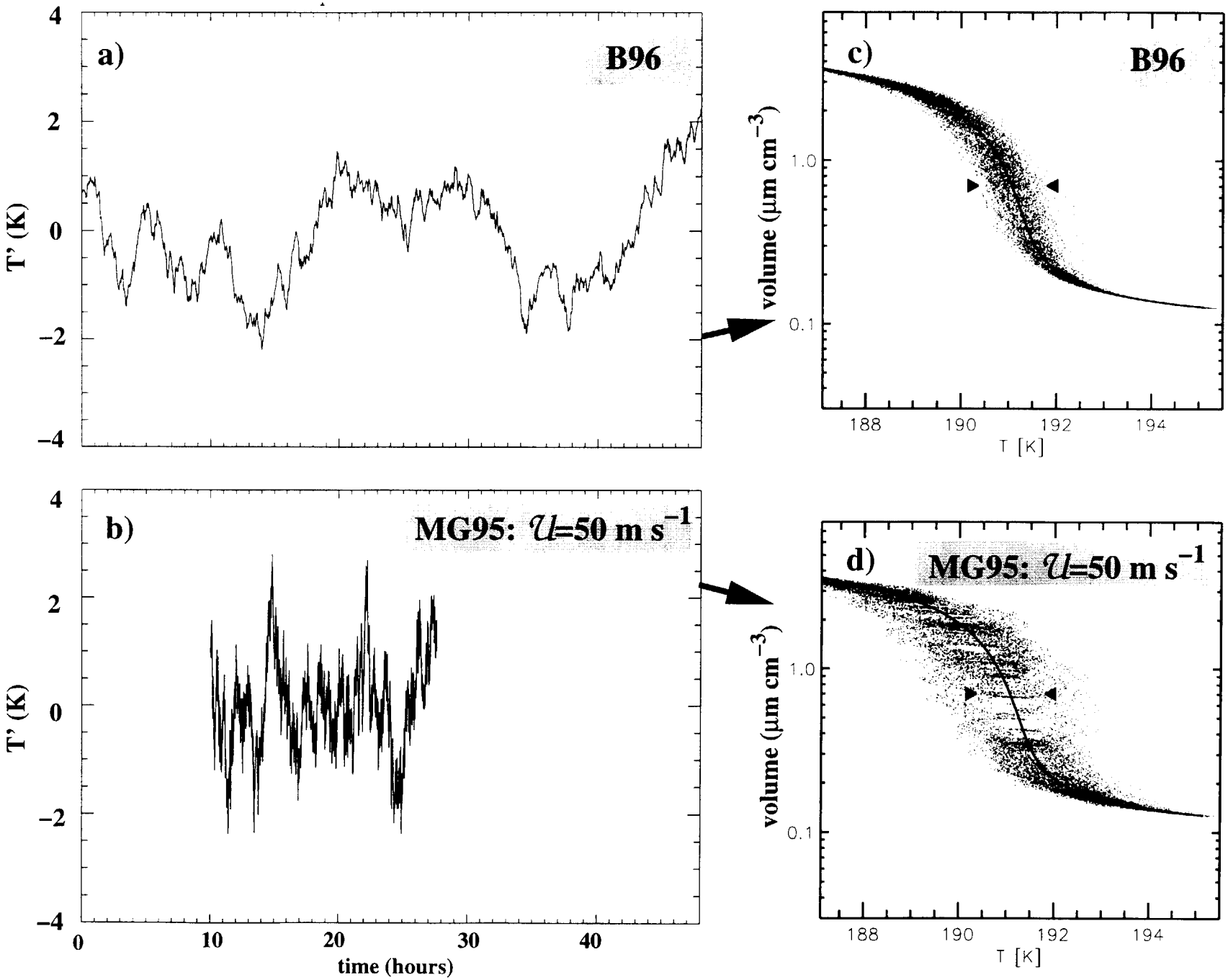
a)
B96
T' (K)
4
2
0
−2
−4
b)
MG95: $\mathcal{U}$=50 m s^{-1}
0
10
20
30
40
time (hours)
c)
B96
d)
MG95: $\mathcal{U}$=50 m s^{-1}
volume (μm cm^{-3})
1.0
0.1
188
190
192
194
T [K]

Figure 4

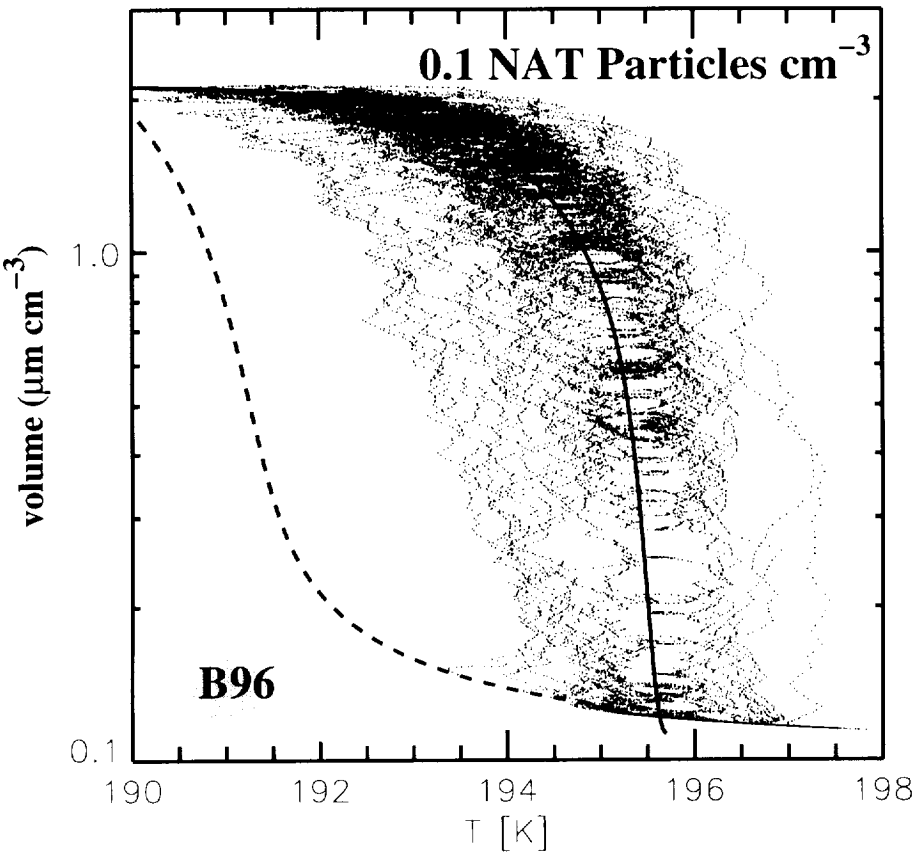
0.1 NAT Particles cm^{-3}
volume (μm cm^{-3})
1.0
0.1
B96
190
192
194
196
198
T [K]

Figure 5

Appendix C

Isentropic Advection by Gravity Waves: Quasi-universal M^{-3} Vertical Wavenumber Spectra near the Onset of Instability

Eckermann, S. D., *Geophys. Res. Lett.*, (in press), 1998.

GEOPHYSICAL RESEARCH LETTERS, VOL. 26, NO. 2, PAGES 201-204, JANUARY 15, 1999

Isentropic Advection by Gravity Waves: Quasi-Universal M^{-3} Vertical Wavenumber Spectra Near the Onset of Instability

Stephen D. Eckermann

Computational Physics, Inc., Fairfax, VA

Abstract. A two-dimensional model was used to advect air parcels under the influence of a linear superposition of hydrostatic gravity waves. As wave amplitudes increased, vertically profiled wave perturbations became nonsinusoidal, producing increased spectral power at large wavenumbers M. At saturation amplitudes just before onset of convective instabilities, these "tail spectra" assumed universal M^{-3} shapes, similar to observed spectra in the atmosphere and oceans.

Introduction

Autospectra of gravity-wave-induced horizontal velocity and relative temperature and density fluctuations have characteristic shapes in the atmosphere and oceans. In particular, vertical wavenumber spectra $F(M)$ have a quasi-universal M^{-3} form at large M [*Smith et al.*, 1987]. Many theories have been proposed to explain these observations. Here, we investigate a specific question of general relevance to all such theories: how do the vertically-profiled waveforms measured by these sounders relate to the wave-induced advection patterns that produced them?

For a single hydrostatic gravity wave, the answer is straightforward: the vertical profile has a sinusoidal form consistent with the advection field of the wave. This holds even for large-amplitude waves because wave displacements remain approximately transverse to the wavenumber vector $\vec{K}$. However, when a spectrum of J waves superpose, displacements can no longer be transverse to all wavenumber vectors $\vec{K}_j$ ($j = 1$–J) unless they are all parallel. For non-infinitessimal amplitudes, it is unclear how this will affect measured vertical perturbation profiles. We study this here using a simple kinematic model of wave advection.

Two-Dimensional Advection Model

A regular spatial grid (x_{i_x}, z_{i_z}) defines the unperturbed positions $(\bar{x}^P_{i_x}, \bar{z}^P_{i_z})$ of an array of air parcels P_{i_x,i_z}, where i_x and i_z are horizontal and vertical grid indices, such that

$$\bar{x}^P_{i_x} = x_{i_x} = x_0 + i_x \Delta x, \qquad i_x = 1, ..., I_x, \tag{1}$$

$$\bar{z}^P_{i_z} = z_{i_z} = z_0 + i_z \Delta z, \qquad i_z = 1, ..., I_z, \tag{2}$$

and $(\Delta x, \Delta z)$ is the spatial resolution. We assume a stably-stratified inviscid nonrotating background atmosphere of potential temperature $\bar{\Theta}(z)$ and no mean flow.

Paper number 1998GL900283.
0094-8276/99/1998GL900283$05.00

We perturb these parcels using a linear superposition of J nondissipating hydrostatic gravity waves, which yield parcel displacements of the form

$$\zeta'(x_{i_x}, z_{i_z}, t) = \sum_{j=1}^{J} \zeta'_j(x_{i_x}, z_{i_z}, t), \tag{3}$$

$$= \sum_{j=1}^{J} \hat{\zeta}_j \sin(k_j x_{i_x} + m_j z_{i_z} - \omega_j t + \phi_j),$$

$$\chi'(x_{i_x}, z_{i_z}, t) = \sum_{j=1}^{J} \left[\frac{-m_j}{k_j}\right] \zeta'_j(x_{i_x}, z_{i_z}, t). \tag{4}$$

The subscript j denotes the jth. wave, $\hat{\zeta}_j$ is it's peak vertical displacement amplitude, $\vec{K}_j = (k_j, 0, m_j)$ is it's wavenumber vector, ω_j is it's oscillation frequency, and ϕ_j is phase. Horizontal displacements (4) follow from (3) using polarization relations [*Gossard and Hooke*, 1975]. At time t the array of parcels P_{i_x,i_z} are advected to perturbed positions

$$\tilde{x}^P_{i_x,i_z}(t) = x_{i_x} + \chi'(x_{i_x}, z_{i_z}, t), \tag{5}$$

$$\tilde{z}^P_{i_x,i_z}(t) = z_{i_z} + \zeta'(x_{i_x}, z_{i_z}, t), \tag{6}$$

yielding an irregularly gridded wave displacement field

$$\chi'^P\left(\tilde{x}^P_{i_x,i_z}(t), \tilde{z}^P_{i_x,i_z}(t), t\right) = \chi'(x_{i_x}, z_{i_z}, t), \tag{7}$$

$$\zeta'^P\left(\tilde{x}^P_{i_x,i_z}(t), \tilde{z}^P_{i_x,i_z}(t), t\right) = \zeta'(x_{i_x}, z_{i_z}, t). \tag{8}$$

We resample these displacement fields at the regular grid positions (x_{i_x}, z_{i_z}) using standard algorithms (Delaunay triangulation and interpolation). This yields the array of parcels $Q_{i_x,i_z}(t)$ that have been advected to these grid positions at time t, i.e.,

$$\tilde{x}^Q_{i_x,i_z}(t) = x_{i_x} = \bar{x}^Q_{i_x,i_z}(t) + \chi'\left(\bar{x}^Q_{i_x,i_z}(t), \bar{z}^Q_{i_x,i_z}(t), t\right), \tag{9}$$

$$\tilde{z}^Q_{i_x,i_z}(t) = z_{i_z} = \bar{z}^Q_{i_x,i_z}(t) + \zeta'\left(\bar{x}^Q_{i_x,i_z}(t), \bar{z}^Q_{i_x,i_z}(t), t\right). \tag{10}$$

The wave displacement fields at these positions are

$$\chi'^Q(x_{i_x}, z_{i_z}, t) = \chi'\left(\bar{x}^Q_{i_x,i_z}(t), \bar{z}^Q_{i_x,i_z}(t), t\right), \tag{11}$$

$$\zeta'^Q(x_{i_x}, z_{i_z}, t) = \zeta'\left(\bar{x}^Q_{i_x,i_z}(t), \bar{z}^Q_{i_x,i_z}(t), t\right). \tag{12}$$

Thus, on the regular grid (x_{i_x}, z_{i_z}), $\zeta'(x_{i_x}, z_{i_z}, t)$ in (3) defines the Lagrangian vertical displacements of the parcels P_{i_x,i_z} *from* their equilibrium positions (x_{i_x}, z_{i_z}), whereas $\zeta'^Q(x_{i_x}, z_{i_z}, t)$ in (12) defines the Eulerian vertical displacement field due to parcels $Q_{i_x,i_z}(t)$ that have been instantaneously advected *to* positions (x_{i_x}, z_{i_z}) at time t. It is these

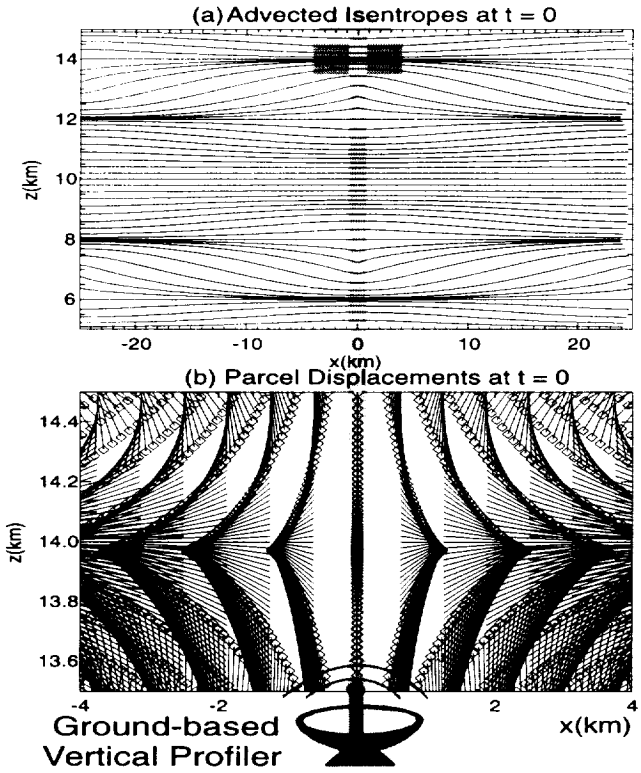

Figure 1. (a) Wave-perturbed isentropes. Shaded region at $z = 13.5$–14.5 km is expanded in (b), showing advected parcels P_{i_x,i_z} (diamonds) and lines connecting them to their undisturbed positions (x_{i_x}, z_{i_z}). Vertical arrow depicts the "beam" of a ground-based sounder at $x = 0$.

latter parcels that are sampled by a ground-based profiler: e.g., a vertical profiler at $x = x_{i_x}$ will measure the vertical displacement profile

$$Z'^{Q}(z,t) = \zeta'^{Q}(x_{i_x}, z, t). \tag{13}$$

The waves also advect potential temperature surfaces. This yields a perturbation potential temperature field

$$\frac{\Theta'^{Q}(z,t)}{\bar{\Theta}(z)} \approx \frac{-\bar{N}^2(z)}{g} Z'^{Q}(z,t), \tag{14}$$

where $\bar{N}^2(z)$ is the squared background Brunt-Väisälä frequency [*Eckermann et al.*, 1998]. Similar fractional relations govern the perturbed temperature and density fields.

Model Results

Using this model we studied vertical displacement profiles $Z'^{Q}(z,t_0) = \zeta'^{Q}(x_{i_x}, z, t_0)$, as would be sampled at some time t_0 by a ground-based vertical profiler at $x = x_{i_x}$. We compared $Z'^{Q}(z,t_0)$ with the corresponding Lagrangian perturbation profile $Z'(z,t) = \zeta'(x_{i_x}, z, t_0)$. Many different model simulations were conducted using a variety of choices for J, m_j, k_j, $\hat{\zeta}_j$ and ϕ_j in (3) and (4), but always confining $|m_j|$ within some range m_f-m_C. The following general characteristics were noted.

The power spectrum of $Z'(z,t_0)$, $F_Z(M,t_0)$, was confined within the wavenumber range $M = m_f$-m_C, irrespective of the values of $\hat{\zeta}_j$, as expected from (3). For small $\hat{\zeta}_j$'s, $Z'^{Q}(z,t_0)$ and $Z'(z,t_0)$, and their corresponding power spectra $F_Z^Q(M,t_0)$ and $F_Z(M,t_0)$, were almost identical. However, as $\hat{\zeta}_j$'s increased in wave fields where $\vec{K}_j$ vectors were not all parallel, $Z'^{Q}(z,t_0)$ deviated more and more from $Z'(z,t_0)$ by developing nonsinusoidal waveform distortions. This led to significant leakage of spectral power in $F_Z^Q(M,t_0)$ to Fourier wavenumbers $M > m_C$. Eventually amplitudes became large enough to generate isentropic overturning in places, implying convective instability, turbulence and mixing. On approaching this limit, $F_Z^Q(M,t_0)$ attained a limiting M^{-3} shape at $M > m_C$.

We illustrate these general features here using a specific field of $J = 8$ waves with parameters

$$m_j = -a_j m_f, \quad a_j = 1,1,2,2,3,3,4,4, \tag{15}$$
$$k_j = b_j k_f, \quad b_j = 1,-1,1,-1,1,-1,1,-1, \tag{16}$$
$$\hat{\zeta}_j = \hat{\zeta}_f, \tag{17}$$
$$\phi_j = \pi,\pi,0,0,0,0,\pi,\pi, \tag{18}$$

and fundamental wavenumbers $m_f = 2\pi(10\text{ km})^{-1}$, $k_f = 2\pi(50\text{ km})^{-1}$. From (15), the largest vertical wavenumber $m_C = 4m_f$. An amplitude $\hat{\zeta}_f = 0.112$ km was used for each wave: values only slightly larger than this produced regions of convective instability. Figure 1a plots distorted isentropes in the model at $t = 0$, using $I_x = 80$, $I_z = 1000$, $\Delta x = 0.625$ km and $\Delta z = 0.02$ km. Advected parcels P_{i_x,i_z} within a small region centered at $x = 0$ and $z = 14$ km are shown in Figure 1b. The observational "beam" of a profiler at $x = 0$ ($i_x = 40$) is also shown.

Figure 2a shows $Z'(z,t_0)$ and $Z'^{Q}(z,t_0)$ profiles at $x_{40} = 0$ and $t_0 = 0$. We see a nonsinusoidal distortion of $Z'^{Q}(z,t_0)$ compared to the sinusoidal $Z'(z,t_0)$ profile. Spectra (Figure 2b) show that the distortions produce an M^{-3} spectrum at $M > m_C$ extending over more than a decade in M.

The wave field (15)–(18) produces a horizontal standing wave pattern. At $t_0 = 0$, $\tilde{x}^P_{40,i_z}(t_0) = x_{40} = 0$ since χ'_j oscillations interfere destructively here (see Figure 1b). Conversely, ζ'_j oscillations interfere constructively here, which yields a one-dimensional (1D) profile solution at x_{40} given from (5), (6) and (8) by

$$\zeta'^{P}\left(x_{40}, z + \zeta'(x_{40},z,t_0), t_0\right) = \zeta'(x_{40},z,t_0), \tag{19}$$

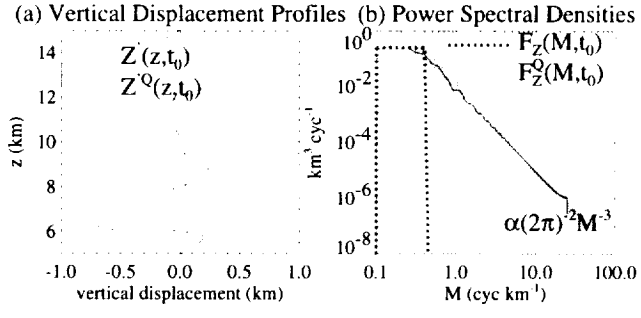

Figure 2. (a) $Z'(z,t_0)$ (dotted curve) and $Z'^{Q}(z,t_0)$ (solid curve) from model results in Figure 1 at $x_{40} = 0$ and $t_0 = 0$; (b) $F_Z(M,t_0)$ (dotted curve) and $F_Z^Q(M,t_0)$ (solid curve). Model spectrum (23) is also plotted (thick light curve) using $\alpha = 0.4$.

where $\zeta'(x_{40}, z, t_0) = Z'(z, t_0)$. Regridding the advection profile $\zeta'^P\left(x_{40}, z + \zeta'(x_{40}, z, t_0), t_0\right)$ onto the regular vertical grid z_{i_z} yields the $Z'^Q(z, t_0)$ profile. We see from (19) that the nonsinusoidal "steepening" of this $Z'^Q(z, t_0)$ oscillation (Figure 2a) is caused by differential vertical advection of points on the original profile $Z'(z, t_0)$ (Figure 1b), which yields a characteristic longitudinal distortion or "self advection" of the waveform. Note from Figure 1b, however, that both horizontal and vertical parcel displacements are important in producing distorted $Z'^Q(z, t)$ waveforms at other x_{i_x}'s in the model, and for wave fields different to (15)–(18).

Since the m_j's are constant and have magnitudes $\leq m_C$, no identifiable waves exist in the $F_Z^Q(M, t_0)$ "tail spectrum" at $M > m_C$ in Figure 2b. Indeed, on comparing $Z'^Q(z, t_0)$ and $Z'(z, t_0)$ in Figure 2a, we note that the wave *lengths* remain the same but the wave *shapes* differ. Thus, the M^{-3} spectrum in Figure 2b is essentially a Fourier effect, in which nonsinusoidal steepening of $Z'^Q(z, t_0)$ contributes a series of higher Fourier harmonics which asymptote to a characteristic M^{-3} spectrum as amplitudes increase towards a "saturation" value of $\hat{\zeta}_f \approx 0.112$ km.

To illustrate further features, we utilize the 1D solution (19) at x_{40}, since it is conceptually useful and can be gridded at a high vertical resolution. Here we use $I_z = 2\ 10^4$ and $\Delta z = \lambda_f / I_z$ for a given $m_f = 2\pi/\lambda_f$. Regridding is achieved here using cubic spline interpolation. A series of steepened wave forms similar in form to Figure 2a were created from (15)-(18) for arbitrary m_f by choosing

$$\hat{\zeta}_f = \epsilon_s \lambda_f = 4\epsilon_s \lambda_C, \tag{20}$$

where ϵ_s is a "saturation" constant for a given set of ϕ_j's.

For the phases (18), we obtained $\epsilon_s \approx 0.0115$ at this higher vertical resolution. Left panels of Figure 3 show

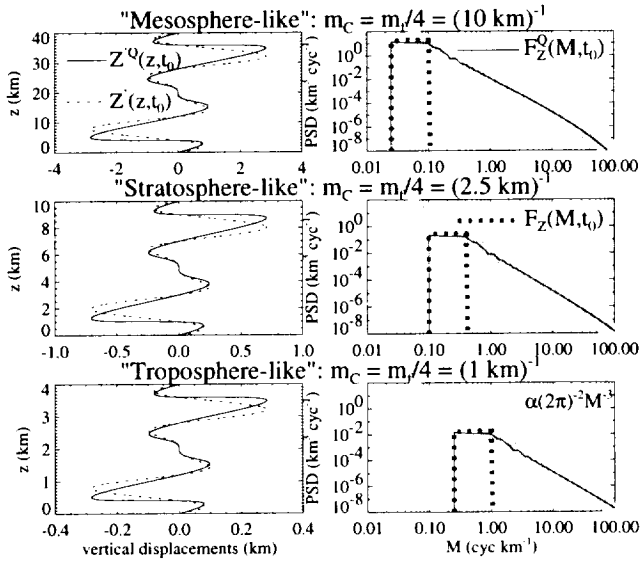

Figure 3. Left column: $Z'(z, t_0)$ (dotted curve) and $Z'^Q(z, t_0)$ (solid curve) from (20) at $x_{40} = 0$. Right column: spectra $F_Z(M, t_0)$ (dotted curve) and $F_Z^Q(M, t_0)$ (solid curve). Model spectrum (23) is also shown using $\alpha = 0.4$. Results are for three $m_C = m_f/4$ values: $(10\text{ km})^{-1}$ (top row); $(2.5\text{ km})^{-1}$ (middle); $(1\text{ km})^{-1}$ (bottom).

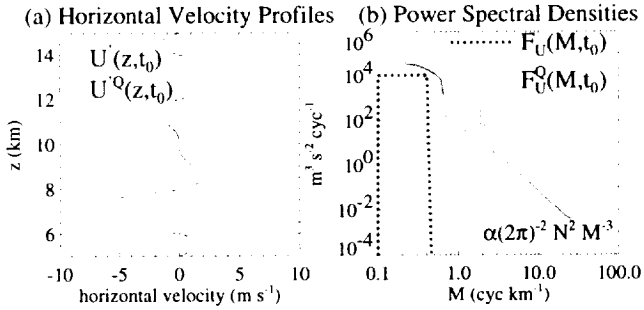

Figure 4. As in Figure 2, but for horizontal velocity perturbations at $i_x = 555$ ($x = 2.75$ km). Model "saturated" spectrum also plotted using $\alpha = 0.1$.

$Z'^Q(z, t_0)$ and $Z'(z, t_0)$ profiles at $t_0 = 0$ using three m_f values: $2\pi(40\text{ km})^{-1}$ (top row); $2\pi(10\text{ km})^{-1}$ (middle row); $m_f = 2\pi(4\text{ km})^{-1}$ (bottom row). Corresponding spectra are shown to the right. $F_Z^Q(M, t_0)$ spectra at $M > m_C = 4m_f$ not only have M^{-3} shapes (extending over more than two decades in M), but their intensities are nearly identical in each case, despite the different m_f and $\hat{\zeta}_f$ values used.

Existing spectral models (based to some extent on collated observations) yield "saturated" spectra of relative potential temperature perturbations at large M of the form

$$F^{sat}_{(\Theta'/\bar{\Theta})}(M) = \alpha \left(\frac{\bar{N}^4}{g^2}\right) M^{-3}, \tag{21}$$

where α is a universal constant, typically in the range ~ 0.1-0.5 depending on the model used [*Smith et al.*, 1987; *Hines*, 1991; *Gardner*, 1996]. From (14), this implies a saturated spectrum of hydrostatic vertical displacements

$$F_Z^{sat}(M) = \alpha M^{-3}, \tag{22}$$

for M in units of rad m^{-1}: for units of cyc m^{-1}, an additional factor $(2\pi)^{-2}$ appears on the right of (22). This spectrum is plotted in Figures 2b and 3 using a "best fit" $\alpha \approx 0.4$ that closely matches both the shape and intensity of the various $F_Z^Q(M, t_0)$ tail spectra. Thus, even when m_f and m_C vary, the advectively-generated $F_Z^Q(M, t_0)$ tail spectra at $M > m_C$ always converge to the "universal" M^{-3} spectrum observed in the atmosphere [*Smith et al.*, 1987]. The "best fit" α value varied somewhat from simulation to simulation: e.g., adding $\pi/2$ to all phases in (18) yielded $\epsilon_s \approx 0.0102$ and $F_Z^Q(M, t_0)$ spectra at $M > m_c$ with a "best fit" $\alpha \sim 0.2$.

For a single hydrostatic wave, $\hat{u}_j = -\imath \bar{N} \delta_j \hat{\zeta}_j$, where $\hat{u}_j$ is the peak horizontal velocity amplitude and $\delta_j = \pm 1$, depending on the sign of m_j/k_j (assuming $\omega_j > 0$) [*Gossard and Hooke*, 1975]. Combining this with (3) yields the horizontal velocity field

$$u'(x_{i_x}, z_{i_z}, t) = \bar{N} \sum_{j=1}^{J} \delta_j \hat{\zeta}_j \cos(k_j x_{i_x} + m_j z_{i_z} - \omega_j t + \phi_j), \tag{23}$$

which leads in the same way as before to $U'(z, t_0)$ and $U'^Q(z, t_0)$ profiles at a given x_{i_x}. The waves (15)-(18) yield a vanishing $U'^Q(z, t_0)$ profile at $x_{40} = 0$, so we consider

profiles at other locations where both horizontal and vertical displacements will be significant (Figure 1b). Therefore a high horizontal resolution is used here ($I_x = 1000$, $\Delta x = 50$ m).

Model-generated profiles at $i_x = 555$ ($x_{i_x} = 2.75$ km) are shown in Figure 4a using $\bar{N} = 0.02$ rad s^{-1}. Profile distortions are different here: whereas $Z'^{Q}(z, t_0)$ steepened near the nodes of the oscillation (Figures 2a and 3), $U'^{Q}(z, t_0)$ departs from sinusoidality mainly around the peaks and troughs of the waveform. This is due to the $\pm 90°$ phase shift between $\hat{u}_j$ and $\hat{\zeta}_j$ for each wave. Peak amplitudes of the profiles in Figure 4a also differ, due to nonzero horizontal parcel displacements that arise here. Spectra in Figure 4b show formation of $F_U^Q(M, t_0)$ "tail spectra" $\sim M^{-3}$ at $M > m_C$. Using (22) and (23), the corresponding "saturated" horizontal velocity spectrum is $\approx \alpha \bar{N}^2 M^{-3}$ [*Smith et al.*, 1987] and is plotted in Figure 4b using a nominal $\alpha \approx 0.1$. Intensities of $F_U^Q(M, t_0)$ tail spectra are somewhat less than model predictions.

Discussion

A simple "Occam's Razor" model reveals that the purely kinematic effects of a linear superposition of gravity waves can generate vertical wavenumber spectra similar to observations. Simulated vertical displacement/potential temperature spectra attained limiting quasi-universal M^{-3} forms at large M that closely resemble observed spectra. Horizontal velocities also had M^{-3} shapes, but spectral intensities here were generally smaller than observed. A range of omitted effects (e.g., rotation, three-dimensionality, dynamical nonlinearities, refraction, different k_j's, spectral averaging etc.) may account for some of these discrepansies.

Hines [1991, 1993, 1996] argued that advective nonlinearities are important for atmospheric gravity wave spectra, citing as evidence the *Allen and Joseph* [1989] (AJ89) model of oceanic gravity waves. The AJ89 model produces M^{-3} spectra beyond some cutoff wavenumber m_C. The present simulations, while highly idealized, have features which resemble the AJ89 analysis: e.g., linear superposition of Lagrangian wave displacements, inclusion of advection effects, computation of both Eulerian and Lagrangian spectra, and M^{-3} "tail spectra" beyond a cutoff wavenumber m_C. *Hines* [1991, 1993] argues that Doppler-spread theory (DST) models these processes too [*Hines*, 1996; *Chunchuzov*, 1996], though other studies have questioned this [*Eckermann*, 1997; *Broutman et al.*, 1997].

Quasi-universal M^{-3} spectra arose here due to a limiting "saturation" constant ϵ_s in (20) for a given set of waves. A similar saturation constant marks the onset of convective overturning for a single hydrostatic wave of wavenumber m_C and amplitude ζ_f,

$$\hat{\zeta}_f = m_C^{-1} = (2\pi)^{-1} \lambda_C. \tag{24}$$

This yields $\hat{\zeta}_f / \lambda_C \approx 0.16$, whereas from (20) $\hat{\zeta}_f / \lambda_C = 4\epsilon_s \approx 0.05$ for the simulations here ($\epsilon_s \approx 0.0115$). The smaller latter ratio indicates that instabilities due to superposition set in first here. From (3) and (20), the total variance

$$\overline{\zeta'^2} = \frac{J}{2} \hat{\zeta}_f^2 = \frac{a^2}{m_C^2}, \tag{25}$$

where $a = (16\pi\epsilon_s) \approx 0.6$ for the waves (15)-(18). In an isothermal unsheared atmosphere, $\overline{U'^2} = \bar{N}^2 \overline{\zeta'^2}$ grows with height as $\exp(z/H_\rho)$, where H_ρ is density scale height. From (25), m_C must decrease exponentially with height with a scale height $2H_\rho$ to retain the same marginally stable profiles in Figure 3. In practice, wave fields will not scale with height in this manner. Rather, as m_C decreases with height, those waves of $|m_j| \sim m_C$ will be progressively removed or attenuated [*Hines*, 1993; *Gardner*, 1996; *Eckermann*, 1997], yielding a more gradual increase (decrease) in variance (m_C) with height [*Hines*, 1996].

The $Z'^{Q}(z, t_0)$ profile in Figure 2a implies large narrowly-confined enhancements in static stability at ~6 and 14 km. These features resemble the narrow "sheets" observed in high resolution stratospheric temperature profiles [*Dalaudier et al.*, 1994]. Turbulence often occurs near these layers, which also agrees with the current model, since they arise here only at amplitudes close to the onset of convective instability.

Acknowledgments. This research was partially supported by NASA contracts NAS5-97247 and NAS5-98045.

References

Allen, K. R., and R. I. Joseph, A canonical statistical theory of oceanic internal waves, *J. Fluid Mech.*, *204*, 185-228, 1989.

Broutman, D., C. Macaskill, M. E. McIntyre, and J. W. Rottman, On Doppler-spreading models of internal waves, *Geophys. Res. Lett.*, *24*, 2813-2816, 1997.

Chunchuzov, I. P., The spectrum of high-frequency internal waves in the atmospheric waveguide, *J. Atmos. Sci.*, *53*, 1798-1814, 1996.

Dalaudier, F., C. Sidi, M. Crochet, and J. Vernin, Direct evidence of "sheets" in the atmospheric temperature field, *J. Atmos. Sci.*, *51*, 237-248, 1994.

Eckermann, S. D., Influence of wave propagation on the Doppler spreading of atmospheric gravity waves, *J. Atmos. Sci.*, *54*, 2544-2573, 1997.

Eckermann, S. D., D. E. Gibson-Wilde, and J. T. Bacmeister, Gravity wave perturbations of minor constituents: a parcel advection methodology, *J. Atmos. Sci.*, (in press), 1998.

Gardner, C. S., Testing theories of atmospheric gravity wave saturation and dissipation, *J. Atmos. Terr. Phys.*, *58*, 1575-1589, 1996.

Gossard, E. E., and W. H. Hooke, *Waves in the atmosphere*, 456pp., Elsevier, Amsterdam, 1975.

Hines, C. O., The saturation of gravity waves in the middle atmosphere. Part II: Development of Doppler-spread theory, *J. Atmos. Sci.*, *48*, 1360-1379, 1991.

Hines, C. O., The saturation of gravity waves in the middle atmosphere. Part IV: Cutoff of the incident wave spectrum, *J. Atmos. Sci.*, *50*, 3045-3060, 1993.

Hines, C. O., Nonlinearity of gravity wave saturated spectra in the middle atmosphere, *Geophys. Res. Lett.*, *23*, 3309-3312, 1996.

Smith, S. A., D. C. Fritts and T. E. VanZandt, Evidence of a saturated spectrum of atmospheric gravity waves, *J. Atmos. Sci.*, *44*, 1404-1410, 1987.

S. D. Eckermann, Code 7641.2, Naval Research Laboratory, Washington, DC 20375 (email: eckerman@uap.nrl.navy.mil)

(Received January 21, 1998; revised November 13, 1998; accepted November 20, 1998.)

Appendix D

Full Page Figures

Plate 1

Figures 1,2,3,4,5,6,7,9,10,11,12

(note that Figures 8,13,14 and 15 are to be found in the main body of the text)

In situ Meteorological Measurements Made on the DC-8 During the SUCCESS Campaign

May 2, 1996

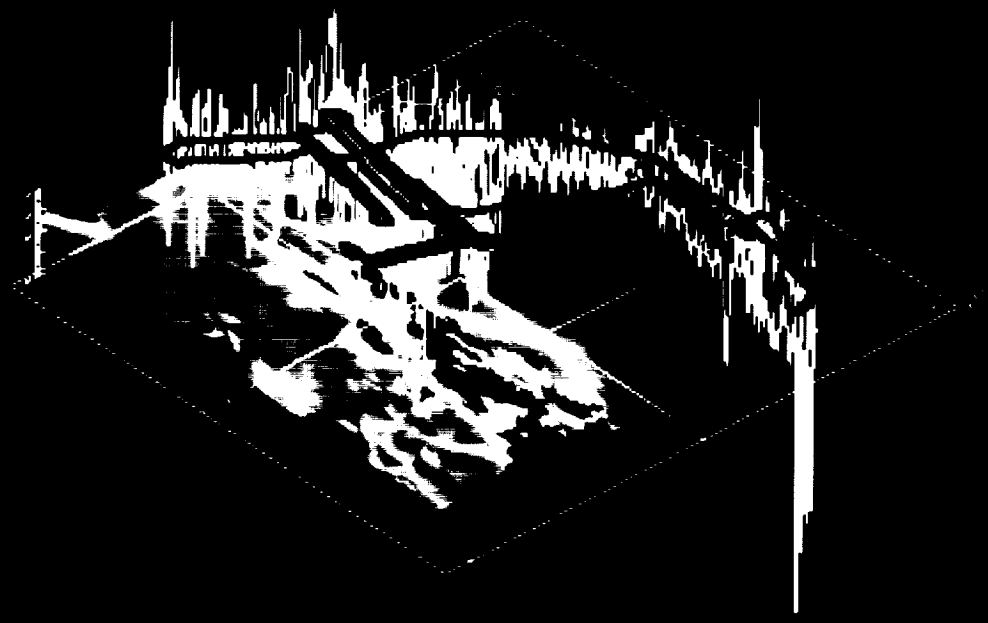

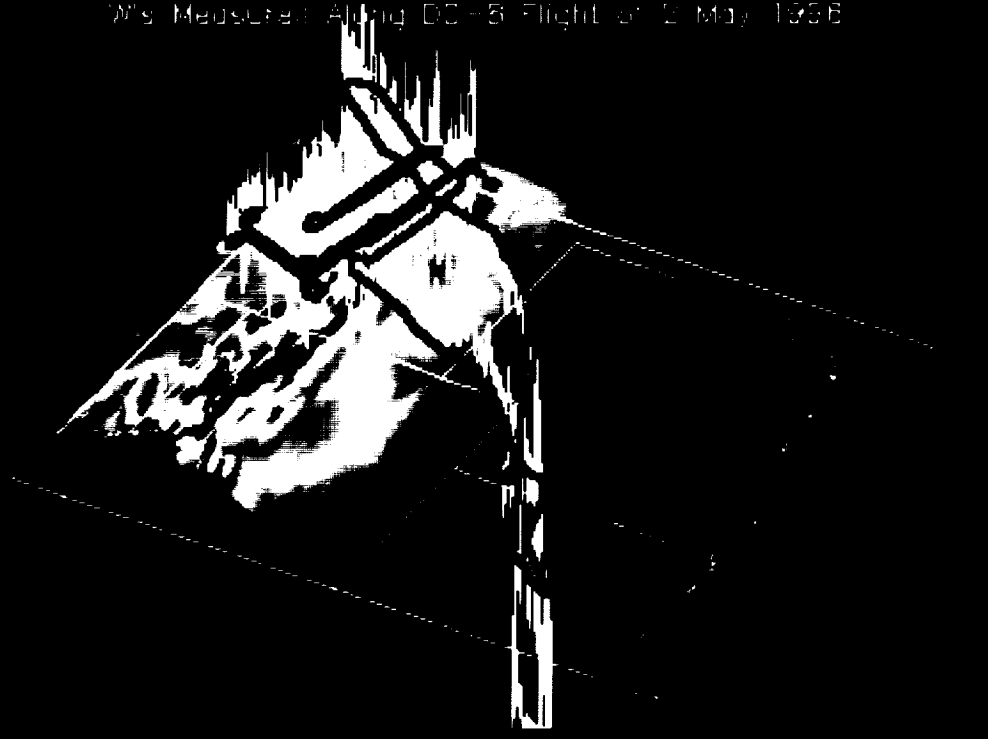

Plate 1

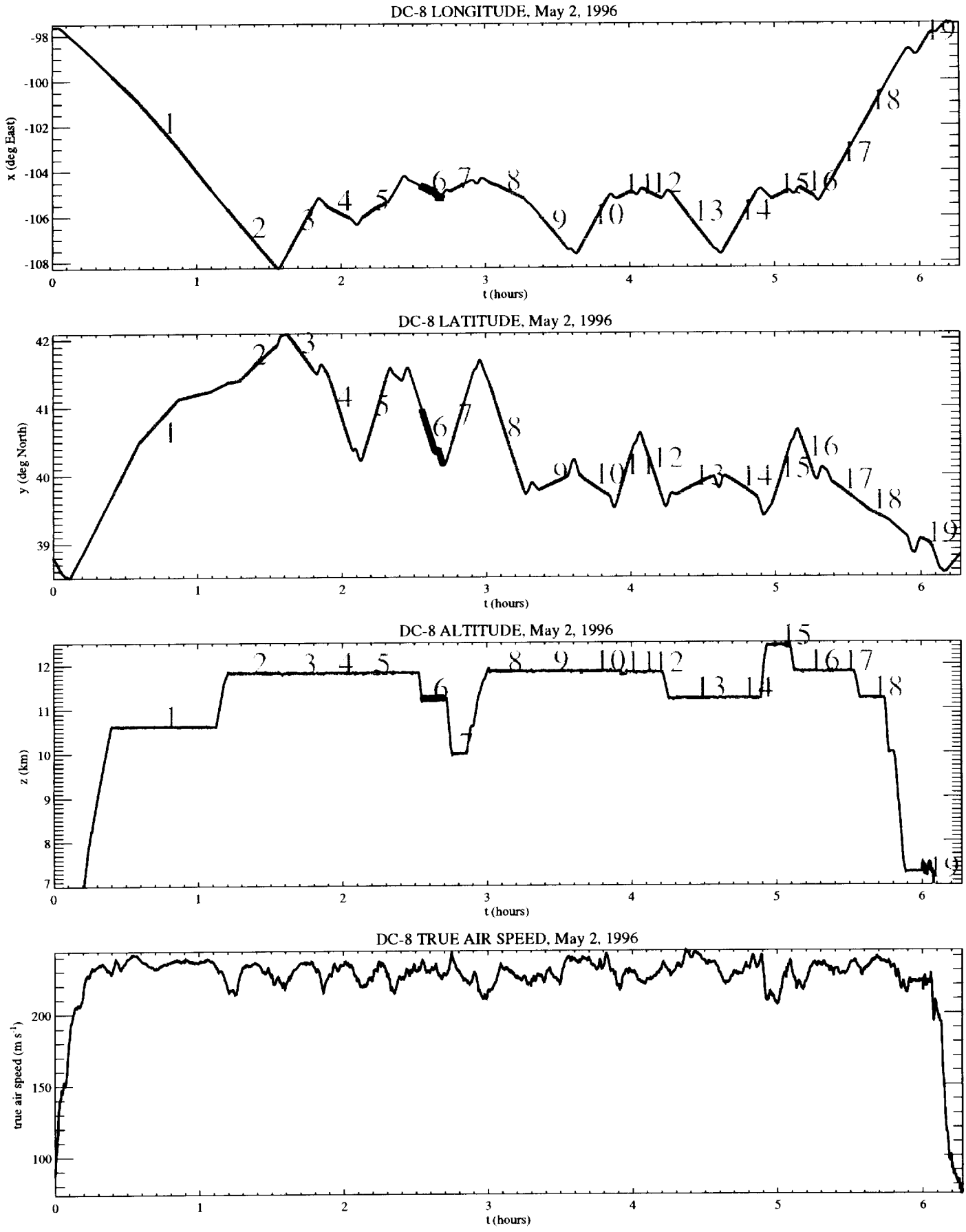
DC-8 LONGITUDE, May 2, 1996
x (deg East)
t (hours)
DC-8 LATITUDE, May 2, 1996
y (deg North)
t (hours)
DC-8 ALTITUDE, May 2, 1996
z (km)
t (hours)
DC-8 TRUE AIR SPEED, May 2, 1996
true air speed (m s-1)
t (hours)

Figure 1

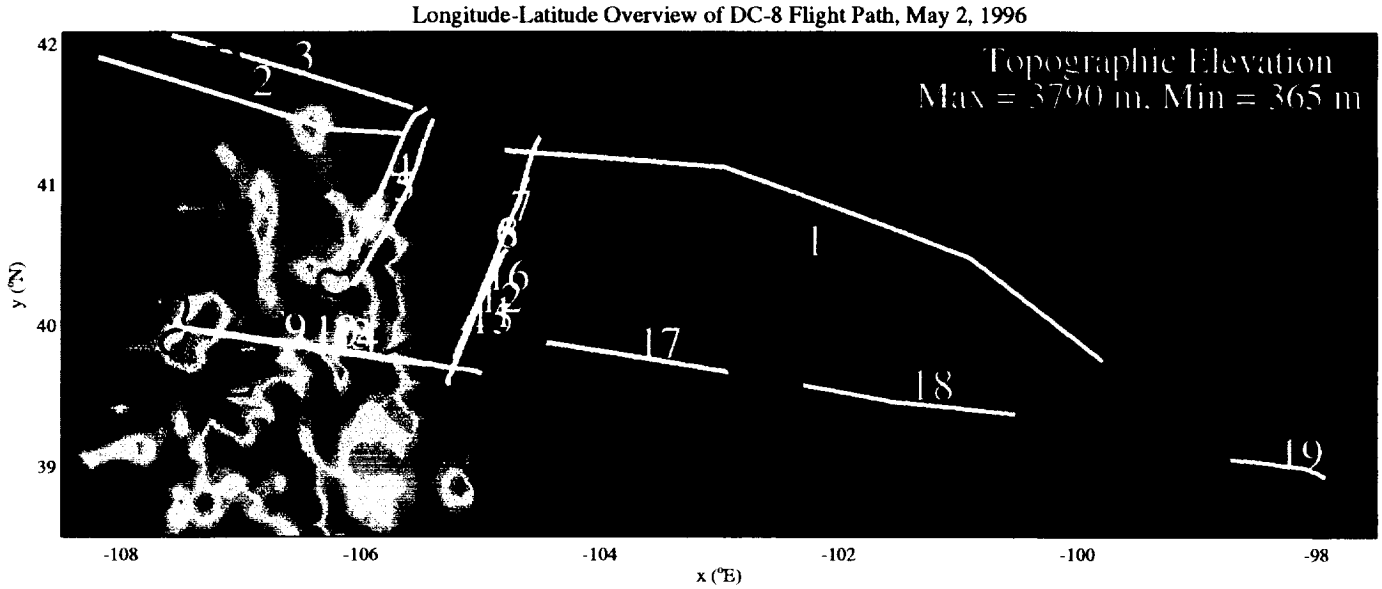
Longitude-Latitude Overview of DC-8 Flight Path, May 2, 1996
Topographic Elevation
Max = 3790 m, Min = 365 m
1
2
3
17
18
19
42
41
40
39
y (°N)
-108
-106
-104
-102
-100
-98
x (°E)

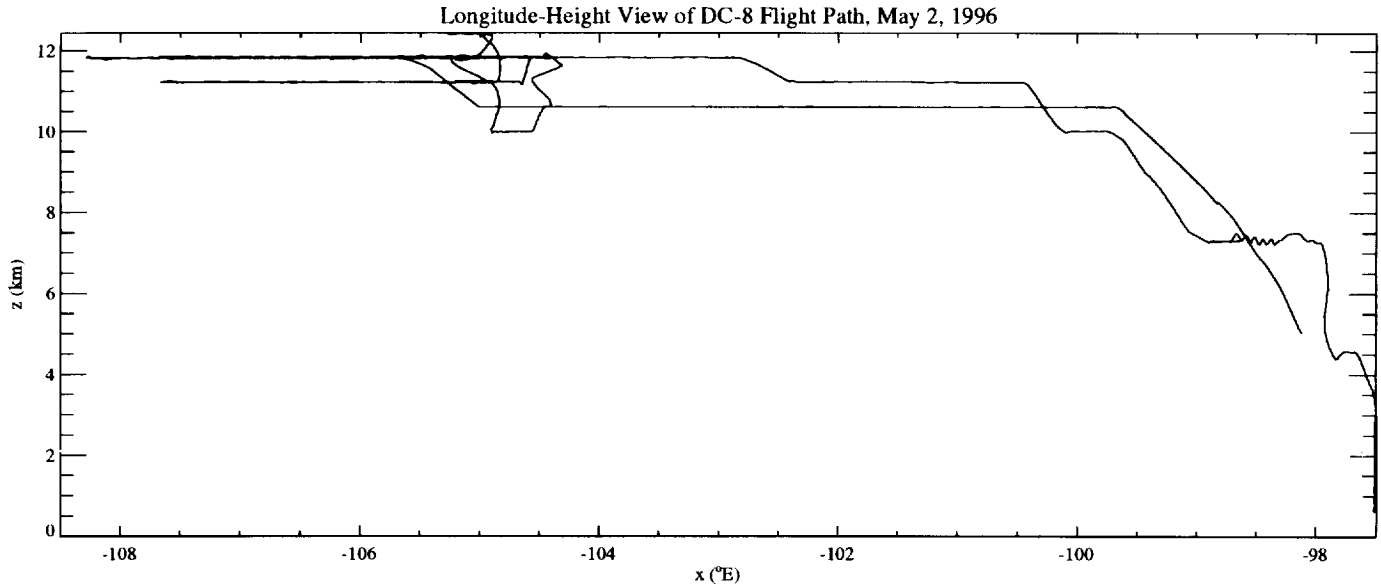
Longitude-Height View of DC-8 Flight Path, May 2, 1996
12
10
8
6
4
2
0
z (km)
-108
-106
-104
-102
-100
-98
x (°E)

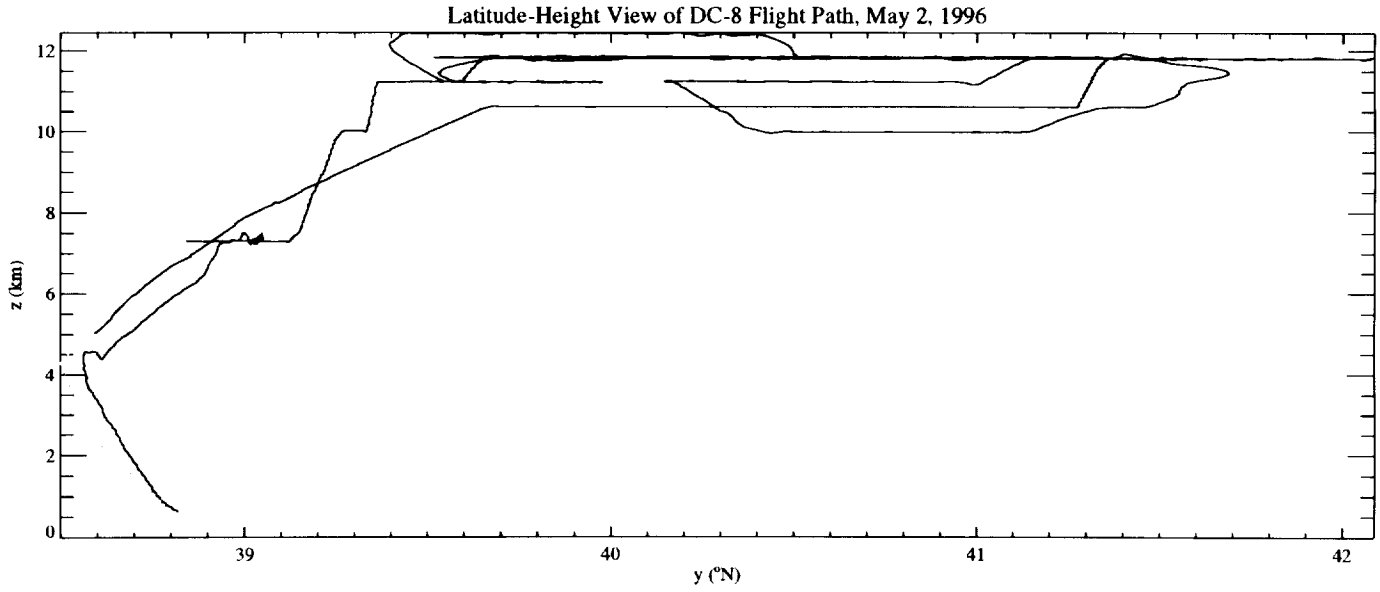
Latitude-Height View of DC-8 Flight Path, May 2, 1996
12
10
8
6
4
2
0
z (km)
39
40
41
42
y (°N)

Figure 2

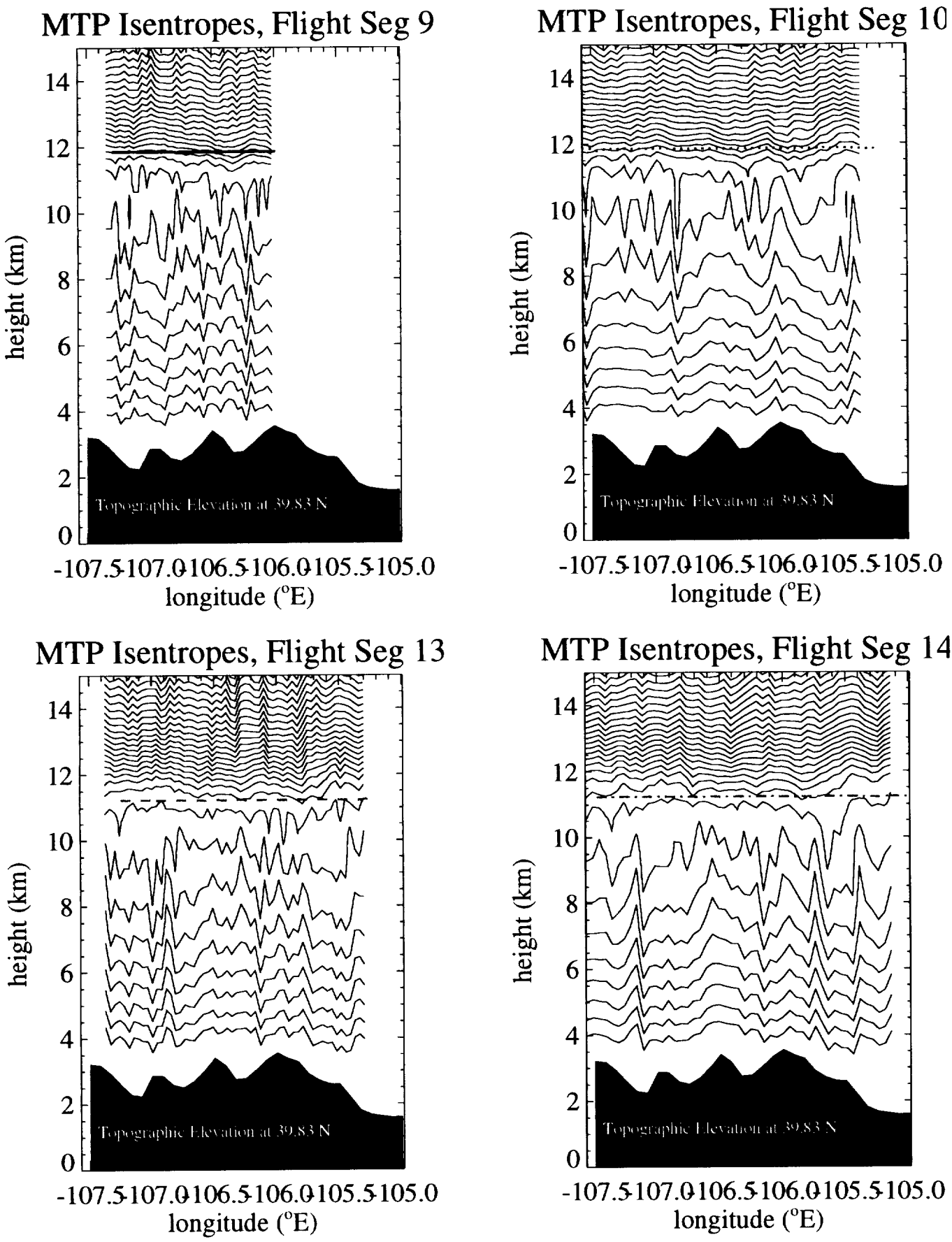
MTP Isentropes, Flight Seg 9
MTP Isentropes, Flight Seg 10
MTP Isentropes, Flight Seg 13
MTP Isentropes, Flight Seg 14
height (km)
0
2
4
6
8
10
12
14
Topographic Elevation at 39.83 N
-107.5 -107.0 -106.5 -106.0 -105.5 -105.0
longitude (°E)

Figure 3

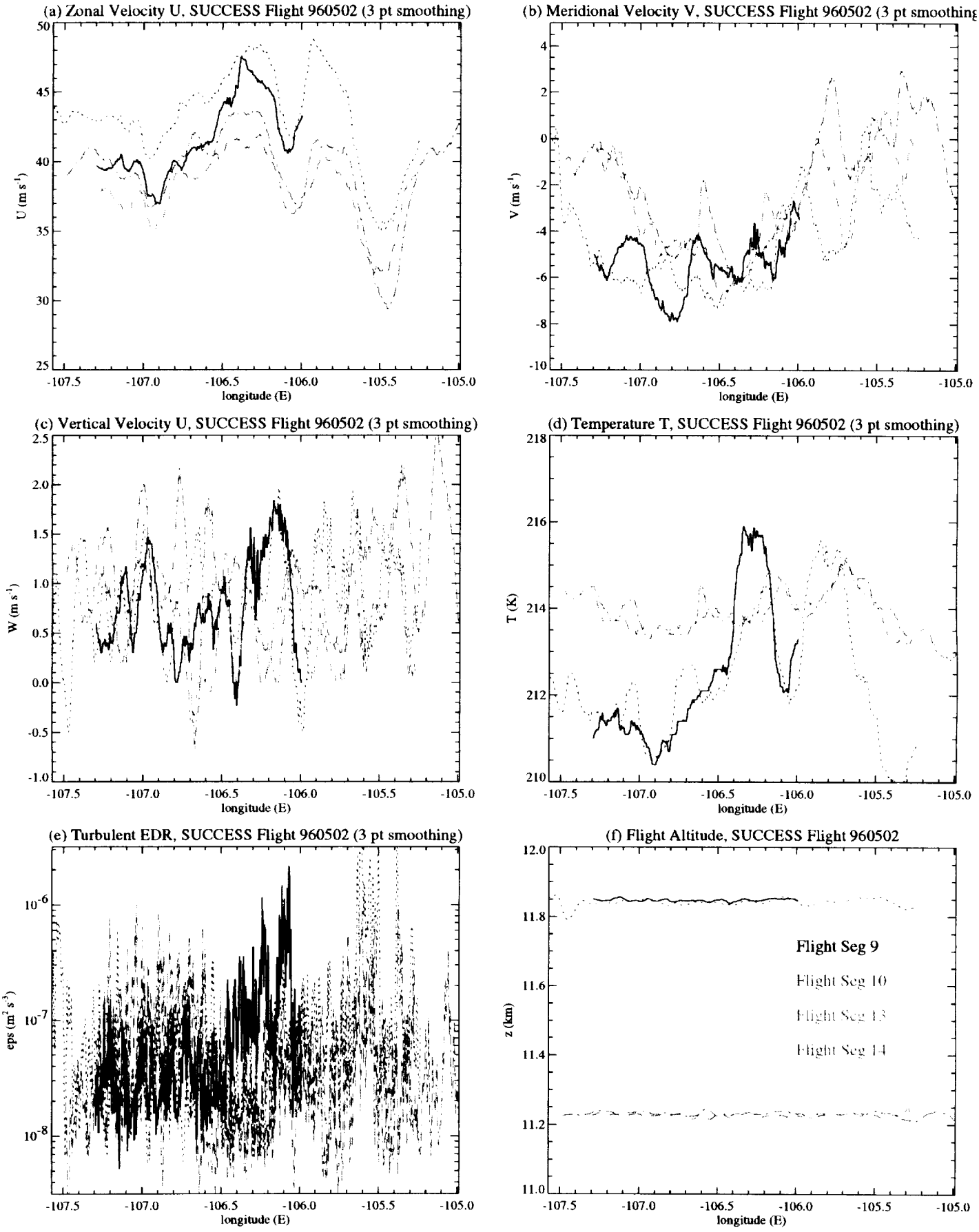
(a) Zonal Velocity U, SUCCESS Flight 960502 (3 pt smoothing)
U (m s-1)
longitude (E)
(b) Meridional Velocity V, SUCCESS Flight 960502 (3 pt smoothing
V (m s-1)
longitude (E)
(c) Vertical Velocity U, SUCCESS Flight 960502 (3 pt smoothing)
W (m s-1)
longitude (E)
(d) Temperature T, SUCCESS Flight 960502 (3 pt smoothing)
T (K)
longitude (E)
(e) Turbulent EDR, SUCCESS Flight 960502 (3 pt smoothing)
eps (m2 s-3)
longitude (E)
(f) Flight Altitude, SUCCESS Flight 960502
z (km)
Flight Seg 9
Flight Seg 10
Flight Seg 13
Flight Seg 14
longitude (E)

Figure 4

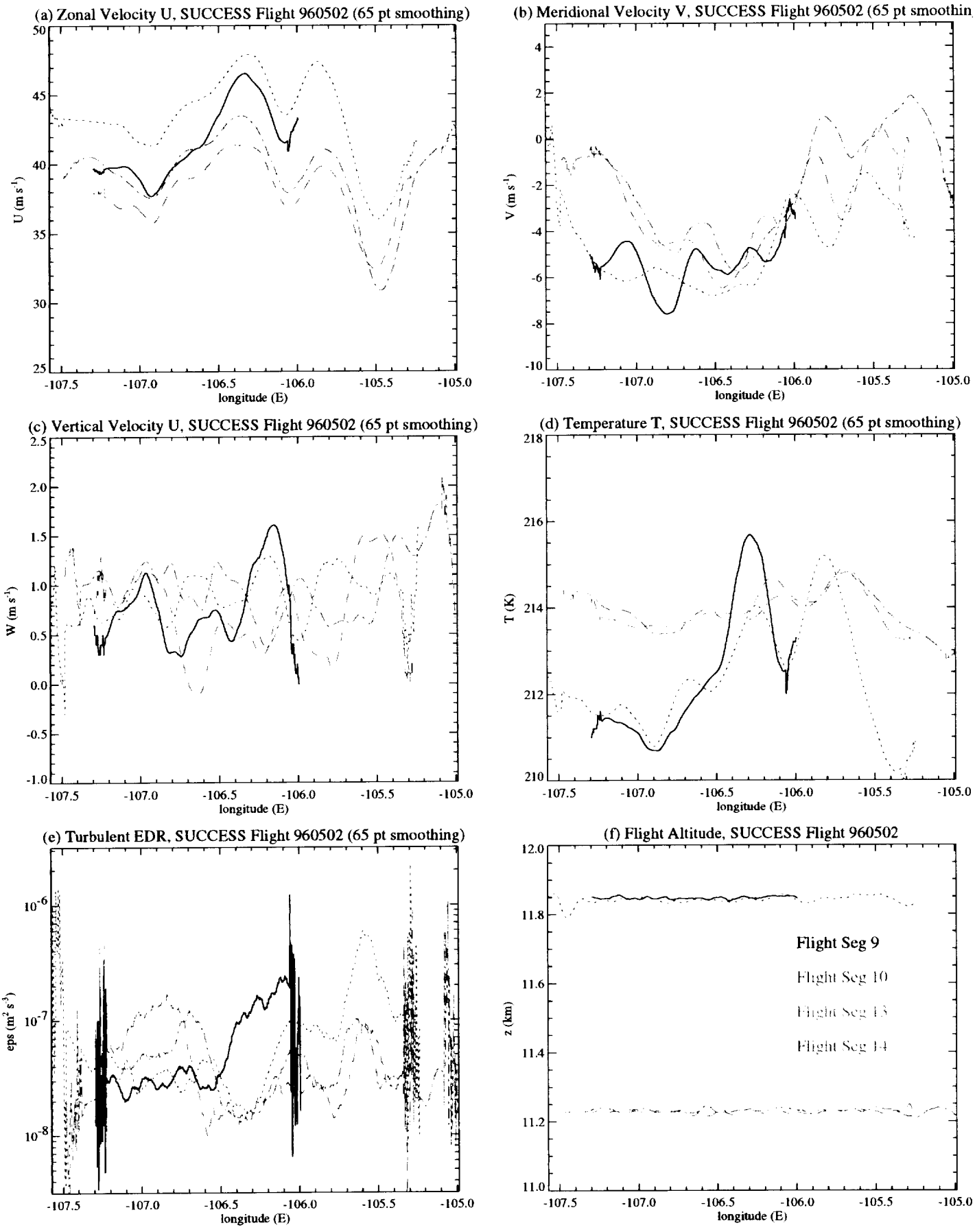
(a) Zonal Velocity U, SUCCESS Flight 960502 (65 pt smoothing)
U (m s-1)
longitude (E)
(b) Meridional Velocity V, SUCCESS Flight 960502 (65 pt smoothin
V (m s-1)
longitude (E)
(c) Vertical Velocity U, SUCCESS Flight 960502 (65 pt smoothing)
W (m s-1)
longitude (E)
(d) Temperature T, SUCCESS Flight 960502 (65 pt smoothing)
T (K)
longitude (E)
(e) Turbulent EDR, SUCCESS Flight 960502 (65 pt smoothing)
eps (m2 s-3)
longitude (E)
(f) Flight Altitude, SUCCESS Flight 960502
z (km)
Flight Seg 9
Flight Seg 10
Flight Seg 13
Flight Seg 14
longitude (E)

Figure 5

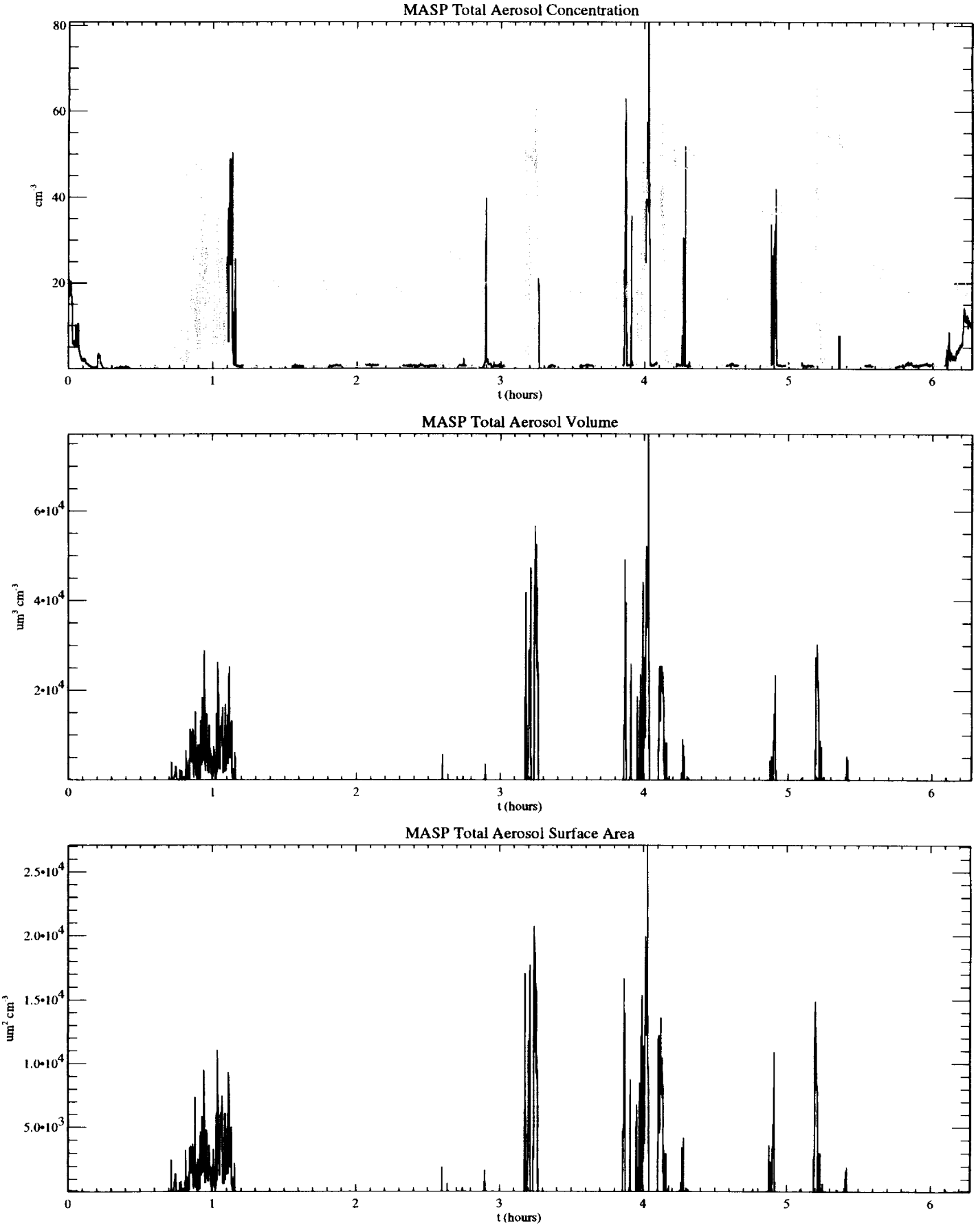
MASP Total Aerosol Concentration
80
60
40
20
cm^{-3}
0
1
2
3
4
5
6
t (hours)
MASP Total Aerosol Volume
6•10^4
4•10^4
2•10^4
um^3 cm^{-3}
0
1
2
3
4
5
6
t (hours)
MASP Total Aerosol Surface Area
2.5•10^4
2.0•10^4
1.5•10^4
1.0•10^4
5.0•10^3
um^2 cm^{-3}
0
1
2
3
4
5
6
t (hours)

Figure 6

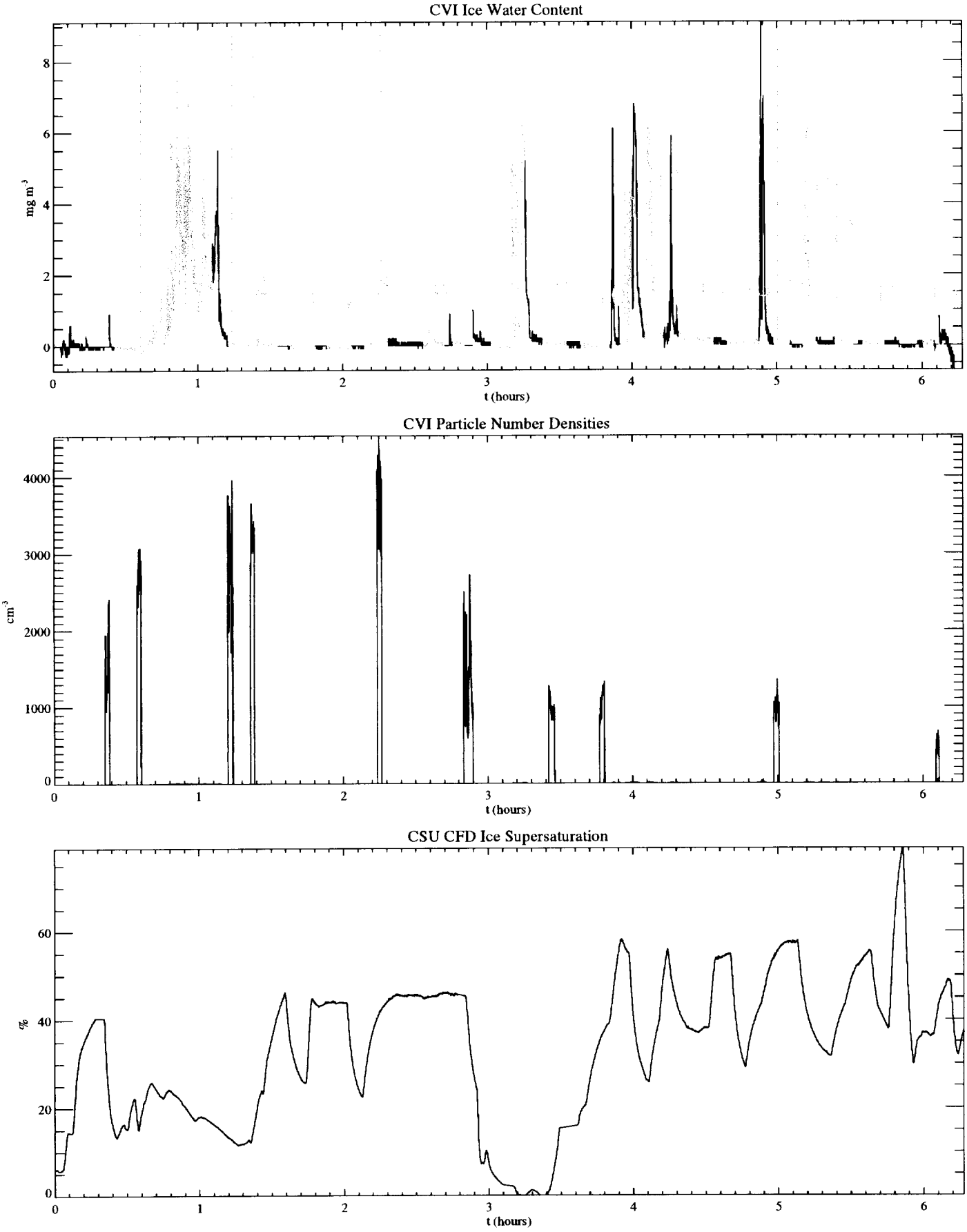
CVI Ice Water Content
mg m-3
t (hours)
CVI Particle Number Densities
cm-3
t (hours)
CSU CFD Ice Supersaturation
%
t (hours)

Figure 7

NRL/MWFM Predictions, 2nd May, 1996 (NCEP Data)

100mb

(a) Peak Vertical Displacement

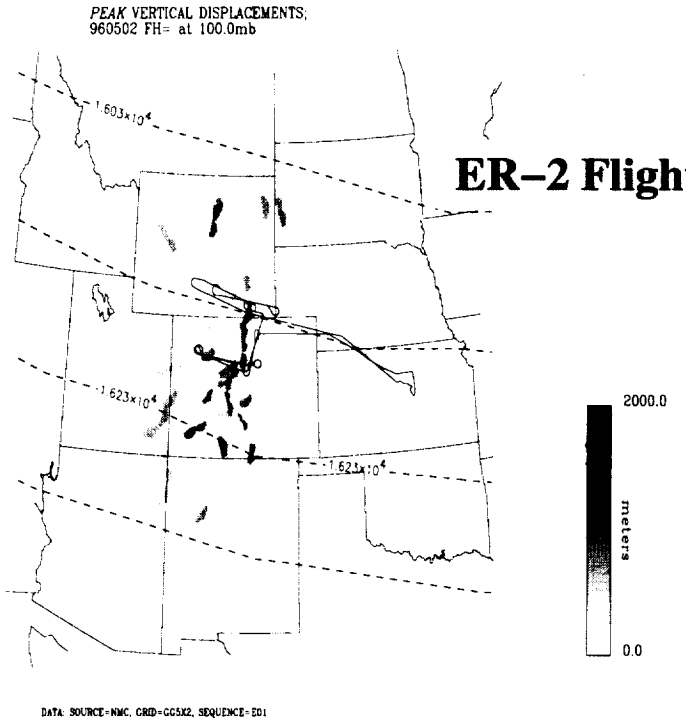

(b) Momentum Flux Divergence

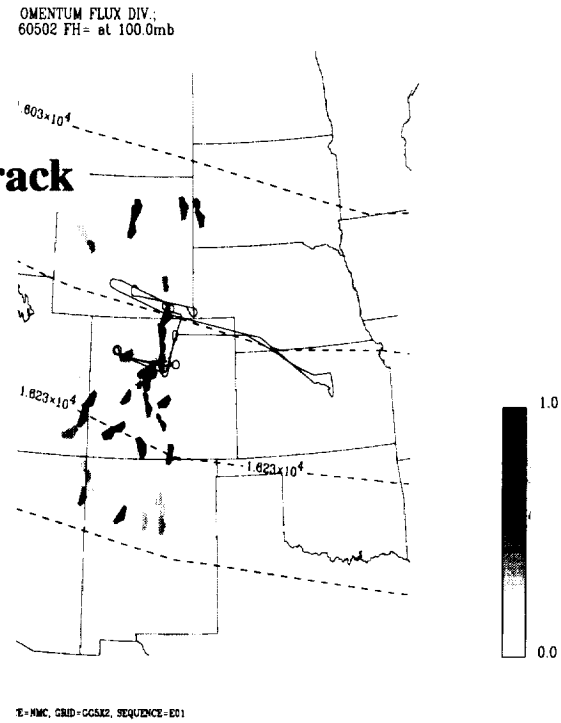

ER–2 Flight Track

200mb

(c) Peak Vertical Displacement

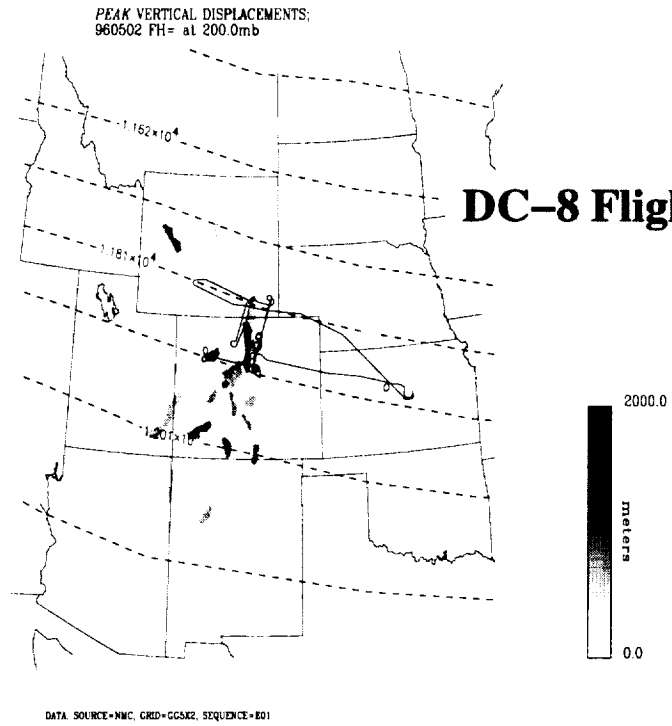

(d) Momentum Flux Divergence

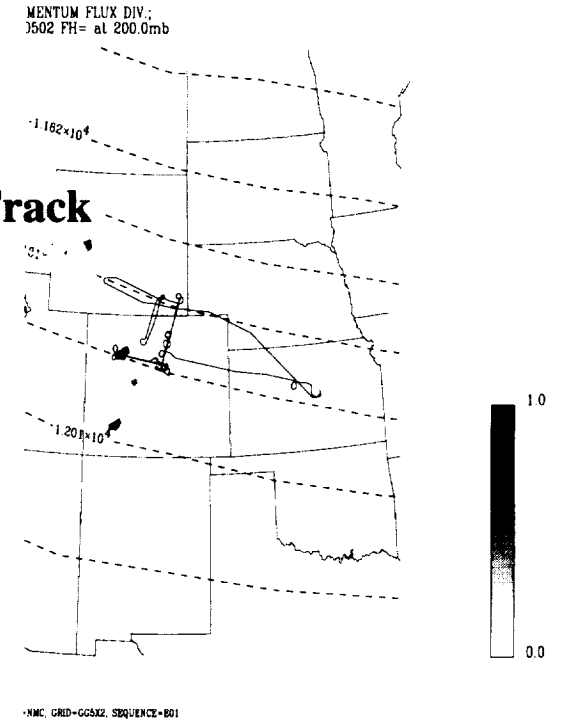

DC–8 Flight Track

Figure 9

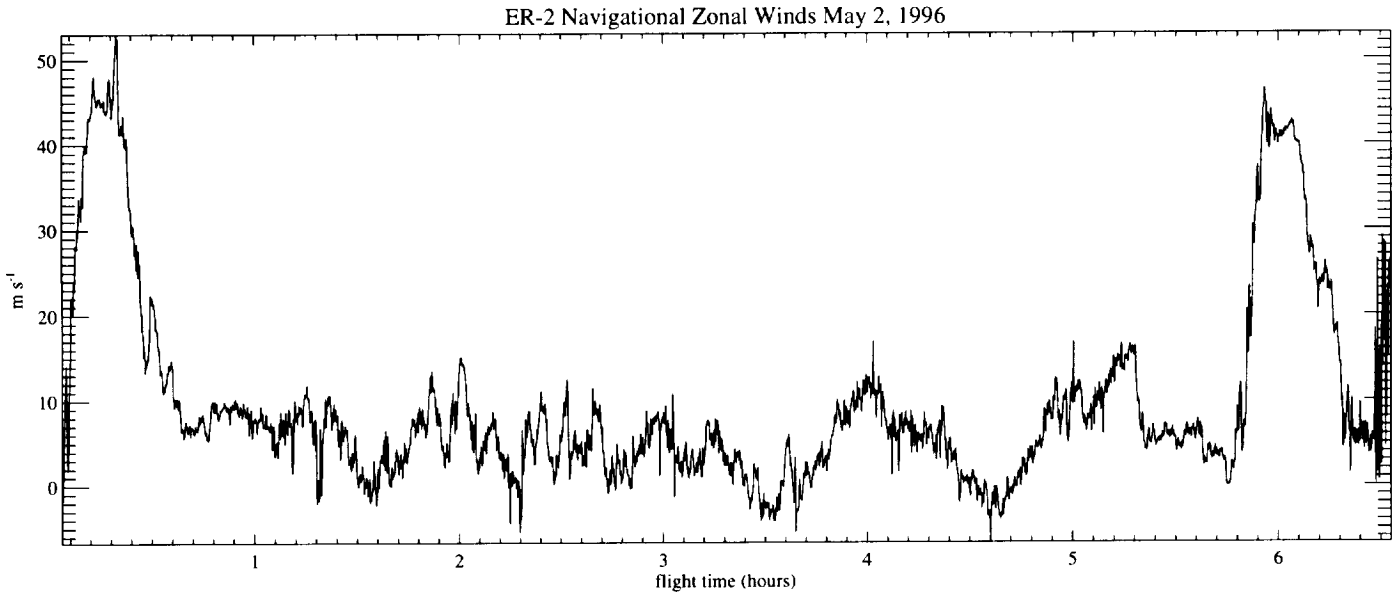
ER-2 Navigational Zonal Winds May 2, 1996
m s-1
50
40
30
20
10
0
1
2
3
4
5
6
flight time (hours)

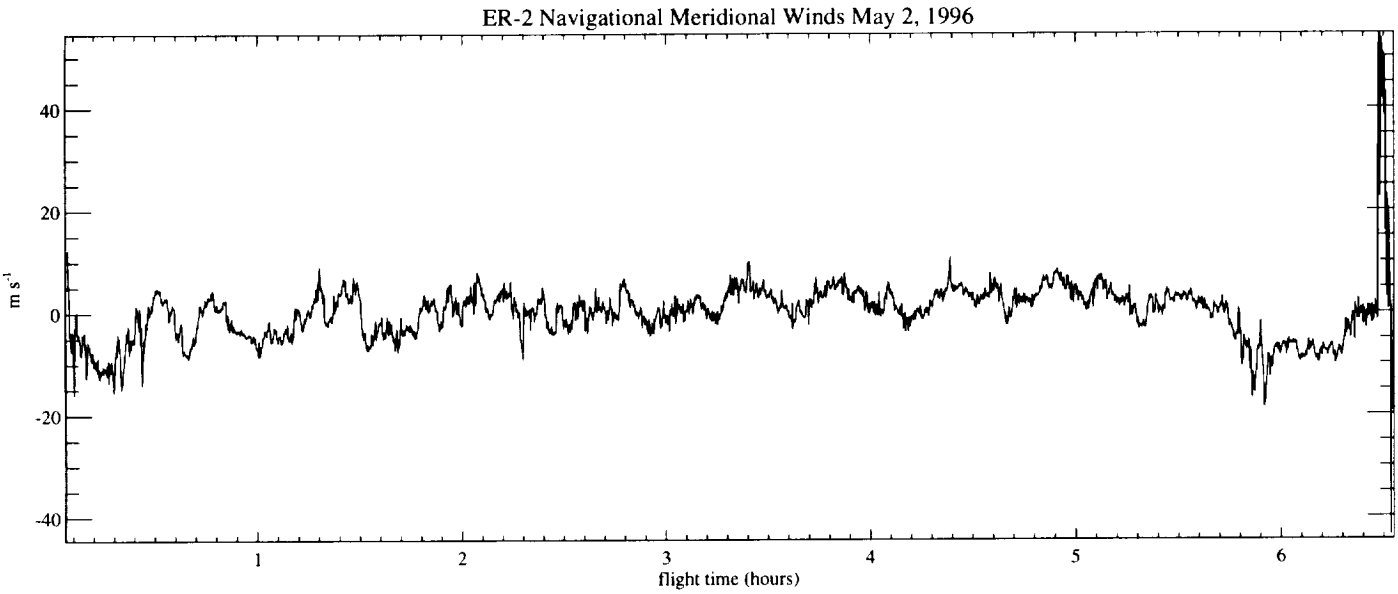
ER-2 Navigational Meridional Winds May 2, 1996
m s-1
40
20
0
-20
-40
1
2
3
4
5
6
flight time (hours)

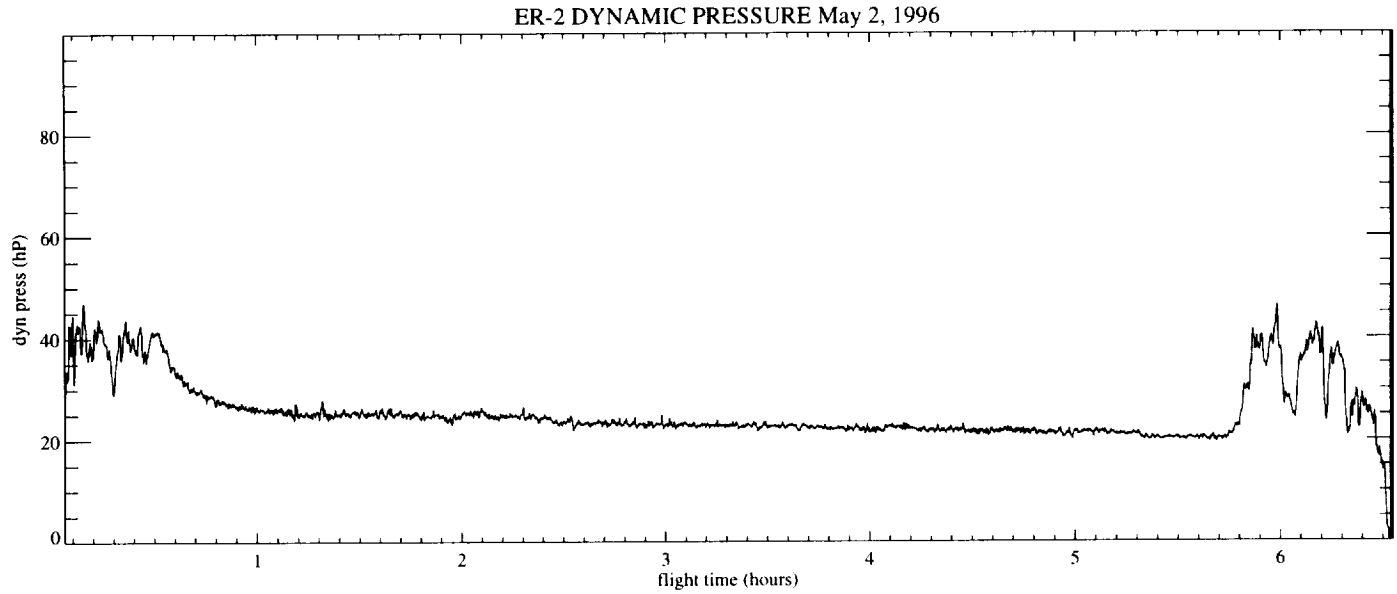
ER-2 DYNAMIC PRESSURE May 2, 1996
dyn press (hP)
80
60
40
20
0
1
2
3
4
5
6
flight time (hours)

Figure 10

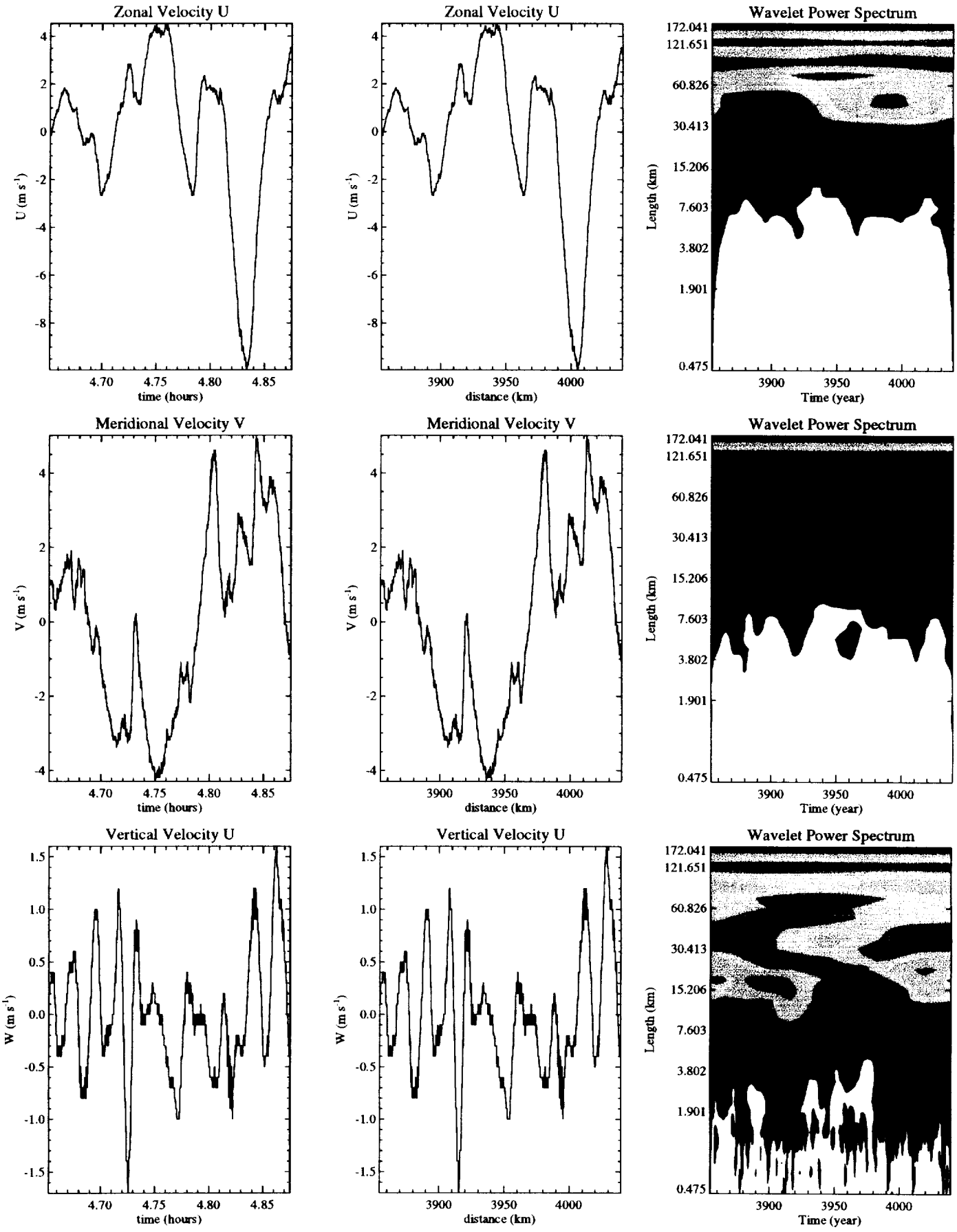
Zonal Velocity U
U (m s-1)
time (hours)
Zonal Velocity U
U (m s-1)
distance (km)
Wavelet Power Spectrum
Length (km)
Time (year)
Meridional Velocity V
V (m s-1)
time (hours)
Meridional Velocity V
V (m s-1)
distance (km)
Wavelet Power Spectrum
Length (km)
Time (year)
Vertical Velocity U
W (m s-1)
time (hours)
Vertical Velocity U
W (m s-1)
distance (km)
Wavelet Power Spectrum
Length (km)
Time (year)

Figure 11

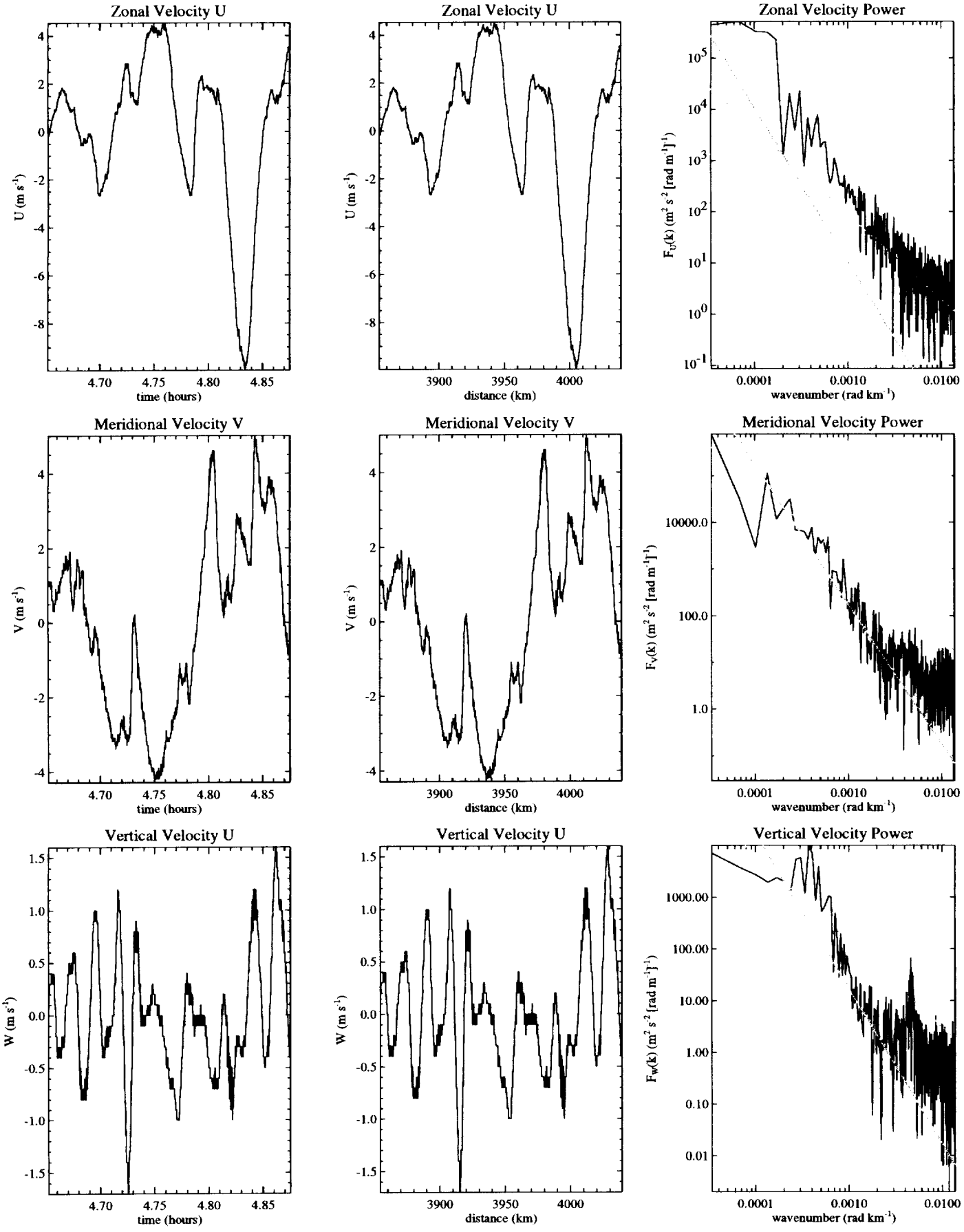
Zonal Velocity U
U (m s-1)
time (hours)
Zonal Velocity U
U (m s-1)
distance (km)
Zonal Velocity Power
F_U(k) (m2 s-2 [rad m-1]-1)
wavenumber (rad km-1)
Meridional Velocity V
V (m s-1)
time (hours)
Meridional Velocity V
V (m s-1)
distance (km)
Meridional Velocity Power
F_V(k) (m2 s-2 [rad m-1]-1)
wavenumber (rad km-1)
Vertical Velocity U
W (m s-1)
time (hours)
Vertical Velocity U
W (m s-1)
distance (km)
Vertical Velocity Power
F_W(k) (m2 s-2 [rad m-1]-1)
wavenumber (rad km-1)

Figure 12

REPORT DOCUMENTATION PAGE

Form Approved
OMB No. 0704-0188

1. AGENCY USE ONLY *(Leave blank)*	2. REPORT DATE	3. REPORT TYPE AND DATES COVERED
	September 1998	Contractor Report

4. TITLE AND SUBTITLE
Mesoscale Variability in SUCCESS Data

5. FUNDING NUMBERS
NAS5-97247
NRA-96-OA-01

6. AUTHOR(S)
PI: Stephen D. Eckermann

7. PERFORMING ORGANIZATION NAME(S) AND ADDRESS (ES)
Computational Physics, Inc.
2750 Prosperity Avenue, Suite 600
Fairfax, VA 22031

8. PEFORMING ORGANIZATION REPORT NUMBER

9. SPONSORING / MONITORING AGENCY NAME(S) AND ADDRESS (ES)
National Aeronautics and Space Administration
Washington, DC 20546-0001

10. SPONSORING / MONITORING AGENCY REPORT NUMBER
NASA/CR-1999-209461

11. SUPPLEMENTARY NOTES

12a. DISTRIBUTION / AVAILABILITY STATEMENT
Unclassified–Unlimited
Subject Category:43
Report available from the NASA Center for AeroSpace Information,
7121 Standard Drive, Hanover, MD 21076-1320. (301) 621-0390.

12b. DISTRIBUTION CODE

13. ABSTRACT *(Maximum 200 words)*

Analysis of meteorological, chemical, and microphysical data from the airborne SUCCESS mission is reported. Careful analysis of the complex DC-8 flight pattern of May 2, 1996 reveals 19 linear or nearly linear flight segments within six main geographical areas, which we have analyzed. Significant mountain wave activity is revealed in the data from the MMS and MTP instruments on the DC-8, which resembles previous observations of mountain wave structures near Boulder, CO. Strong mountain-wave-induced upwelling downwind of the Rockies is noted. Turbulence is also noted in regions of the mountain wave consistent with overturning near the tropopause. Zonal winds recorded on the ER-2 are shown to consistent with mountain wave breaking at or near critical levels in the stratosphere, consistent with the strong turbulence reported by the pilot during the ER-2 flight. Those observations have been supported with spectral analyses and modeling studies. "Postcasts" of mountain wave activity on May 2, 1996, using the Naval Research Laboratory Mountain Wave Forecast Model (NRL/MWFM) predicts both strong mountain wave activity near the tropopause (as measured by the DC-8) and stron mountain-wave-induced turbulence in the stratosphere (as encountered by the ER-2). Two-dimensional simulations of fluid flow over topography reveal similar isentropic structures to observations.

14. SUBJECT TERMS
Mesoscale, SUCCESS Data Analysis, mountain wave, ER-2, DC-8

15. NUMBER OF PAGES
26

16. PRICE CODE

17. SECURITY CLASSIFICATION OF REPORT	18. SECURITY CLASSIFICATION OF THIS PAGE	19. SECURITY CLASSIFICATION OF ABSTRACT	20. LIMITATION OF ABSTRACT
Unclassified	Unclassified	Unclassified	UL